Diapycnal diffusivity and transport of matter in the open ocean estimated from underway acoustic profiling and microstructure profiling.

Dissertation
zur Erlangung des Doktorgrades
der Mathematisch-Naturwissenschaftlichen Fakultät
der Christian-Albrechts-Universität
zu Kiel

vorgelegt von

Tim Fischer

Kiel 2011

Leibniz-Institut für Meereswissenschaften
an der Universität Kiel

Referent:	Prof. Dr. Peter Brandt
Korreferent:	Prof. Dr. Andreas Oschlies
Tag der mündlichen Prüfung:	04.05.2011
Zum Druck genehmigt:	25.05.2011
Gez.:	Prof. Dr. Lutz Kipp, Dekan

Abstract

Accompanying to a large scale tracer release experiment (GUTRE) at the oxygen minimum zone (OMZ) off West Africa, microstructure measurements have been performed during two cruises to independently estimate diapycnal diffusion and fluxes of matter across the OMZ's upper limit. The vessel mounted Acoustic Doppler Current Profilers have been used in this context to get underway estimates of finescale shear and allow to infer diapycnal diffusivity K indirectly. In this way the regional integral K for the depth range of OMZ upper half and tracer location (150m to 400m) has been determined to $K = 1.2 \cdot 10^{-5} \pm 0.2 \cdot 10^{-5} \frac{m^2}{s}$. This is a slightly higher value than expected for these latitudes and probably is caused by bottom topographic influence. The influx of oxygen brought by zonal jets and then diapycnally transferred to the OMZ has been estimated as $|\nabla \Phi_{O_2}| = 1.7 \pm 0.2 \frac{mmol}{m^3\, a}$ and thus is deemed to resupply a substantial part of the oxygen consumption in the upper half of the OMZ.

Begleitend zu einem großskaligen Tracer-Ausbreitungsversuch an der Sauerstoffminimumzone (OMZ) vor Westafrika wurden während zweier Forschungsfahrten Mikrostrukturmessungen durchgeführt, um unabhängige Schätzungen von diapyknischer Diffusion und diapyknischen Stoffflüssen über den oberen Rand der OMZ zu erhalten. Die schiffseigenen akustischen Strömungsmessgeräte (vmADCP) wurden in diesem Zusammenhang benutzt, um vom fahrenden Schiff aus die Strömungsscherung und indirekt auch den diapyknischen Austauschkoeffizienten K zu messen. Mit dieser Methode wurde der integrale Austauschkoeffizient für die gesamte Region - in dem Tiefenbereich von 150m bis 400m, wo die obere Hälfte der OMZ und der Tracer sich finden - zu $K = 1.2 \cdot 10^{-5} \pm 0.2 \cdot 10^{-5} \frac{m^2}{s}$ bestimmt. Das ist etwas mehr, als für diese Breiten zu erwarten wäre, und ist vermutlich auf den Einfluss der Bodentopographie zurückzuführen. Der von zonalen Strömungen herangeführte und dann von oben diapyknisch eintransportierte Sauerstoff wurde als volumenbezogener Zufluss von $|\nabla \Phi_{O_2}| = 1.7 \pm 0.2 \frac{mmol}{m^3\, a}$ gemessen und entspricht damit einem spürbaren Anteil der Sauerstoffzehrung in der oberen Hälfte der OMZ.

Printed on recycled paper

Contents

1 Introduction

The budget of energy for the global ocean circulation, its distribution and its pathways from surface and tidal forcing to friction, while keeping the ocean stratified, still is a matter of uncertainty [Wunsch and Ferrari, 2004].

The question of how exactly meridional overturning circulation is driven and stratification is maintained - with the early notion of uniform small-scale mixing balancing a slow uniform upwelling in the ocean interior [Munk, 1966] - was one driving force for a diverse, growing and constantly innovative "industry" of mixing research ([Lueck et al., 2002; Thorpe, 2005; Moum and Rippeth, 2009] for some general impression). Starting with consistent, but astonishingly low estimates of open ocean diapycnal mixing from different methods [Gregg, 1989; Ledwell et al., 1998], mixing research took its part in forming a more diverse picture with adiabatic processes and mixing hotspots contributing to the meridional overturning, so that low mixing in the ocean interior no longer is deemed disturbing [Webb and Suginohara, 2001]. Some additional contribution to watermass transformation from processes that originate from density being nonlinearly dependent on temperature and salinity, still further widens the gap that diapycnal mixing alone cannot account for [Klocker and McDougall, 2010], thus further reducing the probable share of diapycnal mixing.

The regional distribution of diapycnal mixing is diverse, probably caused to a large extent by currents interacting with topographic features [Nikurashin and Legg, 2011]. This just partly known global pattern of diapycnal mixing is deemed important for understanding global circulation, as circulation patterns in Global Circulation Models are sensitive to changing mixing patterns [Saenko and Merryfield, 2005; Jayne, 2009]. Despite remarkable developments in surveying the global mixing patterns [Kunze et al., 2006] and some generalizing insight, expressed as proposed parametrizations ([Gregg et al., 2003] with preceding history, [StLaurent et al., 2002]), complexity and cost of measurement methods prevent faster progress.

Our current interest in diapycnal mixing is mainly focused on its distribution and on its practical potential to infer diapycnal fluxes of energy and matter, given that adequate profiles and local gradients are known. Here we present an underway method of acoustically estimating diapycnal diffusion from moving vessels for the main thermocline down to a depth of 500 m. The greater spatial coverage in diapycnal mixing data compared to classic station based measurements, and its use to estimate regional thermocline fluxes of oxygen and greenhouse gas nitrous oxide is demonstrated for the well sampled region of the GUinea dome Tracer Release Experiment (GUTRE) off West Africa. The acoustic data from vessel mounted Acoustic

Doppler Current Profilers (ADCP) that are used here, do allow estimates of that part of diapycnal mixing that may be ascribed to breaking internal waves. This certainly is an important contributor to mixing - and for Guinea Dome Region, internal wave shear indeed seems to be the predominant mixing driver -, but for other regions its predominance has to be justified for each case. Another prominent mixing process that common turbulence-assuming measurement methods are downright blind to, is double diffusion. Its contribution may be partial, like at the North Atlantic Tracer Release site [StLaurent and Schmitt, 1999], or even predominant like in the Western Tropical Atlantic staircase [Schmitt et al., 2005].

The conceptual treatment of mixing usually is via an exchange coefficient K, that in analogy to molecular diffusion treats the mixing process as a downgradient diffusive process. Stirring caused by velocity differences and overturning leads to stretching and folding of water parcels, thus allowing molecular diffusion to act much more efficient. This causes the epiphenomenon of an accelerated (pseudo-) diffusion. This approach being quite successful in practice, it is followed here as well, implicitly present for example in the used Osborn parametrization for K from microscale shear (section 3.2) and in the formulation of fluxes as K times parameter gradient in analogy to molecular diffusive fluxes (section 5.1).

2 Guinea Dome Region

In Nov. 2008 and Dec. 2009 mixing related data were sampled in the Tropical North Eastern Atlantic Ocean in the frame of the large scale Tracer Release Experiment GUTRE. Tracer was released about $8^\circ N$ $23^\circ W$ in 300 m in April 2008 and was then expected and found in the region referred to as Guinea Dome Region (GDR), which is limited roughly to the North by Cape Verde archipelago, to the West by the Mid Atlantic Ridge extensions, to the South by the North Equatorial Countercurrent (NECC) and to the East by the African continent (figure 2.1). A prominent feature of bathymetry is the elongated seamountain range from $10^\circ N$ $20^\circ W$ to $6^\circ N$ $24^\circ W$ with single peaks shallower than 1000 m.

The North Equatorial Current (NEC) as part of the subtropical gyre and Cape Verdian Frontal Zone (CVFZ) being further North and not influencing, GDR lies in the weakly ventilated shadow zone [Stramma et al., 2005]. The flow field in GDR is dominated by eddies [Stramma et al., 2005; Brandt et al., 2010], but the mean flow exhibits distinct zonal alternating current bands (figure 2.2 and 2.3 upper panel). The cyclonic Guinea Dome also is a mean feature, best detected from its isopycnal doming, and of reportedly permanent presence but seasonal variation [Siedler et al., 1992]. It is assumed to be a patch of seasonally varying upwelling, the wind field supporting favourable conditions for Ekman suction from July to October [Siedler et al., 1992] or June to September [Doi et al., 2010]. There are no observational values, but Ekman velocities given by [Schott et al., 2004] allow estimates of upwelling transports of up to 2 Sv annual average.

The weak ventilation causes an oxygen minimum zone (OMZ) at 300 to 600 m depth with its core at about 400 m and $\sigma = 27.1\,kg/m^3$, that ranges from about $5^\circ N$ to $20^\circ N$ and from $30^\circ W$ to the African continent. Oxygen supply replenishing respiration loss is via the easterly zonal jets (figure 2.3 lower panel), and isopycnal and diapycnal eddy fluxes [Brandt et al., 2010]. There has been detected a longterm decreasing trend in oxygen concentration (minus 15 to 20 $\mu mol/kg$ in 50 years [Stramma et al., 2008], minus 15 $\mu mol/kg$ in 25 years [Brandt et al., 2010]), that seems to be driven mainly by changes in ventilation [Karstensen et al., 2008; Brandt et al., 2010]. Total consumption in OMZ that has to be resupplied by advection, mesoscale eddies and diapycnal diffusion is estimated to 5 to 6 $mmol/m^3/a$ [Karstensen et al., 2008] and 2 to 3 $mmol/m^3/a$ [Brandt et al., 2010]. The GUTRE tracer was released at $\sigma = 26.85\,kg/m^3$ at about 300 m depth in the upper oxygen gradient of the OMZ, in order to estimate diapycnal oxygen transport from above.

Our accompanying mixing measurements, that shall deliver another estimate of

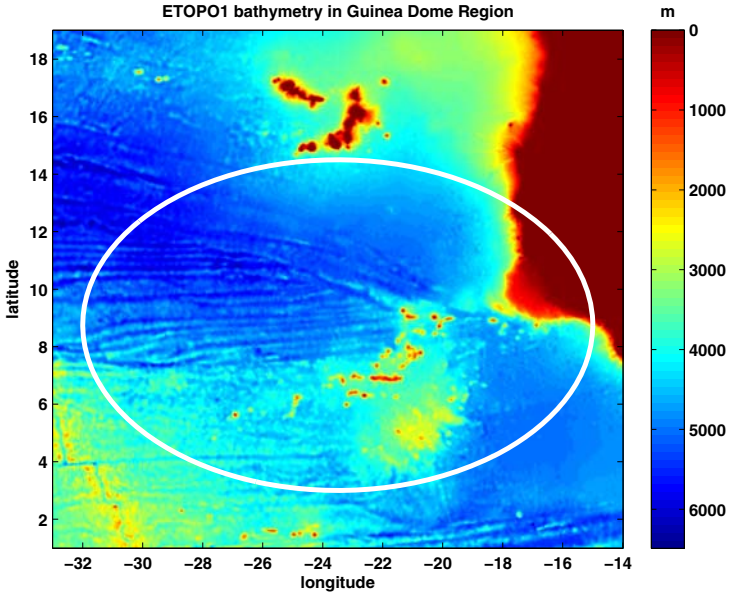

Fig. 2.1: Bathymetry of the Tropical Northeastern Atlantic following ETOPO1 [Amante and Eakins, 2009]. White ellipse: rough limits of Guinea Dome Region (GDR), where tracer release experiment GUTRE took place. About compliant with the area [Schott et al., 2004] ascribed to Guinea Dome.

diapycnal diffusion and oxygen transport, rely on smallscale shear being the dominant source of diapycnal mixing. The main other mixing process that might play a role in GDR is double diffusion. To test for the latter, the density ratio R_ρ is calculated for all available CTD profiles of the two cruises (figure 2.4). [StLaurent and Schmitt, 1999] in their study of double diffusive contribution to mixing in the NATRE tracer release region at Canary Current limit possible influence of double diffusion to $1 < R_\rho < 2$, with clear substantial contribution showing up in their diffusion estimates from about $R_\rho < 1.7$. This different quality is accounted for by the chosen colorscale of figure 2.4. The dominant feature of the latitudinally sorted CTD profiles there is the streak of low R_ρ where relative fresh and cold Antarctic Intermediate Water (AAIW, its core at the salinity minimum about 800 m deep) underlies relative salty and warm South Atlantic Central Water (SACW, its lower boundary coinciding with the oxygen minimum core [Stramma et al., 2005]). Abundance and values of R_ρ here are comparable to the profiles [StLaurent and Schmitt, 1999] find for NATRE at 100 m to 500 m depth,and like at NATRE site, we do only occasionally find double diffusive staircase structures. So in analogy to [StLaurent and Schmitt, 1999]'s results we may conclude that below the oxygen minimum core, mixing from double diffusion is significant and must be accounted for, even if turbulent processes disrupt the formation of steplike structures.

However, our main interest lies in the depth range above the oxygen minimum core due to the range of our instruments and due to the tracer lying there at $\sigma = 26.85\,kg/m^3$ that is to deliver the integral estimate of diapycnal diffusion that we will have to compare to. In that depth range above 400 m density ratios below 2 are

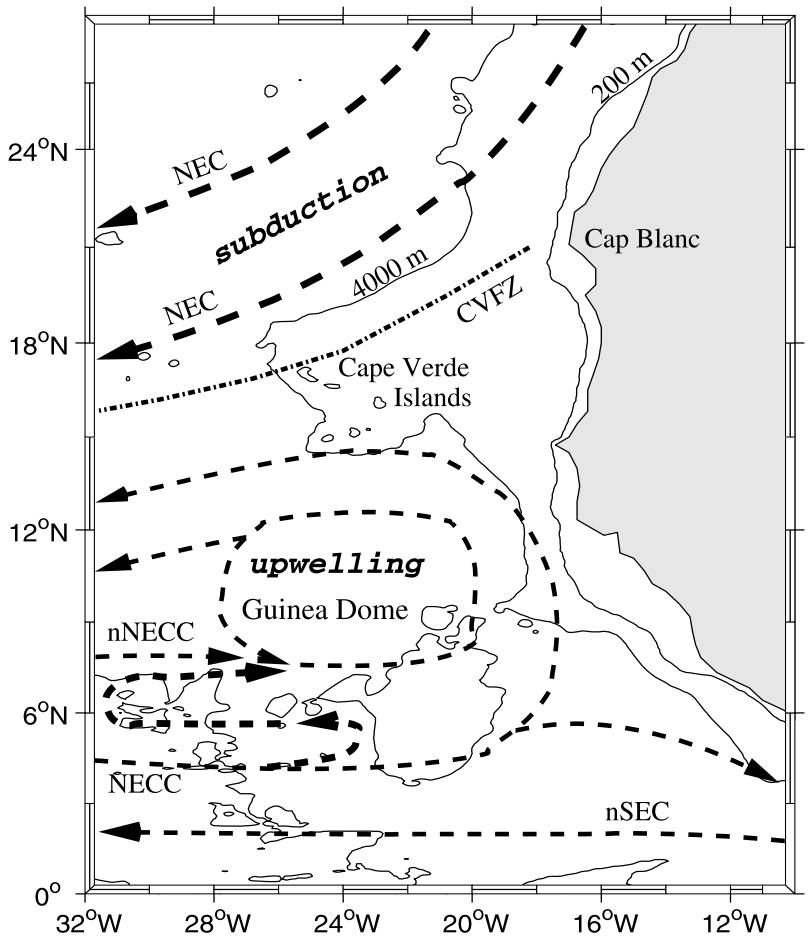

Fig. 2.2: Schematic of mean upper ocean currents in Guinea Dome Region, from [Stramma et al., 2005]. NEC: North Equatorial Current, CVFZ: Cape Verde Frontal Zone, NECC: North Equatorial Countercurrent, nNECC: northern branch of NECC, nSEC: northern branch of South Equatorial Current.

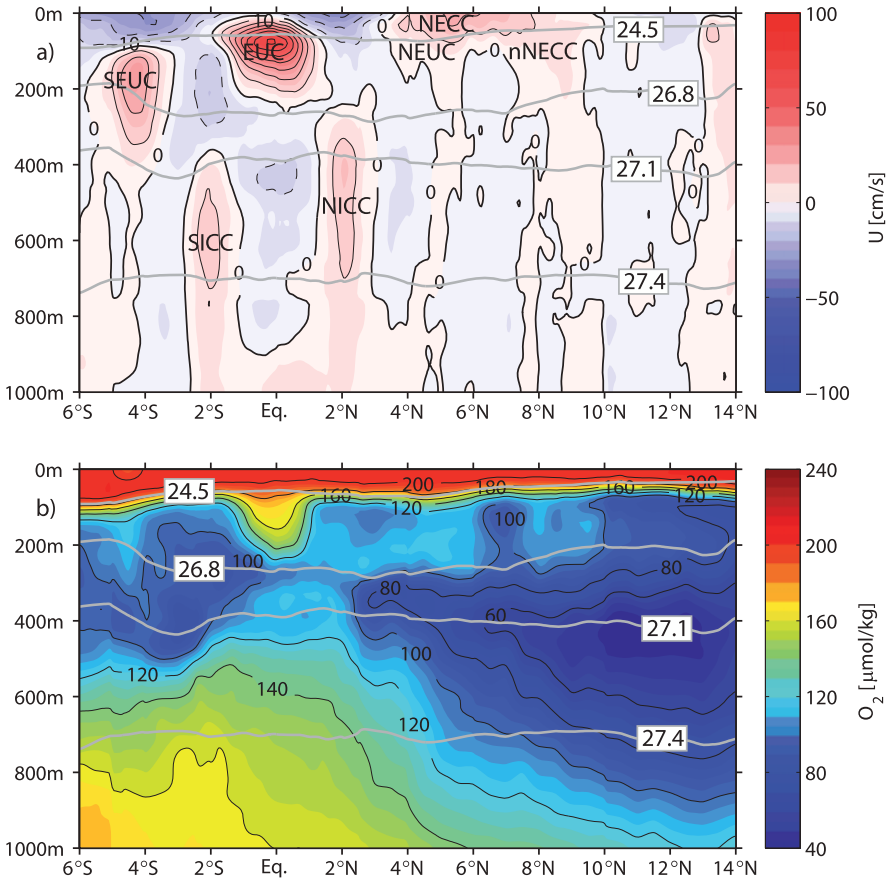

Fig. 2.3: Meridional section at and near 23° W, from [Brandt et al., 2010]. Upper panel showing mean zonal currents, in Guinea Dome Region the characteristic alternating current bands. NECC: North Equatorial Countercurrent, nNECC: northern brach of NECC, NEUC: North Equatorial Undercurrent, EUC: Equatorial Undercurrent, SEUC: South Equatorial Undercurrent, NICC and SICC: North and South Intermediate Countercurrents. Lower panel showing mean oxygen concentration. Oxygen minimum core is at $\sigma = 27.1\,kg/m^3$. Easterly zonal jets exhibit elevated oxygen content.

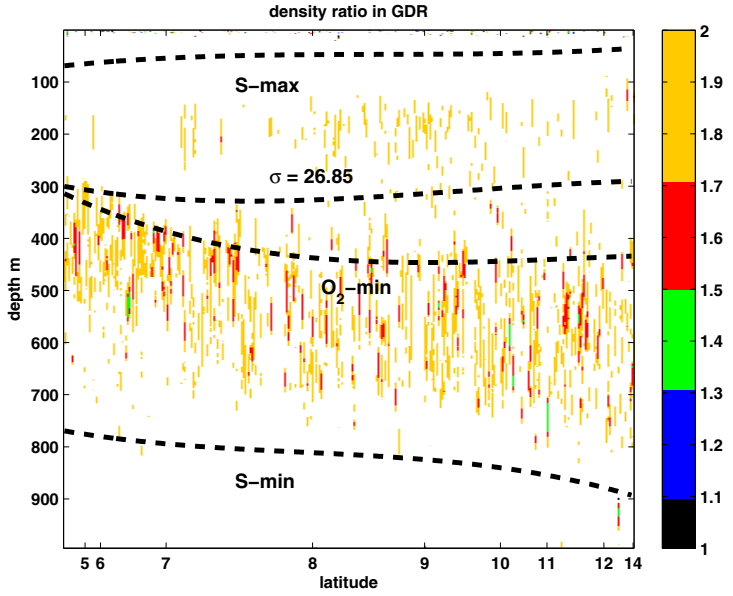

Fig. 2.4: Density ratio R_ρ to evaluate susceptibility to double diffusion. CTD profiles of two cruises in GDR sorted by latitude. The distinct streak of $R_\rho < 2$ lies between South Atlantic Central Water SACW (its lower limit at $O_2 - min$) and Antarctic Intermediate Water AAIW (core at $S - min$). S-max characterizes Subtropical Underwater STUW. $\sigma = 26.85$ is the target density the GUTRE tracer was released on.

sparse and values below 1.7 extremely rare. The Subtropical Underwater (STUW, characterized by the salinity maximum in the sharp thermocline [Stramma et al., 2005]) overlying the SACW only occasionally can account for a very modest amount of diffusive instability. Thus for our main interest of inferring diapycnal diffusivity and downward diapycnal oxygen transport at above the oxygen minimum core, we presumably may rely on our methods based on smallscale shear measurements. For the deeper parts, a double diffusive contribution (salt finger enhancement [StLaurent and Schmitt, 1999]) should be added.

Stratification in a band of 150 m above and below the tracer depth proves to be quite constant anywhere in GDR, even if the individual profiles vary regionally in their constant N^2 (figure 2.5) by a factor of 2. An average density profile for GDR is constructed (figure 2.6) which keeps the characteristic shape and allows to translate density coordinates to a scaled depth. From above 72 m scaled depth, the relation is no longer by density, but by a linear relation to in-situ depth determined by the mixed layer depth that is fixed to a scaled depth of 24 m. The reason is the distinct regional variability of mixed layer density.

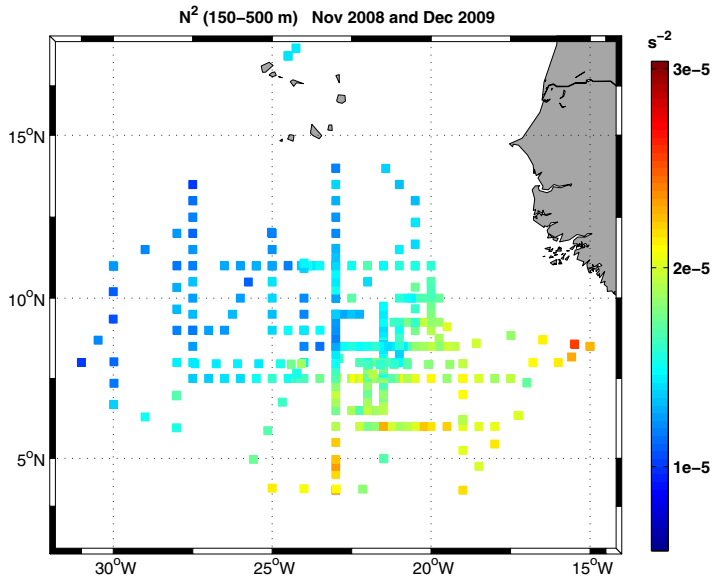

Fig. 2.5: Regional distribution of buoyancy frequency squared, in the depth range 150-500 m of approximate N^2 constancy.

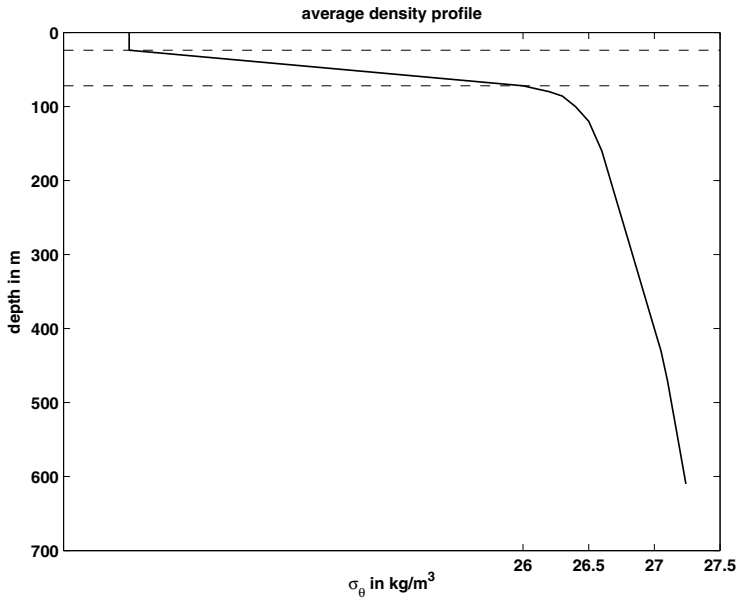

Fig. 2.6: Average density profile for GDR. Dashed lines mark mixed layer depth at 24 m scaled depth, and the lower end of the sharp thermocline at 72 m scaled depth and $\sigma = 26$.

3 From the microstructure probe to diffusivities

3.1 Introduction

The Sea&Sun Technology's microstructure probe [SeaSunTechnology, 2011] we use is only one of many different types that are employed worldwide, though with some spread around Europe. For a technical review of velocity microstructure history and profiler types see [Lueck et al., 2002]. We mainly use S&ST type MSS90D tethered but quasi free-falling profiler (figure 3.1) with airfoil velocity shear sensors. These need oncoming flow of approximately 0.5 m/s in order to sense fluctuations of horizontal velocity as a change in angle of attack on the airfoil. Subsequently a piezo crystal measures the resulting lift force very sensitively. Data are transmitted realtime via tether cable to the deck unit at 1024 Hz.

3.2 Along the measurement chain

3.2.1 Basic relations and processing

The measurement chain from airfoil sensor tip to the transmitted digital signal begins with the flow against the sensor tip being produced by the probe's sink velocity, under an angle of attack that is modulated by horizontal velocity fluctuations. The lift force at the tip sensed by the piezo crystal is

$$F = \frac{1}{2}\,\rho\,U^2\,sin\,2\alpha \cdot A \tag{3.1}$$

with ρ water density, U total water velocity at angle of attack α, and A section area of tip [Macoun and Lueck, 2004]. Due to its finite length the sensor tip acts as a spatial low pass filter. The piezo crystal translates lift force into voltage linearly in a limited range of α:

$$E = 2\sqrt{2}\,\frac{S}{A}\,F = \sqrt{2}\,S\,\rho\,U^2\,sin\,2\alpha = 2\sqrt{2}\,S\,\rho\,v_{sink}\,u' \tag{3.2}$$

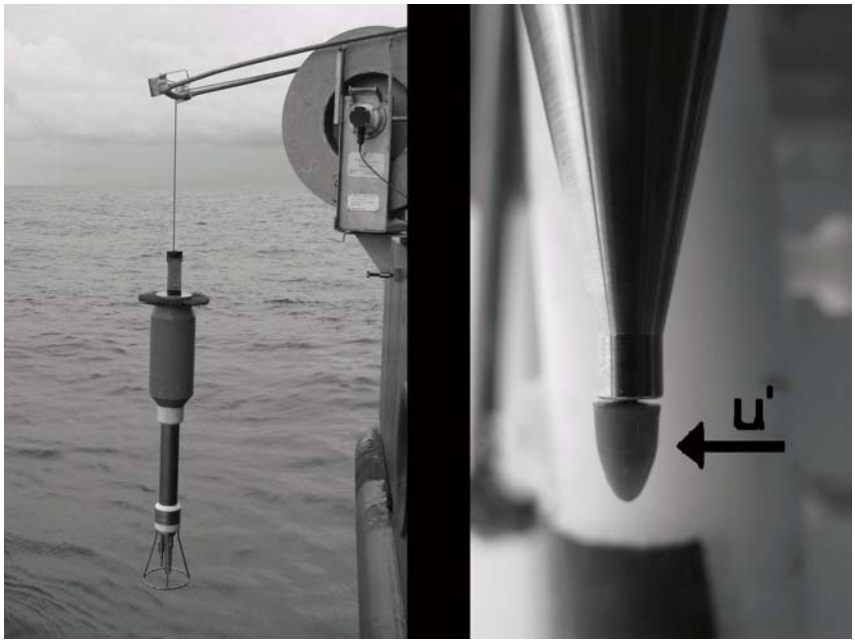

Fig. 3.1: Sea & Sun technology's microstructure profiler MSS90D on its way to the water. Right panel closeup of 4mm-airfoil shear sensor tip.

with S manufacturer's reported sensitivity. After some amplification there is a electronic 1-Hz highpass filter to eliminate spurious signals resulting from slow probe undulations, and finally the AD converter. The piezo crystal is sensitive to temperature change, which has to taken into account for processing [ISW Wassermesstechnik Dr. Hartmut Prandke, 2009]:

$$S_T = S_{cal} \cdot (1 - 0.011\,[21^\circ\,C - T])\,. \tag{3.3}$$

Processing of recorded data means in a first step calculating backward to u' and differencing to $\frac{\partial u'}{\partial z}$, then in a second step doing shear spectra of 2 seconds overlapping data chunks (figure 3.2). An important base for getting a dissipation estimate from shear spectrum is Nasmyth's universal shear spectrum from field measurements (values reported by [Oakey, 1982]), a simple fit found by R. Lueck was reported by [Wolk et al., 2002]. To derive a dissipation estimate from shear spectra, spectral density is integrated in a usable wavenumber band, the latter determined from fitting Nasmyth's universal spectrum. After correcting spectral variance for losses to the lower and higher wavenumbers, ϵ is calculated by the relation

$$\epsilon = 7.5\,\nu \left\langle \left(\frac{\partial u}{\partial z} \right)^2 \right\rangle . \tag{3.4}$$

Typical uncertainties of resulting ϵ estimates are 50% (95% confidence limit).

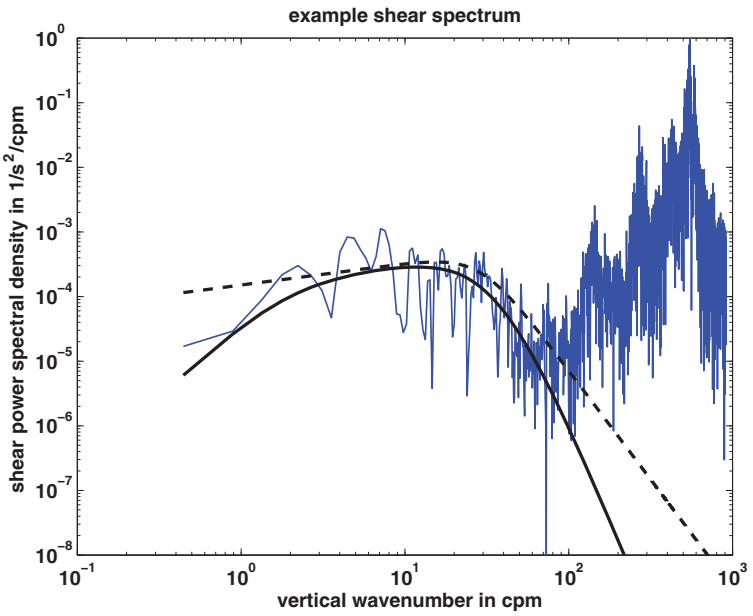

Fig. 3.2: Typical shear spectrum over vertical wavenumber (blue line). Wavenumbers larger 100 cpm show vibrational noise from probe body and sensors. Dashed black line: Fitted Nasmyth universal shear spectrum. Solid black line: Damped Nasmyth spectrum from spatial smoothing at sensor tip (higher wavenumbers) and electronic highpass filter (lower wavenumbers).

3.2.2 Collision spikes

Typical ϵ profiles have about 5 bad bins due to collisions in the water column (figure 3.3), many of them in the chlorophyll maximum. But the resulting spikes are hard to evaluate if they are true spikes or just events of high mixing. Therefore a spike detecting algorithm was developed to reduce human interference to the absolute minimum.

Spikes leave characteristic traces in the recorded signal (figure 3.4), as well as in form of distorted shear spectra (figure 3.5). Characteristic features have been from signal time series and spectra have been combined to key figures, and for these a qualityfunction was empirically developed. 50 hand evaluated profiles served partly to develop, partly to test the final algorithm (figure 3.6).

3.2.3 Detection limit of dissipation estimates and its treatment

From ϵ-profiles and their histogrammes may be deduced a noise level of approximately $\epsilon_{NL} = 7 \cdot 10^{-10}\, m^2/s^3$. Thus a limit for detecting a signal with confidence is the detection limit $\epsilon_{DL} = 2 \cdot 10^{-9}\, m^2/s^3$. When trying to estimate average ϵ for some depth range there arises a problem how to treat values of $\epsilon < \epsilon_{DL}$. Setting them to zero will underestimate average ϵ, not changing them will overestimate average ϵ.

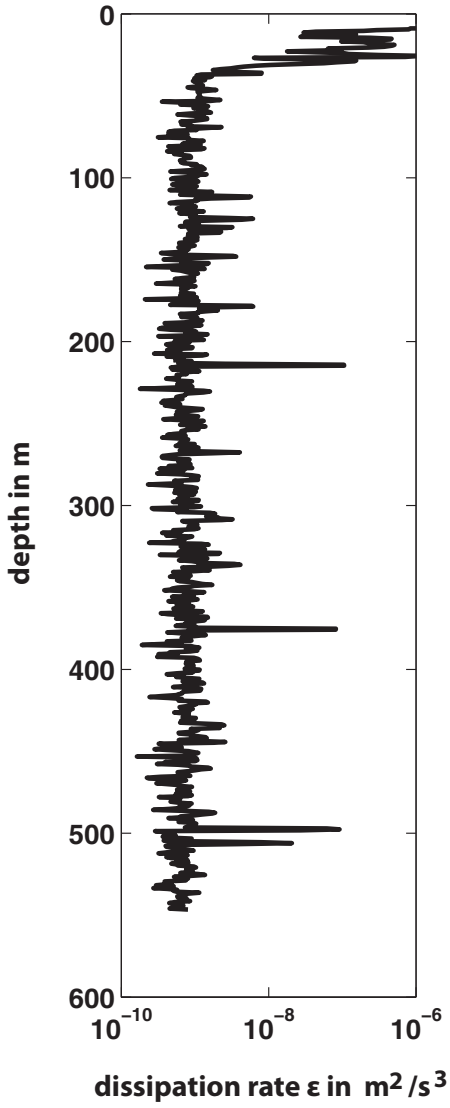

Fig. 3.3: Example profile of dissipation rate ϵ with peaks that may or may not be collision spikes.

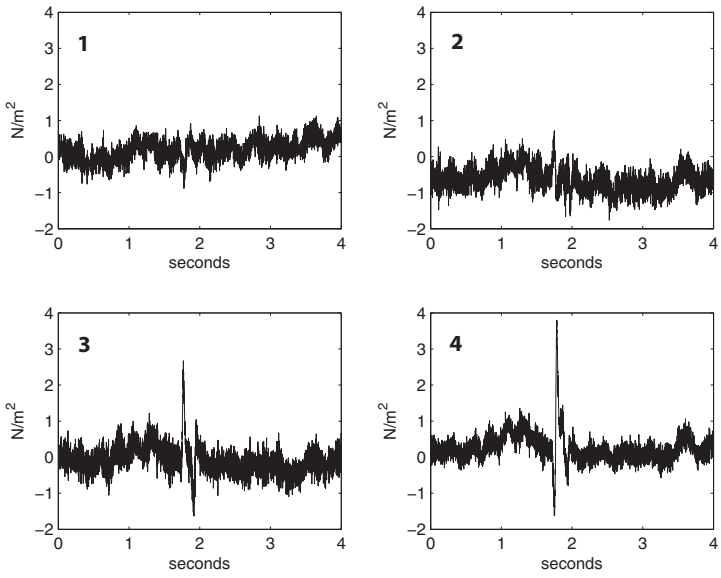

Fig. 3.4: Lifting force density at sensor tip, recorded by 4 parallel sensors mounted on one probe. No. 3 and 4 show a clear collision pattern starting at 1.7 seconds, No. 2 still a weak one.

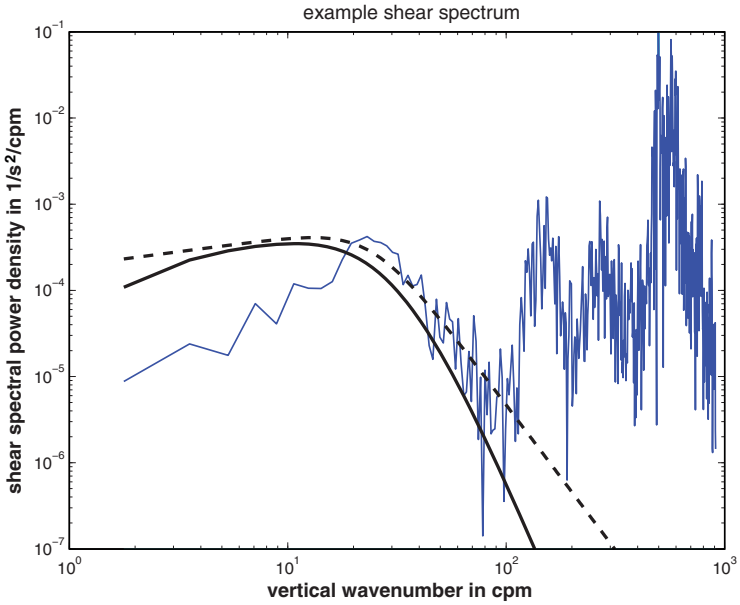

Fig. 3.5: Shear spectrum (blue line) of a signal sequence that contains a collision spike. The spectral shape in the range up to 40 cpm is clearly different from Nasmyth spectrum. Dashed black line: Fitted Nasmyth universal shear spectrum. Solid black line: Damped Nasmyth spectrum from spatial smoothing at sensor tip (higher wavenumbers) and electronic highpass filter (lower wavenumbers).

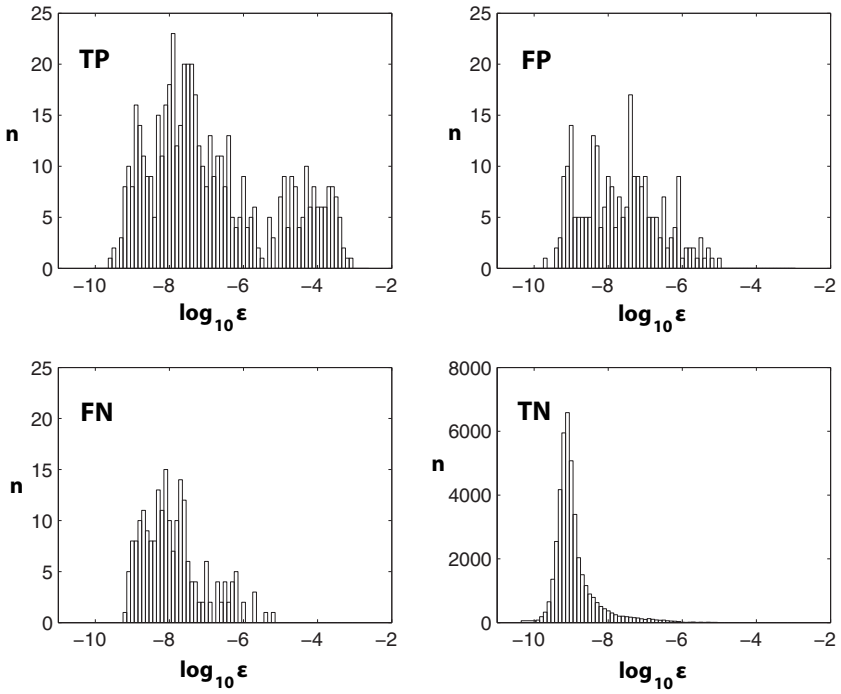

Fig. 3.6: Classification matrix for implemented spike detecting algorithm, developed empirically from 50 hand evaluated dissipation rate profiles. Histogrammes of dissipation rate ϵ in logarithmic classes; n: cumulative number of occurrences in 50 profiles; note different scales. TP: true positive detected spikes. FN: false negative = spikes falsely rated by algorithm as good. FP: false positive = good values falsely rated by algorithm as spikes. TN: true negative ratings. Resulting statistical key figures: sensitivity (TP as fraction of hand rated spikes) 0.72 (weighted by ϵ it is 0.99); fallout (FP as fraction of hand rated good values) 0.006. Average ϵ of hand despiked profiles: $1.8 \cdot 10^{-8}\, m^2/s^3$. Average ϵ of algorithm despiked profiles: $1.7 \cdot 10^{-8}\, m^2/s^3$. Not applying any spike detection results in a 10 times higher value.

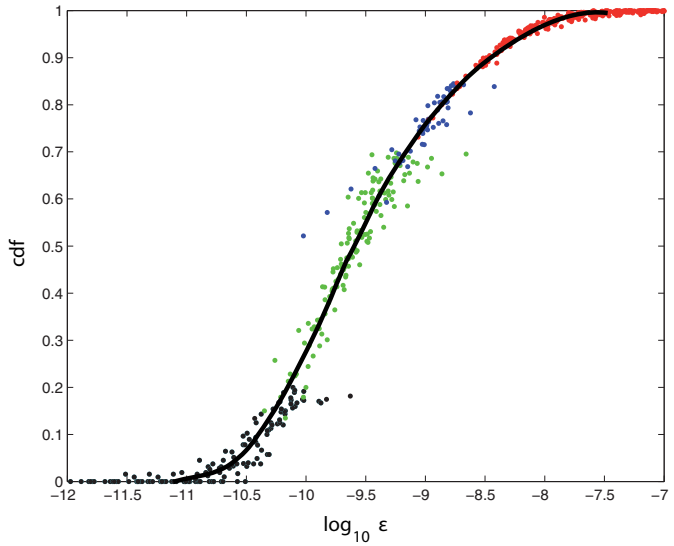

Fig. 3.7: Composite dissipation cumulative distribution for use as a 'universal' base distribution (black line) in order to estimate substitute values for ϵ lower than detection limit $\epsilon_{DL} = 2 \cdot 10^{-9}\, m^2/s^3$. Made from a mosaic of parts of ϵ histogrammes with $\epsilon > \epsilon_{DL}$. Red dots: ϵ from depths below 150m. Blue dots: ϵ above 150m and below sharp thermocline. Green dots: ϵ in sharp thermocline. Black dots: ϵ in lower mixed layer. Logarithmic ϵ axis has arbitrary offset and needs to be shifted according to encountered fraction of measured $\epsilon < \epsilon_{DL}$.

From observation that ϵ-distribution on short timescales of $O(1\,h)$ and from depth bins of uniform stratification show similar shape for $\epsilon > \epsilon_{DL}$, just shifted in ϵ according to overall mixing intensity: construct a 'universal' ϵ distribution from distribution parts with $\epsilon > \epsilon_{DL}$ by shifting and mosaicking (figure 3.7).

This then allows estimating one uniform substitute value for all $\epsilon < \epsilon_{DL}$ determined as a function of the percentage of measured values below detection limit. The validity of the universal distribution for sharp thermocline and lower mixed layer is questionable, but below cdf = 0.6 the exact shape of the distribution does only insignificantly influence the final resulting ϵ. A good substitute value is needed particularly for measured ensembles with a higher fraction of ϵ below detection limit than about 0.8.

3.3 Diffusivities from MSS: a chain of assumptions

First assumption that is needed for practical work is that oncoming flow while falling does not distort velocity fluctuation we want to measure. Only indication up to today that this assumption is good, is a theoretical consideration of an early microstructure pioneer [Hayes et al., 1984] who estimated a 5% overestimate for velocity (i.e. 10% for ϵ) from potential flow theory.

Second assumption is local isotropy, that is virtually always assumed, more for practical reasons, as we only have one component of the strain rate tensor. Local isotropy manifests in the factor 7.5 of

$$\epsilon = 7.5\,\nu \left\langle \left(\frac{\partial u}{\partial z} \right)^2 \right\rangle, \tag{3.5}$$

a consequence of isotropy, that [Pope, 2000] leaves to his readers to solve as an exercise with some hints. But in reality anisotropy even in the microstructure range is observed [Gargett et al., 1984], and for our configuration of measured vertical shear of horizontal velocities can lead to overestimates up to factor of 3 (a review section is found in [Thorpe, 2005], especially in strong stratification. Up to now there is no commonly accepted correction method.

The third assumption is Osborn's parametrization to get diapycnal diffusivity K:

$$K = \Gamma \frac{\epsilon}{N^2} \tag{3.6}$$

with ϵ and N^2 meant as ensemble representatives, with need to (usually) spatially average over some depth range of order 10m. The parametrized K is understood as including the mixing effect of smaller scales as well and is thus describing the overall mixing effect in that depth range (a consequence of the balance of turbulent kinetic energy [Osborn, 1980] gives). Γ is called dissipation ratio [StLaurent and Schmitt, 1999] and is connected with mixing efficiency which is also called flux Richardson number R_f. There is ambiguity what scales to use for averages of ϵ and N^2 and there is a whole literature about mixing efficiency and its dependencies on constraints. Usually the classic value of $\Gamma = 0.2$ or near is chosen, because in practice it appears to be a good estimate for many not too extreme conditions. But there is no final certainty about Γ. Nevertheless we choose $\Gamma = 0.2$ in order to allow results to be compared to other work groups.

4 Diffusivities derived from underway acoustic measurements

4.1 Introduction

A 30-month large scale Tracer Release Experiment at and near Guinea Dome (acronymed GUTRE) was opportunity to win a large set of mixing-related observational data. Two tracer survey cruises, the first in November 2008 on FS Merian [Maria S. Merian, 2008], the second in December 2009 on FS Meteor [Meteor, 2009] covered an area of 1200×800 kilometers in the region of the oxygen minimum zone off western Africa (figure 4.1). The covered region shall subsequently be called Guinea Dome Region or GDR, as it comprises the area of that current feature. Data comprise continuous velocity data of the upper 500-600m from a 75kHz vessel-mounted Acoustic Doppler Current Profiler (vmADCP), a total of 115 microstructure shear profiles at 39 stations from a tethered microstructure probe (MSS), and a total of 334 hydrographic profiles from a Conductivity-Temperature-Depth recorder (CTD) mounted at the water sampler rosette. Focus is on the depth range of 150m-500m for several reasons: this range covers large parts of the oxygen minimum zone and the depth of the tracer release experiment (which will deliver an integral estimate for effective diapycnal diffusion in GDR); it is a range of rather uniform stratification (refer to figure 2.6 in chapter 2), thus there is reason to expect vertical homogeneity in density-gradient-related parameters like internal wave activity and mixing intensity; the mixed layer with few valuable information from both vmADCP and MSS is avoided; the thermocline at its sharpest part below the mixed layer is avoided, for its strong stratification renders mixing estimates from MSS more uncertain, and its small vertical extension and sharp flanks pose problems to acoustic observation of internal waves that given instrument resolution can't compensate; and finally available vmADCP and MSS instrumentation constrains range to depths shallower than 500 to 600 m.

There are two main objectives with this data. One is to check if vmADCP survey of the upper ocean internal wave field is feasible from a fast moving ship at changing speed. The other is to relate vmADCP borne estimates of finescale vertical shear on scales of O(10m) to O(100m) and MSS borne estimates of microscale vertical shear on scales of O(1cm) to O(1m). Such a relation would allow estimates of diapycnal mixing from cruising vessels and could extend the observable information on diapycnal mixing by one dimension (i.e. from profiles to a continuous section).

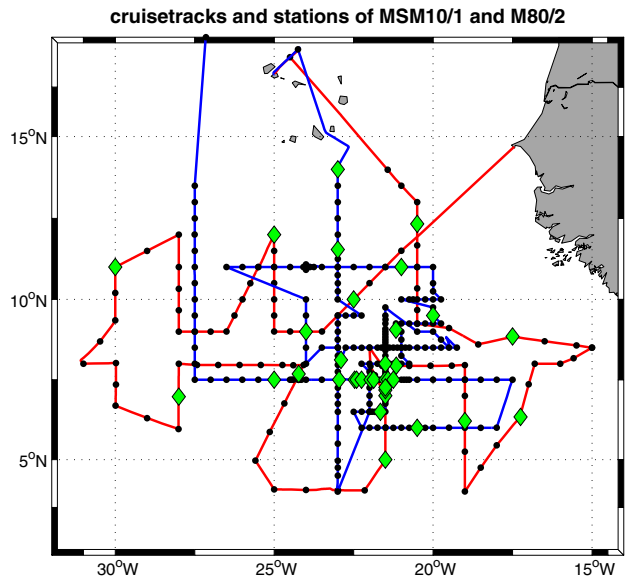

Fig. 4.1: Cruisetracks of Maria S. Merian MSM10/1 in Nov. 2008 (blue line) and Meteor M80/2 in Dec. 2009 (red line). Black dots: CTD stations. Green diamonds: combined MSS/CTD stations.

In mixing research there has been an early interest in the link between finescale processes and microscale processes, especially how internal waves contribute to turbulence and mixing [Nasmyth, 1973; Gargett, 1976]. Mechanisms are not completely understood until present, but observations of finescale shear and microscale shear suggest a strong link (see [Winkel et al., 2002] and an example from our measurements in figure 4.2). The simplified model picture of that link is one of internal waves that interact, become unstable and break, leading to turbulent overturns that finally cascade down to dissipative scales (illustrated by figure 4.3, adapted from [Smyth et al., 2001]). Several parametrizations have been proposed in the past to express microscale shear power (related to dissipation and diapycnal diffusivity) as a function of internal wave shear plus some more parameters (e.g. [Munk, 1981; Gargett, 1990] and [Polzin et al., 1995]'s modification of [Henyey et al., 1986]).

Breaking internal waves is only one important contributor to mixing. Another is double diffusion. Although in GDR prominent staircases are most rare, double diffusion might nonetheless play a role in mixing, as it might be concealed by dominant turbulent mixing that prevents staircases to be formed. That is what [StLaurent and Schmitt, 1999] find at a site north of GDR at Canary Current. Observed density ratio R_ρ at GDR does not support the hypothesis of an important contribution of double diffusion for the depth range above the oxygen minumum core at about 400 m (refer to chapter 2), so we judge double diffusion to play a minor role for mixing here.

There is no indication that further processes might be important that could not be observed as vertical shear of horizontal velocities. Both cruises happened to be past

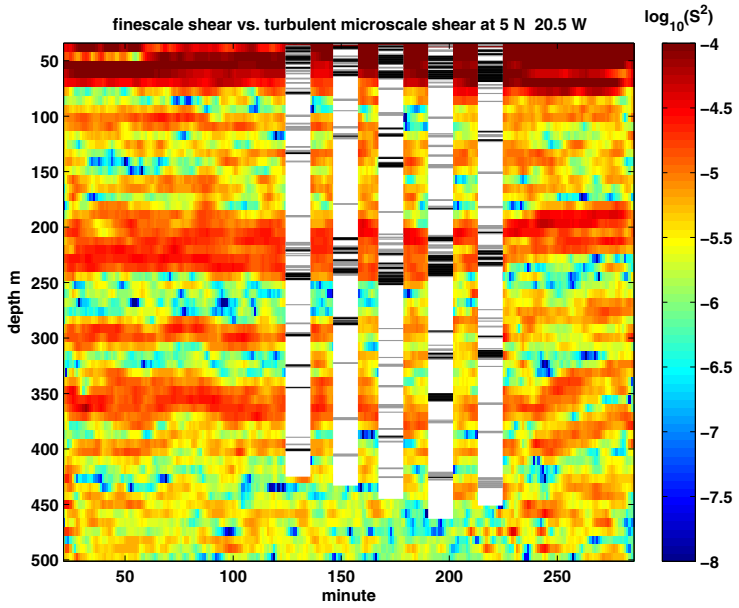

Fig. 4.2: Example of a combined dataset of microstructure profiles (white bars) and ADCP (coloured background). Marks on MSS profiles represent dissipation rates $\epsilon > 3 \cdot 10^{-9} \frac{m^2}{s^3}$ (grey) and $\epsilon > 1 \cdot 10^{-8} \frac{m^2}{s^3}$ (black). ADCP vertical shear variance S^2 in s^{-2} is estimated from velocity first difference.

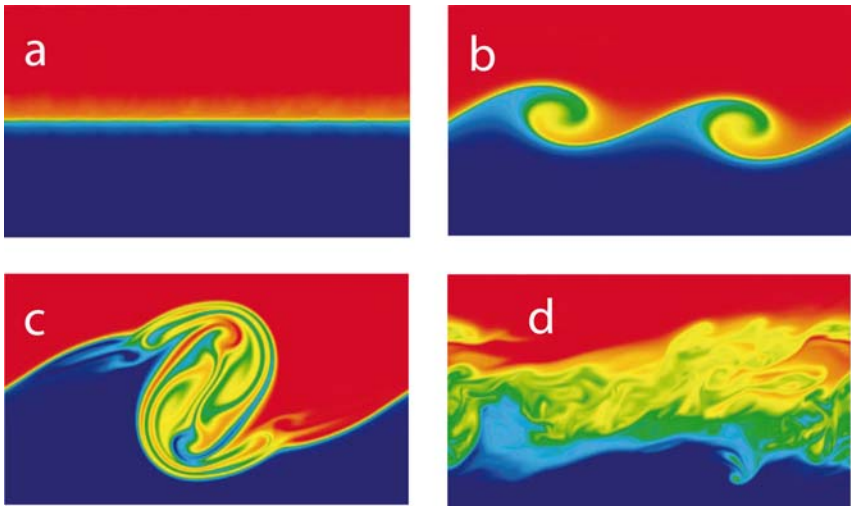

Fig. 4.3: From finescale shear to microscale shear and mixing: development of a Kelvin-Helmholtz instability between two sheared temperature layers; illustrations of direct numerical simulations of [Smyth et al., 2001]. a) is at time of maximum finescale shear while d) is at time of maximum microscale shear.

upwelling season (cf. chapter 2), so horizontal variability of vertical velocities from convection should be negligible. Thus GDR down to 400 m seems to be a "single-parameter" region adequate to study mixing caused by instability of finescale velocity structures.

Finescale shear is commonly characterized by shear variance or shear power. Shear variance has been frequently measured by acoustic means in the past, but traditionally as more or less point measurements: from fixed ADCP [Stacey, 2003; VanHaren, 2009], lowered ADCP on station [Leaman, 1976; Polzin et al., 2002; Garabato et al., 2004; Walter et al., 2005; Kunze et al., 2006, 006b], expendable current profilers XCP [Nagasawa et al., 2002; Polzin et al., 2002], or slowly moving vessels in small areas [Itsweire et al., 1989; Gargett, 1994].

Shear variances have to our knowledge not been measured from a cruising research vessel with its typical velocity pattern of frequent oscillations between zero and full speed, and with the resulting data quality problems solved. [Alford, 2008] reports shear variance during a transit, but averages horizontally rather heavily and does not report noise level or signal loss due to his processing, or how he deals with changing ship speed. From the plots a noise level of about $2 \cdot 10^{-5}\ s^{-2}$ can be read which would correspond to roughly 3 times the Garrett-Munk model shear variance. His focus is on very strong signals in the upper 150m though. [Rainville and Pinkel, 2004] report internal wave observations from shipboard ADCP but also do not comment on ship speed related bias.

Despite half a century of field measurements, total area coverage of mixing observations is small because of high financial and time effort inherent to the used methods. Mostly timeseries-point-measurements with different methods, spatial track series of profiles, plus a few even more elaborate and as valuable as expensive largescale Tracer Release Experiments in different regimes have been performed: in the upper ocean [Ledwell et al., 1998], over rough bathymetry [Ledwell et al., 2000], in double diffusive staircases [Schmitt et al., 2005], and in a convective region of deepwater formation [Watson et al., 1999].

From these field measurements and from theoretical considerations a rough overall picture of mixing intensity below mixed layer has evolved: rather low and uniform open ocean mixing, possibly further reduced in the vicinity of the equator and with hotspots related to continental shelves and regions of rough or steep topography. The contribution of a vmADCP based parametrization of diapycnal mixing, as attempted here, could be enhanced area coverage of mixing estimates at low cost (more or less as a byproduct of common research cruises), though confined to open ocean and the upper 500m up to now. And it may serve as a source of mixing estimate for groups that do not entertain time-, money-, and personel-consuming microstructure equipment.

4.2 Shear inferred from underway vmADCP

4.2.1 General processing strategy

We want to acoustically illuminate internal waves in the oceanic velocity field. This is not a very common purpose. Usually mean velocities and transports are in focus when doing acoustic measurements, and measured remains of internal waves are regarded as noise. Moreover we want to get an unbiased measure of internal wave shear variance (or shear power), and we want to achieve that from a cruising vessel, with a typical ship speed of 5 $\frac{m}{s}$ that is considerably higher than important parts of the internal wave phase velocity continuum. For these aims we have to deal with two main obstacles before obtaining useful finescale shear data from a cruising vessel: ADCP output data quality and Doppler shift of internal wave frequencies.

The issue of ADCP data quality is illustrated by the fact that needed precision of velocity data is 0.5 cm/s standard deviation of one velocity component, for a depth-binsize of 8 meters. This precision is needed in order to discern low but typical background internal wave shear variance of $1 \cdot 10^{-5}\, s^{-2}$ with confidence from instrument noise. Modern single-ping standard deviations of vessel-mounted ADCPs are 20 to 60 times higher [RDI-Teledyne, 2008].

The main problem with Doppler shift results from internal wave shear variance smeared to higher frequencies when observing from a moving platform. Shear variance at higher frequencies is prone to stronger attenuation in the measurement process, especially when doing time averages. This variance loss varies tremendously with varying velocity of the measuring platform.

To overcome these two main obstacles, we come up with a general processing strategy: Do all noise reduction on velocities derived from ADCP, then, based on cleansed velocities, calculate a descriptor for shear variance from vertical shear spectra (refer to figure 4.15 on processing scheme in subsection 4.2.7). As we have to reduce noise drastically in order to resolve low ('background') shear levels of the internal wave field, we start with taking every possible measure to reduce instrument noise when measuring. Then during post-processing, taking advantage of the fact that vmADCP velocity data is collected as a twodimensional field in depth and time, we do further noise-reduction by 2-D-filtering of velocity data. Then we derive spectra of total vertical shear

$$\Phi_S(m) = (\Phi_u(m) + \Phi_v(m)) \cdot (2\pi\, m)^2 \tag{4.1}$$

(with Φ spectral density and m vertical wavenumber) and correct for signal losses that were caused by the measurement process. The subsequent final step - winning a parameter from shear spectra that describes shear variance in a useful way - deserves some particular consideration in the following.

Internal wave spectra, namely distributions of energy and variance of vertical shear on space- and timescales, seem to be of similar shape in most of the inner ocean. That led to the formulation of an internal wave model by [Garrett and Munk, 1972] that was slightly modified in the following years to two main strains (the so-called GM76: [Garrett and Munk, 1975; Cairns and Williams, 1976] and GM81: [Munk, 1981]) and is vastly used as model representation of a saturated background state of internal waves. For analytical details refer to appendix A. We use GM76 with parameters $N_0 = 5.1 \cdot 10^{-3}\, rad/s$, $b = 1000\, m$ and $j^* = 3$ fitted to the region, following the method of [Cairns and Williams, 1976]. N_0 and j^* are near identical to the classic parameter choice, while b is lower than the classic value of $b = 1300\, m$, thus leading to slightly lower reference GM shear levels by a factor of 1.3.

An important feature the Garrett-Munk model catches is the nearly flat ('white') shear power spectrum. Deviating spectral slopes of -0.5 to $+0.5$ are not unusual to be found in the open ocean [D'Asaro, 1984; Duda and Cox, 1989; Gregg et al., 1993; Polzin et al., 1995]. What the Garrett-Munk-model catches not per se is the m^{-1} rolloff at vertical wavenumbers m greater than $O\,(0.1\, cpm)$, that was later found in observations. [Gargett et al., 1981] were first to deliver a composite spectrum of vertical shear over a wide wavenumber range, the idealized shape of which is commonly referred to as the canonical shear spectrum (see figure 4.4). The rolloff wavenumber band (or 'buoyancy subrange' [Gargett et al., 1981]) is understood as an intermediate band between a range of finescale wavelike motions that contains the main bulk of shear variance through to a microscale range of turbulent motions that finally dissipate that part of shear variance that was passed down. The transfer of shear variance to smaller scales in the rolloff band appears to be performed by waves Doppler-shifting and applying their shear on each other. The shear-variance-containing near white spectral band is characterized by the nondimensional energy level E which is proportional to shear spectral level Φ_S (refer to equation A.12 in appendix) and usually is greater or equal to the Garrett-Munk background energy level E_{GM}. So an increased internal wave field compared to background does exhibit higher spectral levels of the near white band: $\Phi_S > \Phi_{S,GM}$ which corresponds to $E > E_{GM}$. The rolloff band on the other hand does not rise in level in an increased internal wave field; it just extends farther to lower vertical wavenumbers.

To simplify speaking and thinking of elevated internal wave field spectral levels, we coin the term GM-level G for the ratio

$$G = \frac{\Phi_S}{\Phi_{S,GM}} = \frac{E}{E_{GM}}. \tag{4.2}$$

G is equivalent to the nondimensional $E_1 = \frac{E}{E_{GM}}$ used by [Polzin et al., 1995], also adopted by [Kunze and Sanford, 1996].

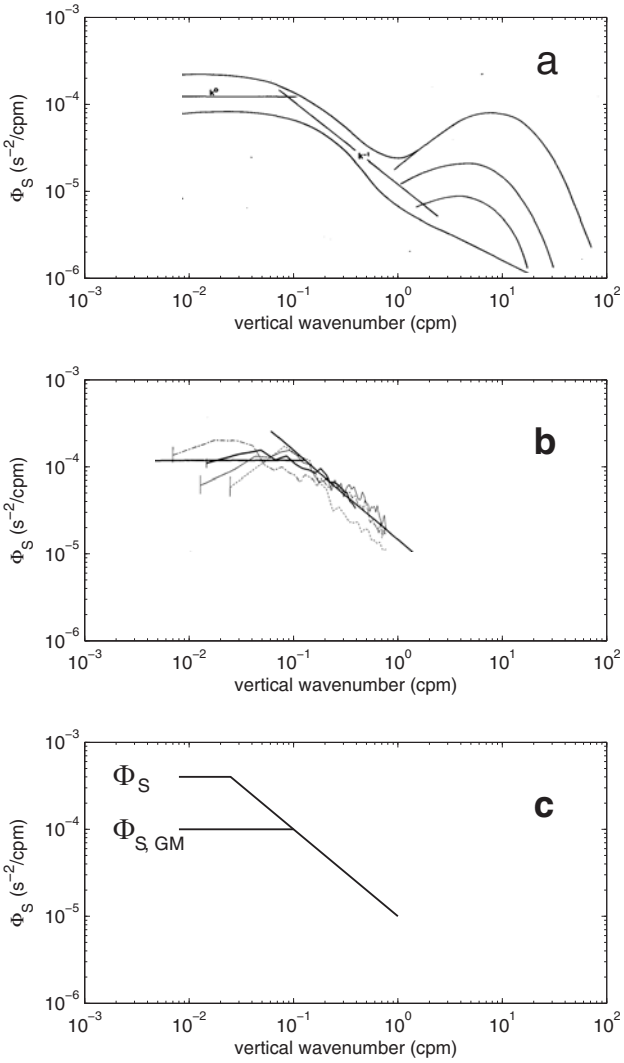

Fig. 4.4: Spectra of vertical shear. a) Composite spectrum brought forward by [Gargett et al., 1981] after measurements in three overlapping wavenumber bands. b) Scaled spectra measured by [Polzin et al., 1995] at different midlatitude sites. c) Idealized 'canonical' spectrum at background internal wave activity ($\Phi_{S,GM}$) and increased activity (Φ_S). Three main ranges are discernible: the flat saturated range of wavelike motions, the buoyancy subrange at slope -1, and the range of turbulent motions.

The aforementioned properties of the canonical shear spectrum have consequences for shear determination. There are at least three possible ways to characterize shear by aid of a calculated parameter: a) Calculate shear directly by vertical first-differencing of observed velocities, just taking the resolved wavenumber range of the instrument and its output as is. The result is some fraction S^2_{direct} of the total shear variance of the internal wave field. b) Calculate shear directly from velocities, but ascertain to resolve virtually the whole vertical wavenumber band up to a defined limit, and correct for shear variance losses from unwanton smoothing during the measurement process. A prominent example of this method has been given by [Gregg, 1989], where shear variance has been resolved down to a vertical wavelength of 10 meters (reported as S^2_{10}). c) Take shear spectral level of near white band Φ_S as a describing parameter, without caring for total shear variance of the internal wave field (i.e. the complete integral of the shear spectrum). All three methods are illustrated in their effect in wavenumber space in figure 4.5, panels a,b,c respectively.

We choose method c) due to several reasons. The range of wavenumbers resolved by vmADCP (in our case 1/128 cpm to 1/38 cpm) lies in the near-white spectral part anyway, so we could only report a fraction of total S^2 due to this limited wavenumber range. As it is not completely clear to what degree internal wave spectra follow the canonical spectrum, i.e. how the shear spectrum continues to lower wavenumbers and at what exact higher wavenumber the roll-off starts, we would not be able to confidentially correct for the missing wavenumber range. So method b) is out of reach. Moreover, method b) has not stood the test of time (see [Gargett, 1990] commenting on [Gregg, 1989]). Gregg calculated S^2_{10} up to vertical wavelengths of 10 meters, a parameter that is less and less sensitive to changes in the energetic part of the shear spectrum with increasing internal wave activity, as integration of the canonical shear spectrum delivers $S^2_{10} = S^2_{10,GM} \cdot (1 + ln\,[E/E_{GM}])$. This effect is due to the special character of the spectral rolloff and in practice renders S^2_{10}-based discrimination between high internal wave levels unsatisfactory. Method a) is worse than b) in that it does not deliver a defined fraction of total shear variance, and in that observed shear quantity varies with instrumentation. Nevertheless method a) can take advantage of its typically limited wavenumber range and might more adequately than b) represent relative changes of shear variance at increased internal wave activity. The price for that is a unique intransferable parametrization necessary for each set of instrumentation and configuration, without possibility to cross-check values to other observations. Method c) combines linear dependence on shear variance level in the interesting wavenumber band with not being forced to resolve every wavenumber and with delivery of a defined quantity that can be compared to reported values won by different instrumentation and settings. To keep clarity concerning names of used shear-describing parameters, we avoid S^2 and use S^2_{direct}, S^2_{10} and Φ_S where appropriate.

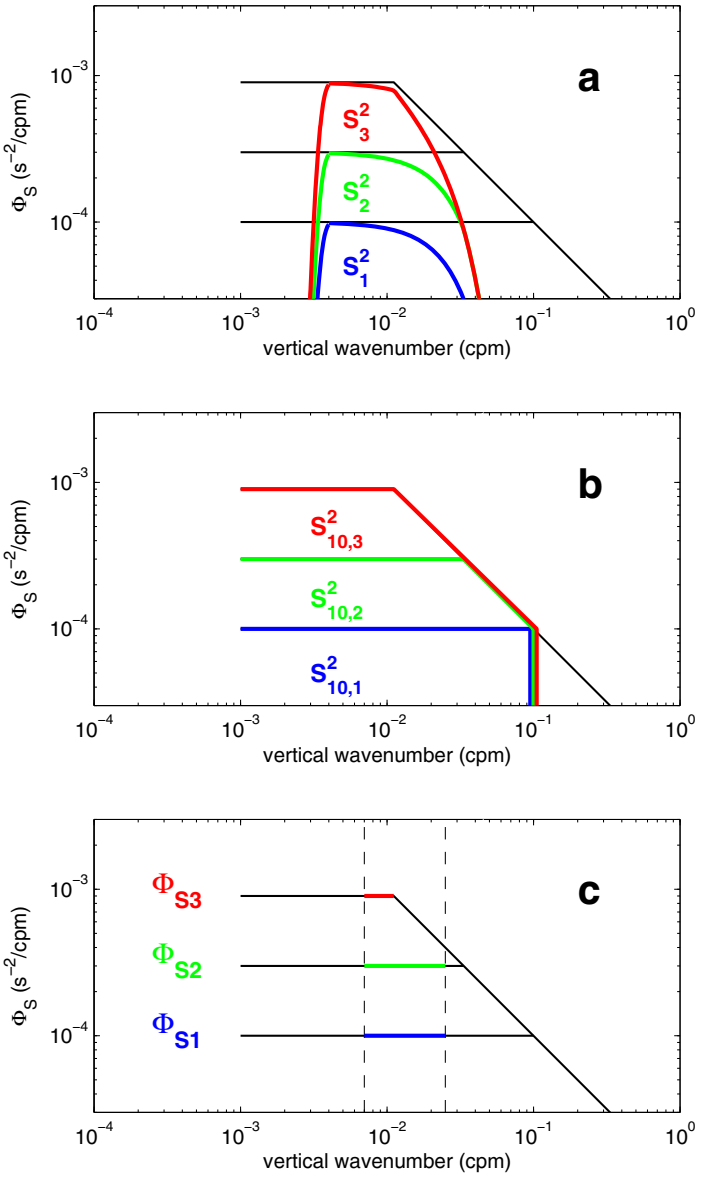

Fig. 4.5: Three methods to derive a parameter that describes shear variance, as seen in wavenumber space. a) S^2_{direct} from first differencing horizontal velocities. High wavenumber end limit is attenuated at wavelengths close to 2 times binsize. b) S^2_{10} from wide wavenumber range resolved velocities, after correcting for attenuation bias. c) Φ_S as level of flat spectrum part.

Figure 4.5 also reveals a problem all methods share: given the canonical shear spectrum applies, the maximum GM-level that can be determined is limited by the lowest vertical wavenumber resolved by the method. In the open ocean, internal wave fields of G = 10 do occur - rarely but regularly. Thus the range of the used instrumentation should be that large, that the lowest vertical wavenumber resolved in high quality is lower than 0.01 cpm.

The following sections treat the necessary data processing steps in more detail, beginning with ADCP data acquisition.

4.2.2 vmADCP configuration and inherent smoothing

We already start with acoustic instrumentation of highest quality: RDI Teledyne's Ocean Surveyor vessel mounted ADCP. This instrument's emergence around the year 2000 plus improved shipboard navigation and computer capacity has soothed ancient ADCP data quality problems markedly [Fischer et al., 2003]. The Ocean Surveyor is capable to switch between long range (narrowband, NB) and precision (broadband, BB) mode, has improved range compared to its predecessors, and firmware improvements that reduce instrument noise. Navigation data quality boosted with GPS enhanced precision, and modern GPS attitude arrays allowing high quality heading readings. Computer power increased continuously, then allowing single ping recording with subsequent near infinite post-processing possibilities.

Both used vessels have a hull mounted RDI Ocean Surveyor phased array ADCP of 75 kHz. Most data were recorded in the more precise broadband mode (with 12cm/s single-ping standard deviation at 8-meter bins [RDI-Teledyne, 2008]) - but we will also consider processing of narrowband mode derived data (with 30cm/s single-ping standard deviation at 8-meter bins), as most existing velocity data of the past 10 years have been recorded in NB mode. BB mode pays for its greater accuracy with lower range, lower robustness against rougher sea conditions and more sensitivity to acoustic interference with other acoustic instrumentation. Thanks to the usual calm sea state of the region and because interfering acoustic devices such as Doppler velocity log or sweep echosounder could be spared, we experienced no severe problems with BB mode. There exists a 10-day-sequence of NB mode data, mainly recorded during transit to the survey region on cruise MSM10/1. We will use this data to test feasibility of shear variance deduction from NB data (subsection 4.2.6). Bin size was chosen as 8 meters, which resulted in a typical range of 550m to 600m for BB mode and 650m to 700m for NB mode. Swath area at range depth is 500m in effective diameter for BB mode and 600m for NB mode. Pingrate was chosen the maximum possible at these settings and was $36\,min^{-1}$ (1.65s ping interval). We chose the usual single-ping recording in order to be free in post-processing.

The ADCP smoothes vertical velocity structures, inherently caused by the finite length of the acoustic ping traveling through the water and by the range gating into finite bin lengths when receiving the echoes. This results in a triangu-

lar window smoothing effect. When working in wavenumber space, the equivalent transfer function is $sinc^4\,(m \cdot \Delta z)$ with m vertical wavenumber, Δz bin size and $sinc(x) = sin(\pi\, x)\,/\,(\pi\, x)$. [Polzin et al., 2002] treat these issues in greater detail.

Furthermore we find a smoothing effect from the vessel's heave and tilt movements that basically cause the returned acoustic signals to be ascribed to an incorrect depth, differently for each beam. This effect we simulated for the typical heave and tilt behavior during the two cruises (pitch and roll less than 2 degrees, heave less than 3 meters). Its transferfunction can be described to a satisfying degree by $sinc^3\,(m \cdot \Delta z)$.

We don't need to care about smoothing caused by first-differencing the velocity profiles, as we do not first-difference, but derive shear spectra from velocity spectra by multiplying power spectral density by $(2\,\pi \cdot m)^2$.

All these effects occur independently of ship speed, and attenuate the recorded signal strength predominantly at the high wavenumber end. They are included to processing when compensating shear spectra for signal losses in subsection 4.2.4.

4.2.3 Preaveraging of velocity data

Before filtering the recorded velocity data, is it necessary to time-average the single-ping data at all?

From a practical view, doing time averages of pings in a modest amount is merely unavoidable, as i) bad bins have to be filled before processing, ii) it is desirable to work with entities of uniform duration and error level when processing (ping frequencies are prone to some irregularity when pinging as fast as possible) and iii) doing data processing for a whole cruise of some weeks should be possible on a modern personal computer within a manageable timespan. A practical lower limit from experience is 1-minute-averages. Further, there is not much sense in doing shorter averages, as a research vessel in full speed of typically 12 knots covers a distance of about 350m during 1 minute, a length on the order of the ADCP footprint.

On the other hand averaging time should not much exceed 1 minute if it can be helped. Generally, when lumping single ping data to averages, the vessel movement translates this to a combined time-and-horizontal averaging, which unpurposefully also causes a reduction in registrable vertical shear variance. The amount of this reduction depends on wave crest slope, ship speed and averaging time. So percentage of retrieved variance when cruising varies with vertical wavenumber and speed. Figure 4.6 shows the pure shear signal reduction effect of time averaging when on station or moving at typical transit speed of 12 knots. The quantification of the effect relies on the Doppler-shifted GM76 model internal wave shear field, dependent on vertical wavenumber and observed frequency (see appendix A for deduction).

Each frequency has contributions from a continuous range of horizontal wavenumbers. For known vertical and horizontal wavenumber, the fraction of shear variance lost by averaging along a path of the moving ship may be quantified, and then the integrative effect for each vertical wavenumber at a given average time and ship speed may be calculated from integration. Generally, more shear variance is lost at higher vertical wavenumbers as they go in hand with higher horizontal wavenumbers (at constant frequency) and thus are more prone to smoothing by horizontal averaging.

When the ADCP is not moving, long-time averaging is possible and will hardly downgrade shear variance data, as the overwhelming part of shear variance is contributed by near inertial waves. The fast moving vessel makes the huge difference. In the past there has been excessive averaging of underway ADCP data caused by memory restriction of then available computer systems. But even 10min-averages lead to a remarkable permanent shear signal loss when moving at 12 knots. That means that signal loss is highly dependent on ship speed, and this is a nuisance when doing typical survey cruises with their frequent speed changes.

So we stick to the shortest meaningful preaveraging of 1 minute. Our collected velocity data after 1-min-averaging retain a standard deviation of 3cm/s in BB mode and 7.5cm/s in NB mode for each horizontal velocity component (estimated from spectra). These numbers are slightly above the expected standard deviations of 2cm/s and 5cm/s, respectively, based on manufacturer's product information [RDI-Teledyne, 2008].

4.2.4 Shear spectra from filtered velocities

Restricted to 1-min-averages, noise is still too high to allow a satisfactory resolution of low 'background' shear levels of the internal wave field. The means of further noise reduction is 2-dimensional spectral filtering of velocity data with one single universal filter for the whole velocity dataset of one cruise. Only changes of configuration such as changing from BB to NB mode or use of a different vmADCP unit with subsequently altered noise level warrants the use of a different filter design. For the present Ocean Surveyor ADCP datasets, we filter overlapping velocity data segments of 64 bins x 256 minutes, that is 512 meters x 256 minutes, and then merge the filtered segments to a filtered velocity dataset.

When looking at example 2-D spectra (vertical wavenumber, frequency) of measured velocities, their similarity to GM76 model spectra $F_u(\omega, m)$ A.3 is apparent (figure 4.7). That is why filter design can be based on GM76 model velocity spectral density as the expected signal, and the known white noise level of unfiltered 1-min-averaged velocity data. The filter function is then determined in the Wiener optimum sense as signal power density divided by signal power density plus noise power density. As measured velocity spectra vary with ship speed - because the internal wave field is Doppler-shifted -, and with the intensity of the internal wave field compared to

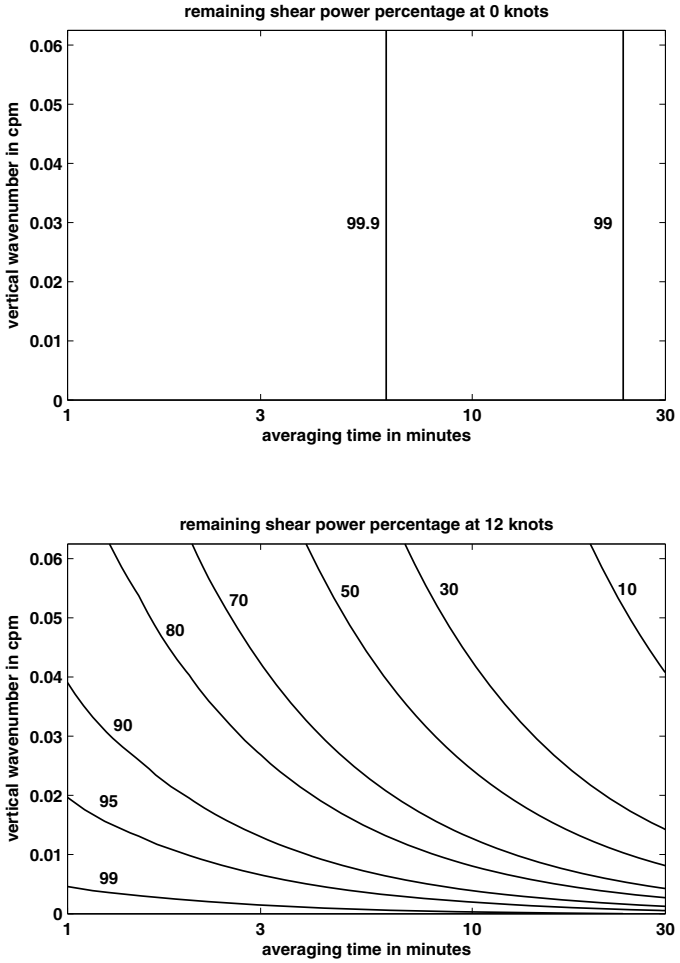

Fig. 4.6: Percentage of vertical shear variance retrievable after time-averaging underway recorded internal wave field velocities (modeled by GM76 spectrum). Upper panel: zero relative velocity at station. Lower panel: at typical cruise speed of 12 knots.

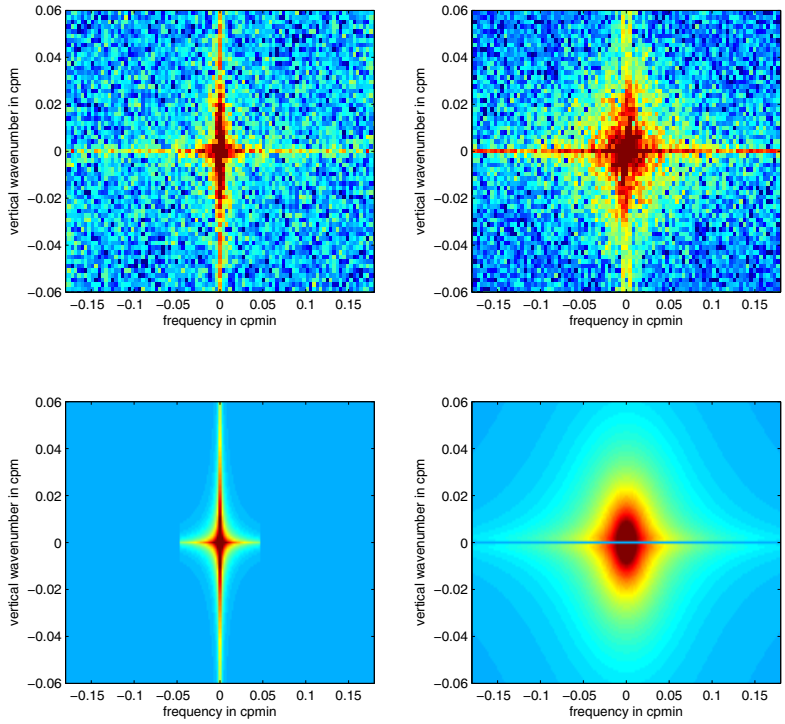

Fig. 4.7: Example 2-D energy spectra in vertical wavenumber frequency space. Upper row: power spectra of example measured velocities. Lower row: GM model at G = 3, offset by ADCP noise level, spectra as of $F_u(\omega, m)$ A.3 and $F_{u,v_0}(\omega_t, m)$ A.15. Left column: zero mean relative velocity. Right column: relative velocity of 10 knots. Most prominent difference of observed to model spectra is the horizontal line at vertical wavenumber zero that is caused by "barotropic" noise due to the ship's pitch, roll and heave motions.

the GM base level (G), the filter to be applied has to be chosen by compromising between some quality criteria.

Although doing velocity filtering, quality criteria for filter choice concern the quality of the final outcome: the shear spectra resulting after calculating vertical spectra of the filtered velocities. Resulting estimated shear variance from the filtered velocity field i) shall not be biased by ship speed (systematic corrections allowed); and ii) the noise level after filtering should allow detecting shear variance level corresponding to GM model shear variance level (G = 1) with confidence. To achieve the best possible signal to noise ratio, there will also be importance to: iii) be able to use a broad wavenumber band to infer shear level; iv) lose only little signal power to the filter, so that compensating corrections to the signal by transfer function can stay moderate. Large compensations would also mean large amplification of noise.

After an empirical optimum search, the filter function deemed best is based on the Doppler shifted GM76 velocity spectrum $F_{u,v_0}(\omega_t, m)$ A.15 for maximum ship speed

of 12 knots at G = 3. That keeps much of the signal and thus keeps necessary compensating signal corrections as small as possible; but also reduces enough noise to detect shear levels of G = 1 (see figure 4.8 for the chosen filter function and its consequences in the shear spectrum). Using the highest practical ship speed of 12 knots for design means incorporating nearly the same amount of signal in the filter interior for every ship speed below 12 knots and thus low influence of ship speed on necessary signal compensation by transfer function. The usable wavenumber band is limited at low wavenumbers by the number of bins that can meaningfully be used for calculation of shear spectra, additionally narrowed by the fact that the spectrum at the lowest wavenumbers can't be estimated accurately due to detrending and windowing. The upper wavenumber band limit is chosen at the break-even point of marginal error when calculating spectral level; that means choosing a wavenumber limit one step higher would effectively increase the overall error of the estimated spectral level, because the additional error from instrument noise multiplied by the necessary transfer function would outweigh the precision gain that one additional spectral value would produce.

After having applied the chosen filter to the 1-min velocity data, calculation of vertical shear spectra is achieved by choosing 48 bins 150m to 520m (BB) and 64 bins 150m to 650m (NB) for each 1-minute velocity ensemble of each velocity component. After detrending, a 10% cosine square taper is applied to the velocity data. The resulting velocity power spectrum is corrected for the loss caused by windowing and multiplied by $(2\,pi \cdot m)^2$ to produce shear power spectrum. Caused by the detrending-windowing preparation, modes 0, 1 and 2 of the spectrum are too attenuated and erroneous, so that the useable wavenumber band is limited to the low wavenumber end by 3/(48*8m) = 0.0078 cpm for BB mode and 3/(64*8m) = 0.0059 cpm for NB mode.

The resulting shear spectra are still attenuated from time-averaging of single-ping velocities, ADCP inherent smoothing, and filtering, particularly in the higher wavenumbers. So compensation for these signal losses is necessary in order to infer shear spectral level. Compensation factors for each wavenumber are a function of relative shear level G and to a lesser degree of ship speed. They are won from GM76 model 2-D-velocity power spectra at relative shear level G and ship speed, then applying ADCP smoothing plus filtering to the modeled spectra, integrating along frequency, transferring to shear spectra, then finally calculating total signal loss from comparison of attenuated shear spectra to the GM76 model shear spectrum at level G.

As compensation factors depend on shear spectral level itself, a quantity not known in advance, we have to enter a three-step process and estimate shear spectral level from the attenuated shear spectrum first, before the attenuated shear spectrum may be corrected. The first shear spectral level estimate is won in two steps. At first, weighted averaging of attenuated shear levels in the useable wavenumber band gives G', a too low estimator of shear level. The weights crudely mirror the greater accuracy of lower wavenumbers, in that they are chosen as $w_i = 1 - (i-1)/n$ for

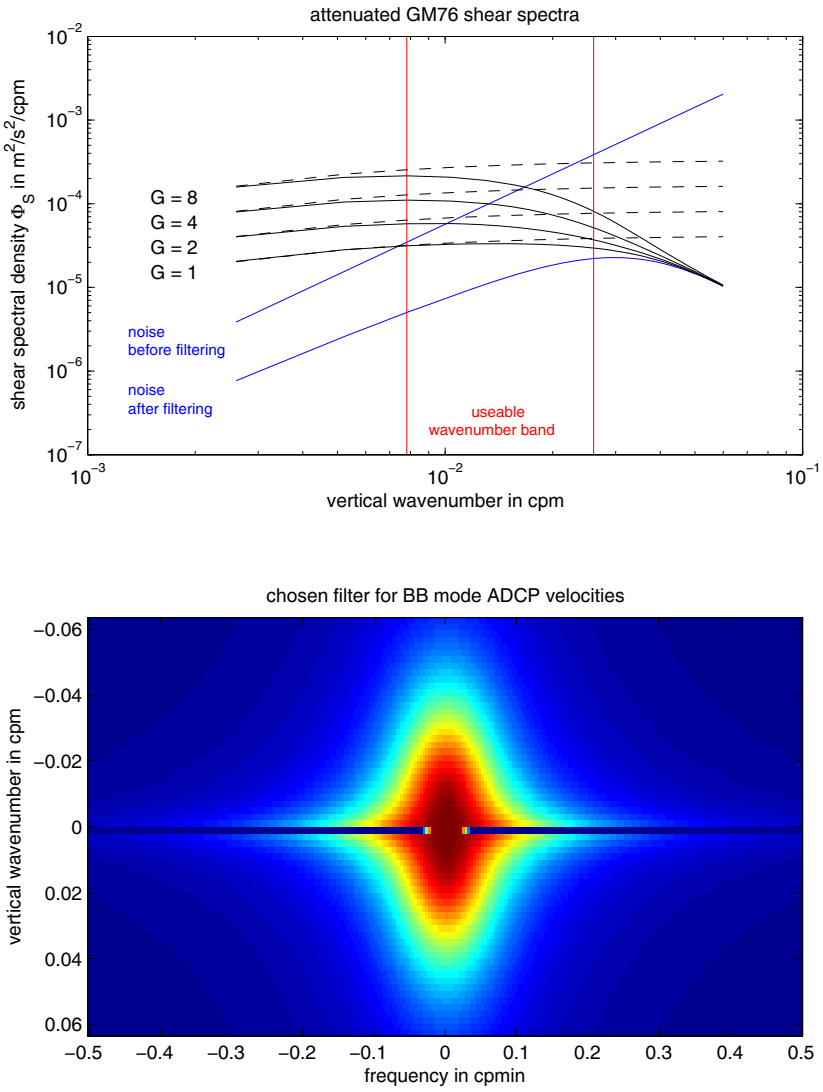

Fig. 4.8: Filter design. Upper panel showing GM76 shear spectral levels before (dashed black) and after (solid black) applying all known smoothing effects due to the ADCP measurement and filter application. Blue lines demonstrate noise reduction from filter use. Red lines mark useable wavenumber band. Lower panel showing chosen best compromise velocity filter. Blanking at vertical wavenumber zero is to eliminate ship motion noise (as visible in figure 4.7). Illustrations are for BB mode. NB mode is similar, but with elevated noise level and a shifted and narrower useable wavenumber band.

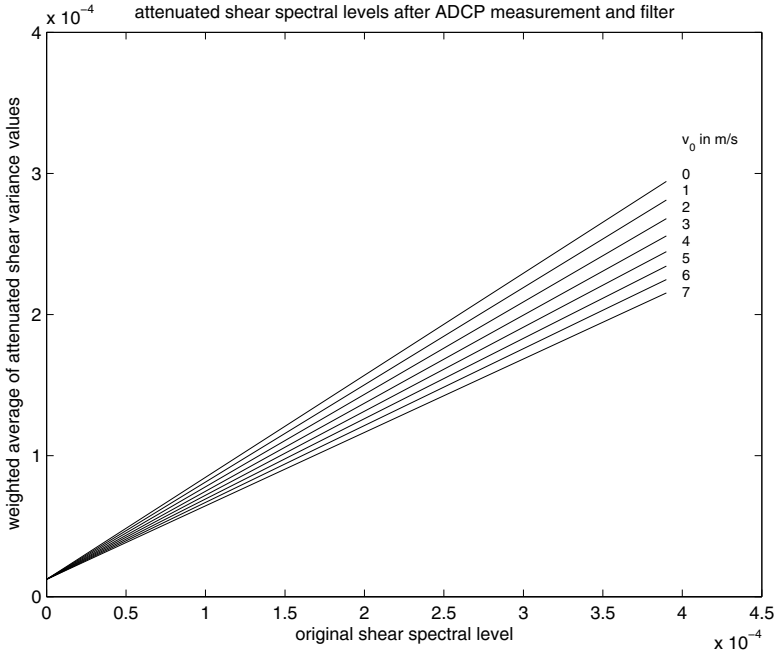

Fig. 4.9: Attenuated mean shear spectral level after applying all known smoothing effects due to ADCP measurement and filtering to GM76 model spectra - at different spectral levels and ship velocities. Inverse use of the function is used to infer Φ_S estimates from measured shear spectra at known ship speed.

$i = 1...n$ and n number of used wavenumber points. The estimated corrected shear level G is then inferred from G' and ship speed by inverse use of the GM76 modeled signal loss (see figure 4.9), as described above. Finally correction factors for each wavenumber may be won from estimated G and ship speed, and be used to correct attenuated shear spectra.

In practice we derive shear levels and spectral corrections from ensembles of 10 averaged shear spectra in order to reduce method-inherent error of the fast Fourier transform.

4.2.5 Scatterer influence

The naturally uneven distribution of scatterers in the water column leads to ADCP shadow pictures of something resembling target strength gradient in the along-ship velocity component (figure 4.10). This effect is proportional to ship speed. It is basically caused by the imperfectness of the ADCP's acoustic beams, as these contain sidelobes that add a small fraction of erroneous Doppler shift to the main lobe's Doppler shift. For the sidelobe part that is more perpendicular than the main lobe, the overall effect is a bias of beam-observed velocity towards zero, which leads to a bias of the shipspeed-corrected velocity towards ship speed. As the echo of this sidelobe part returns before the echo of the main lobe for the same depth,

the bias affects observed velocity at a shallower nominal depth than the scattering layer actually is. For the sidelobe part that is more horizontal than the main lobe, contrary considerations apply. Some commentary and illustration to this problem may be found at University of Hawaii's Current Group internet presence [UH, 2010].

This scatterer effect is of high importance here, as structures are much in the vertical wavenumber range of internal waves. If we were mainly interested in mean velocities, bias might cancel out to a good degree, but when looking for variance, positive and negative derivations both add to variance bias. Processed along-ship shear variance proves to be considerably higher than across-ship shear variance - at a typical transit ship speed of 12 knots they differ by a factor of 3 (cf. figure 4.11). There is no known reasonable way to correct for this bias. So the along-ship component has to be discarded when deriving shear variance at times the ship is moving.

For the processing this means: We have to use velocity components turned to ship coordinates, and only use the across-ship component. Only at station there is no discernible difference between along-ship and across-ship component's shear variance, so both components may be used then. Using only one velocity component to derive shear variance will mean that shear power level derived from this single component must be doubled in order to compare it to the GM model. And it will mean some lower accuracy of estimated shear variance levels.

There might be concern that filtering the across-ship velocity component instead of filtering the velocity components in earth coordinates might result in additional signal loss. The vessel's turning manoeuvers indeed lead to spurious undulations in the velocity record and mimick an additional Doppler shift of the internal wave field towards higher frequencies. But regarding the frequency characteristics of the applied filter and the range of vertical wavenumbers -0.026cpm to 0.026cpm we use, it is conceivable that only fast turns of considerable angles would lead to discernible shifts of power into stronger attenuated frequencies - say 360 degree vessel turns in 10 minutes. Manoeuvers of this suddenness are extremely rare and have to be treated with care if they occur. Typical vessel manoeuvers of turning in for a station and then staying for an hour or more before turning out again, will not lead to discernible stronger attenuation.

4.2.6 Plausibility check and errors

To check the performance of the method laid out in this section and the plausibility of its outcome, look at observed shear spectra and shear spectral levels during the two cruises. Distributions of observed relative shear spectral levels G (figure 4.11) indicate plausibility in 3 points:

1. While relative shear spectral level G as derived from the along-ship velocity component in full ship speed is vastly biased to threefold values caused by patchy distribution of acoustic scatterers in the water column (subsection 4.2.5), all other

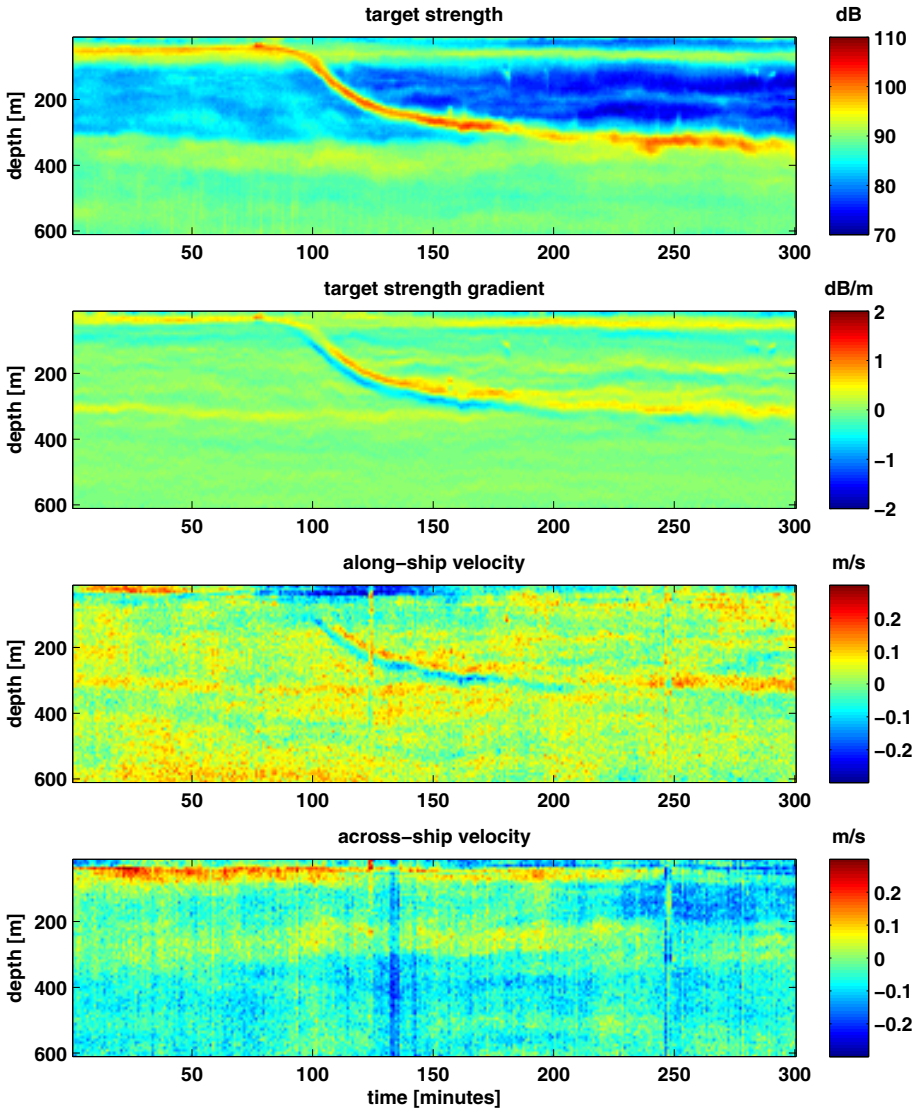

Fig. 4.10: A typical example of uneven scatterer distribution in the water column as seen in different ADCP derived parameters. Uppermost panel: target strength deduced from echo intensity. Upper middle: Vertical gradient of target strength. Lower middle: along-ship velocity component measured at 10 knots ship speed, with many of the target strength inhomogeneities to be identified as ship speed bias pattern. Lowermost panel: across-ship velocity unaffected by scatterer inhomogeneity.

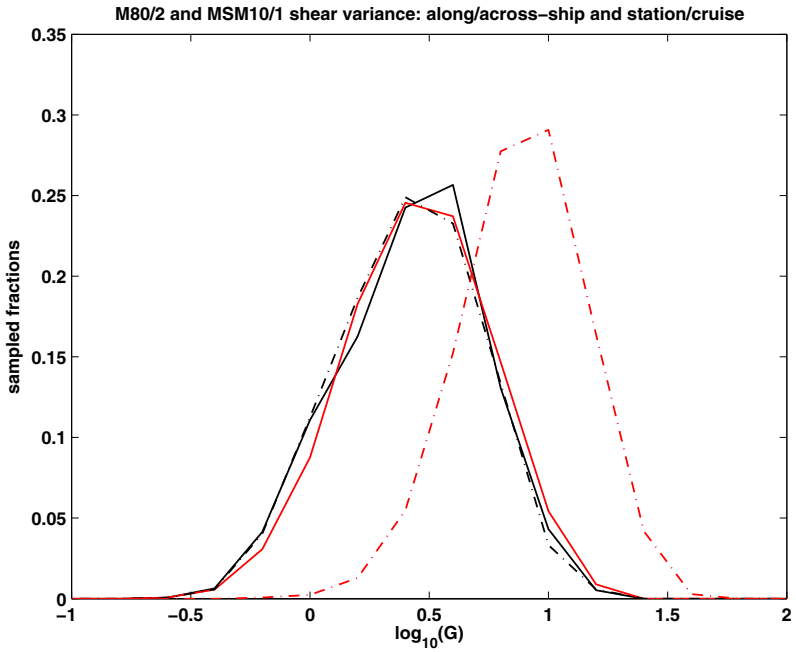

Fig. 4.11: Distributions of deduced relative shear spectral levels G, from all available data in BB mode. Black lines at stations, $v_0 = 0$, red lines moving, $v_0 \geq 4.5\,\frac{m}{s}$. Solid lines: G from across-ship velocity component; dash-dotted lines: G from along-ship velocity component.

distributions agree. Occurrences of G on station for both velocity components and from across-ship velocity component in full ship speed do not differ systematically. By keeping to across-ship component for processing, there's no ship speed bias to be expected in G records of entire research cruises. Using both components when on station may be favourable as error will be lower.

2. The shape of shear level distributions found all over Guinea Dome Region (the distributions here interpreted as probability densities) affirms the heuristically based prejudice to find approximately lognormal distributions connected with mixing parameters. It has to be taken into account though, that G estimates carry lognormal distributed errors and thus smooth observed distributions and slightly bias them towards lognormal.

3. The observed typical shear spectral level is not GM76 'background' G = 1, but rather G = 3 as median value, at least in Guinea Dome Region. The range of observed shear spectral levels is mainly limited by G = 1, as expected background, and G = 10. The smooth tailing of the distributions suggests that these limits do indeed represent limits in the true G distribution, as an 'aliasing' of higher/lower G values into the observed range should be visible as distortion of the distribution. This is no strict argument, especially because a detection maximum about G = 10 is possible in our ADCP configuration, if natural occurring shear spectra are well represented by the canonical shear spectrum (compare figure 4.5 and remarks

in subsection 4.2.1). But other measurements of internal wave shear also do not exceed G = 10 in the open ocean, e.g. [Polzin et al., 1995] in Atlantic midlatitudes and [Dengler and Quadfasel, 2002] in equatorial Indian Ocean.

Also when checking the corrected vertical shear spectra (figure 4.12), those resulting from ship's stations and from ship's full speed do not differ markedly. There also is no discernible strong difference emanating from bottom topographic influence. 'Background' shear level as expected from GM76 model is resolved without visible influence of noise at higher wavenumbers. For modest shear levels G < 6, spectral shapes are about flat, as expected in the wavenumber band covered. A slightly negative slope flatter than $m^{-0.5}$ seems to predominate, which is hardly significant in light of the confidence limits but also not disturbing, as in open ocean slight spectral deviations from m^0 seem to be quite common [D'Asaro, 1984; Duda and Cox, 1989; Gregg et al., 1993; Polzin et al., 1995].

For the rather rare events G > 6 (spanning a wide but sparsely populated range up to G = 25) there's more variability in spectral shape. These highly energetic spectra seem to roll off from about the expected canonical critical wavenumber (e.g. $m_c = 0.01\,cpm$ for G = 10) at a slope roughly canonical ($\approx m^{-1}$), but their rareness of observation and the averaging of spectra over the wide span of G values with each quite uncertain spectral shapes make analysis uncertain here. So non-GM-behaviour of highly energetic internal wave fields may also be a probable explanation.

All remarks up to here have been for processed ADCP data won in BB mode. There also are some days of NB mode data processed from mostly transit during cruise MSM10/1, that have been checked analogous to the previous checks for BB mode data (figure 4.13 to be compared to figures 4.11 and 4.12). Although NB data is little compared to the amount of BB mode data, and average spectral shapes and distributions of shear level are much noisier, there is no strong indication that Ocean Surveyor ADCP in NB mode should not deliver plausible shear spectral levels of the internal wave field, given appropriate filter design and adapted processing. Main differences to BB mode data are a higher noise level and a slightly greater depth range that both affect the usable wavenumber band of calculated shear spectra. The overall effect is a shift towards lower wavenumbers while the usable band is narrowing.

The total error of shear level estimates stems a) from ADCP noise level as modified by shear deduction, by filtering and by applying the transfer function, b) from uncertainty about the applicability of GM76, that determines the transfer function, and c) from estimating spectra via Fast Fourier Transform [Press et al., 1992]. Contribution a) varies with shear spectral level as relative importance of noise level and compensation factors are different at different G. Contribution b) is fundamentally unknown but estimated as 25% for BBmode (45% for NBmode) based on the feeling that deviations from GM spectral shape should not exceed the effect and amount of Doppler shift at full ship speed, i.e. passing energy to higher frequencies and thus beyond the filter horizon. This is a rather crude estimate, and therefore is doubled

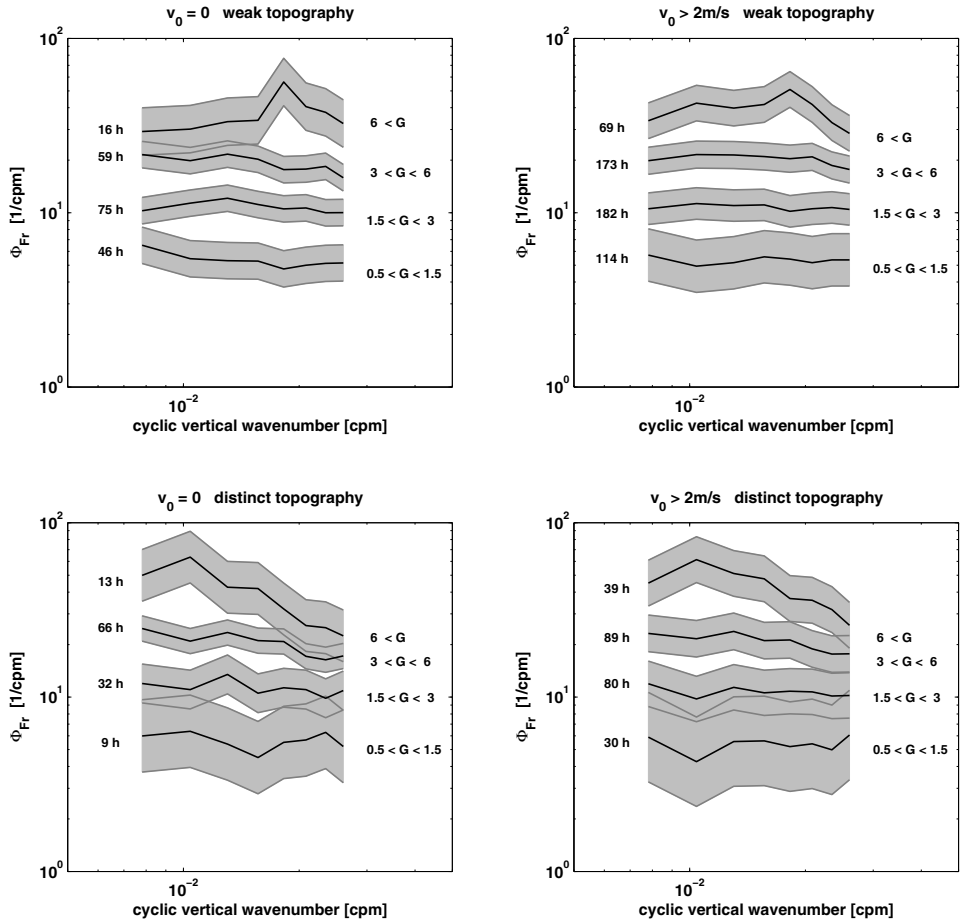

Fig. 4.12: Averaged shear spectra for 2 cruises in Guinea Dome Region after conditional sampling for spectral level classes, ship speed and assumed possible topographic influence. Confidence limits in grey are 95% level. Total hours of data contributing to averages given at left flank of spectral density lines. G is relative shear spectral level compared to GM76. Φ_{Fr} is shear spectral density scaled to buoyancy frequency squared, N^2. Individual spectra usually look noisier and often chromatic.

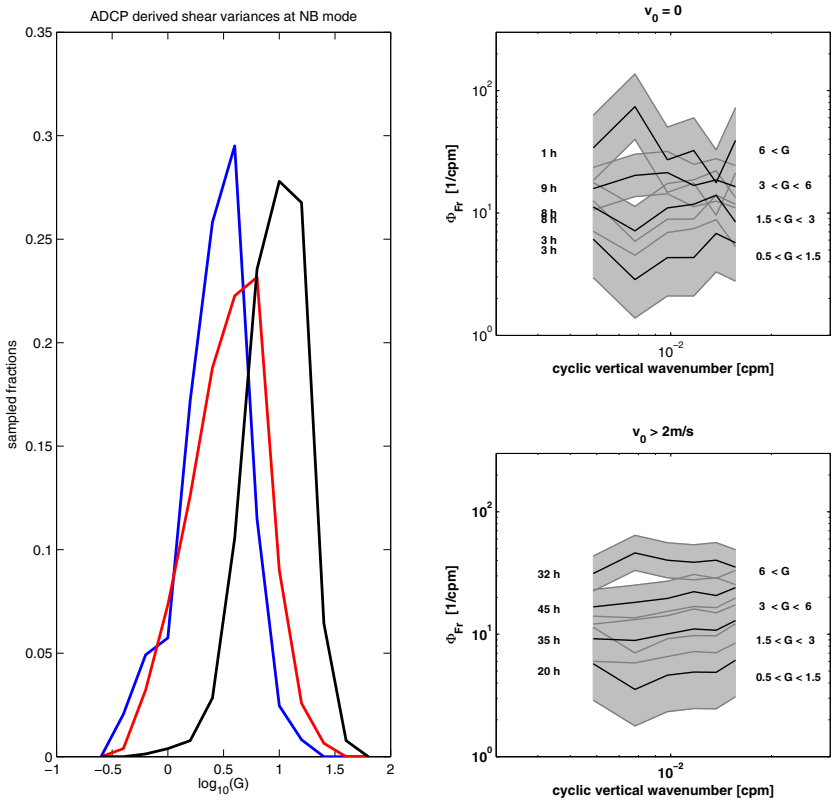

Fig. 4.13: Quality check for measured shear spectra when ADCP is in NB mode. Left panel analogous to figure 4.11 (blue: $v_0 = 0$, along-ship and across-ship G merged as station data is scarce; red: $v_0 \geq 4.5\,\frac{m}{s}$ across-ship component; black: $v_0 \geq 4.5\,\frac{m}{s}$ along-ship component). Right panels analogous to figure 4.12 without differentiating for topography.

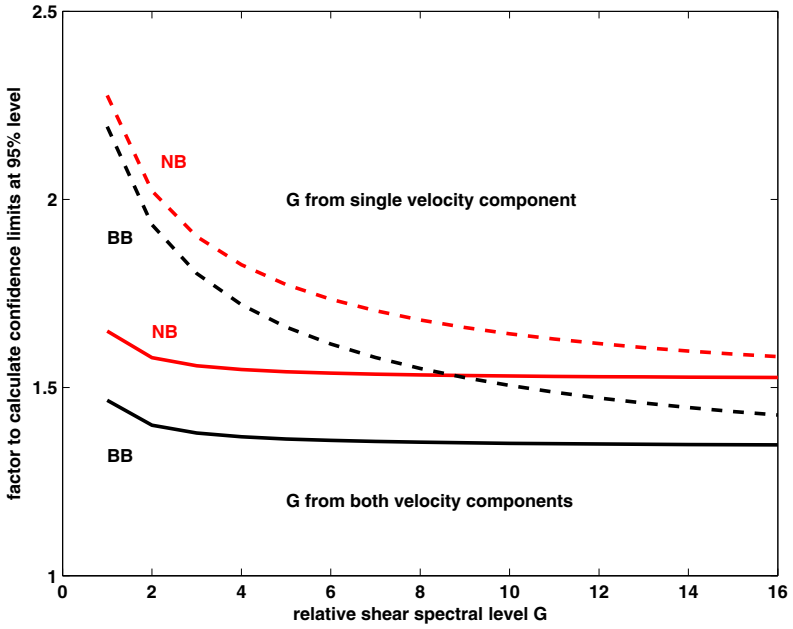

Fig. 4.14: Factors to determine 95% confidence limits for G measured and calculated for ensembles of 10 1-minute values. Error contributions from ADCP noise and power spectral density estimation are accounted for.

for safety. On the other hand there is not too much fear that the internal wave field could dramatically deviate from GM76, based on eyesight (figure 4.7) and based on observed shear spectra (figure 4.12). Total errors resulting of contributions a), b) and c) for averaged ensembles of 10 1-minute spectra are given here as factors, to be employed to compute confidence limits at 95% level (figure 4.14). When deriving shear level estimates from only one velocity component instead of both, an additional error occurs, as both velocity components are not fully dependent. The estimate for this error contribution is based on calculations from observed shear levels at station, where both components are available.

The error can be partly reduced by averaging over several ensembles of 10min. But shear level data resulting from across-ship velocity component shows prominent temporal autocorrelation. The integral timescale of shear level timeseries is 160 minutes - a fact resulting from a combination of the internal wave field changing in time and space and the ship's turning and its changing between station and transit. So essentially there is one independent value every 3 hours when doing a typical research cruise.

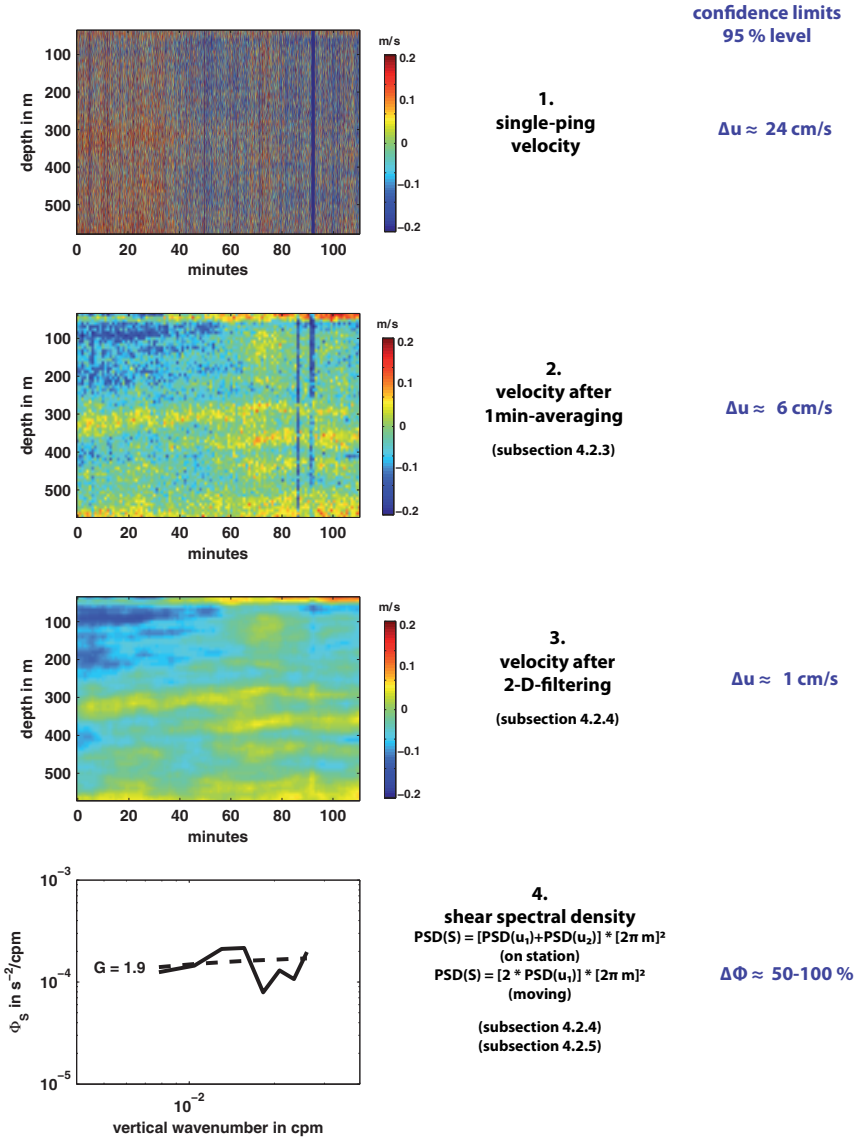

Fig. 4.15: Summary of processing steps and their effect on velocity data and error margins.

4.2.7 Summary: Processing of vmADCP derived shear levels

Several problems have to be addressed in order to estimate internal wave activity from vessel mounted ADCP records: some are generally inherent to ADCP use (rather huge noise reduction necessary; inherent ADCP smoothing), and some are special 'underway problems' that prove to be more severe (signal loss by horizontal averaging, Doppler shift of IW field, one velocity component spoiled by uneven distribution of scatterers).

We follow the strategy to confine signal-to-noise enhancement to the main step of 2-D-velocity filtering, as here is the place and possibility to do 'chirurgian' separating. Preaveraging is too rough an instrument, and is thus kept to the minimum reasonable amount.

Filter design is oriented at Wiener optimal filter design and done for the 2 modern ADCP configurations (OS-BB, OS-NB). For older shipboard systems before the year 2000, filter design is possible (at a standard deviation of 1-minute-average velocities of 0.1m/s), but usually velocities have been ensemble-averaged heavily - up to 30 minutes - and no rawdata on shorter timescales are available. Criteria for choice of an optimum filter are met as a compromise, as the signal is quite variable in time and space. Resulting from the different noiselevels, filters look different for the 2 ADCP configurations, with the BBmode filter keeping a better signal to noise ratio, enabled by its superior accuracy. Useable wavenumber band for shear variance evaluation is different for the 2 ADCP configurations as well, with a slight advantage for BBmode.

As a closing point, not only do shear spectra result from this processing, but as a byproduct clear velocity and shear graphs emanate (figure 4.16) - for NB mode not much worse than for BB mode.

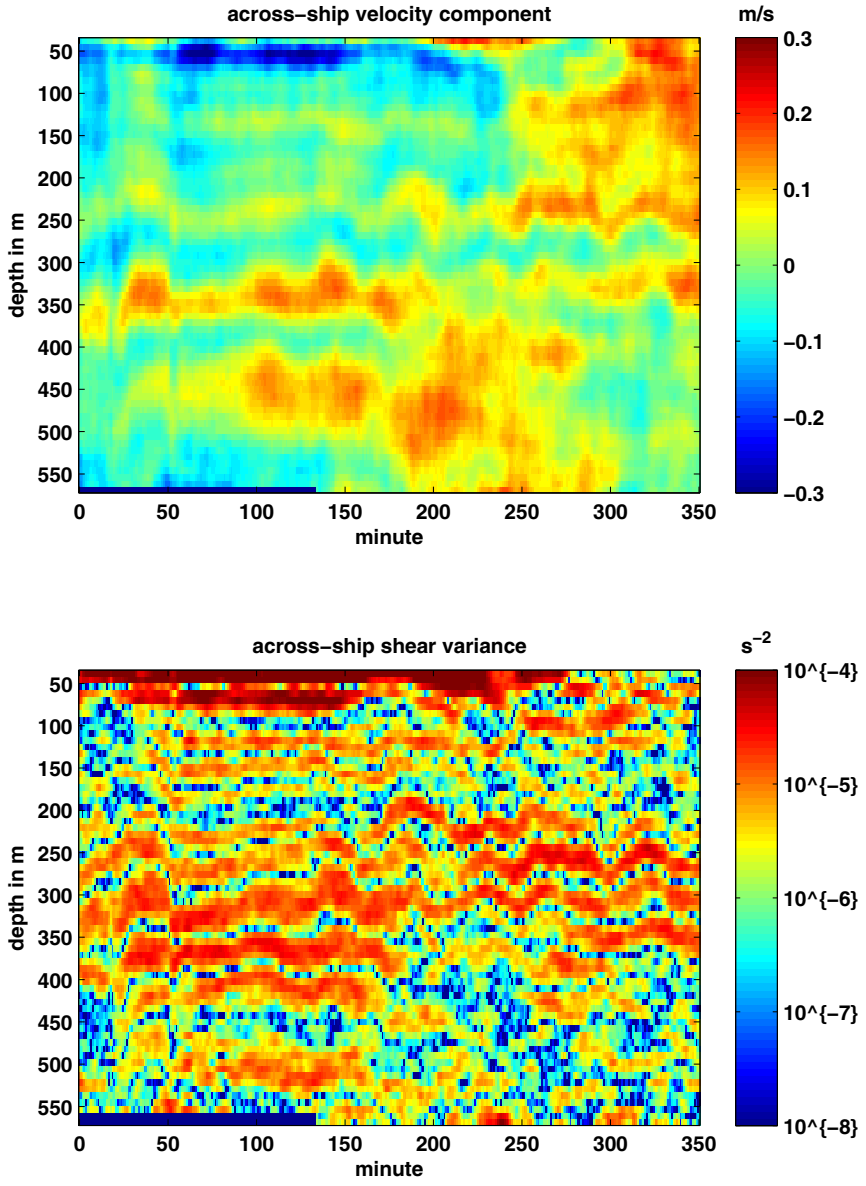

Fig. 4.16: Example of cleaned velocity and shear after processing 6 hours of BB mode data. Internal wave energy in 150 m to 500 m is about 10 times GM background level. There was a station from minute 60 to minute 130. The effect of Doppler shifting is clearly visible.

4.3 Estimate of a regional diapycnal diffusivity from microstructure

For the microscale shear measurements during both cruises, tethered microstructure profilers of type MSS90D [SeaSunTechnology, 2011] were used, equipped with two or four airfoil shear sensors. Standard profile depth was 400-500 m, with a technical depth limit of about 500-550 m. Typical microstructure stations included 3 to 5 profiles immediately before or after a CTD cast, while the vessel mounted ADCP continuously recorded data for finescale shear.

Microstructure processing comprised automated spectral fitting to the universal shear spectrum at dissipative scales to infer dissipation rate ϵ (see subsection 3.2.1 for a short description), and automated spike detection (see subsection 3.2.2). Before doing dissipation rate averages - over some depth range and/or over profiles of one station -, dissipation values below the system's detection limit were replaced by adapted substitute values (see subsection 3.2.3). System's detection limit is $\epsilon_{DL} = 2 \cdot 10^{-9}\, m^2/s^3$ corresponding to a noise level of $\epsilon_{NL} = 7 \cdot 10^{-10}\, m^2/s^3$.

When measuring microscale shear in strong stratification, notably in the sharpest part of the thermocline below the mixed layer, there's probability that MSS-estimated dissipation rates and inferred diapycnal diffusivities K will be overestimated up to a factor of 3 (section 3.3). This effect is caused by anisotropy of turbulence in strong stratification. As it is uncertain how to correct adequately for this stratification effect, dissipation rates and diffusivities will be reported uncorrected for that part of the water column. This possible overestimation has to be kept in mind when interpreting diapycnal diffusion or diapycnal fluxes in the sharp thermocline. The depth range we mainly focus on, though, is 150-500m in the main thermocline: for inferring diapycnal diffusivity and fluxes of matter here. Stratification in the main thermocline in Guinea Dome Region is of order $N^2 = 1 \cdot 10^{-5}\, rad^2/s^2$, and local isotropy of turbulence a plausible assumption here.

The microstructure measurements of the two cruises mainly serve to calibrate the vessel mounted ADCP finescale shear measurements, the latter intended to acoustically estimate dissipation rates and diapycnal diffusion. But the favourable condition that the largescale tracer release experiment GUTRE happened to take place at that same time, and in our focus depth range of 150-500m, allows the microstructure K values to be validated themselves to the GUTRE integral K estimate. For a reasonable comparison, a regional representative value of MSS derived diapycnal diffusion K has to be estimated. For that purpose stations of only a few profiles, but spatially scattered all over the region were sampled. The reason is that it can't be ruled out beforehand that longtime spatial inhomogeneities in K exist in the region.

In order to obtain a representative regional K value, arithmetic averaging of station values is chosen.

This is plausible when considering an instationary growing diffusive patch with diffusion parameter $K(t) = \frac{1}{2}\frac{d\sigma^2}{dt}$ (σ the immediate root-mean-square radius of the diffusing patch), and seeking the effective diffusion parameter K_{eff} for a longer timespan ΔT, K_{eff} describing the time-integrated effect of the instationary $K(t)$:

$$K_{eff} = \frac{1}{2}\frac{\Delta\sigma^2}{\Delta T} = \frac{1}{\Delta T}\int_{\sigma_1^2}^{\sigma_2^2}\frac{1}{2}\,d\sigma^2 = \frac{1}{\Delta T}\int_{t_1}^{t_2}\frac{1}{2}\frac{d\sigma^2}{dt}\,dt = \frac{1}{\Delta T}\int_{t_1}^{t_2} K(t)\;dt. \qquad (4.3)$$

So in a time-frame, K_{eff} may be approximated by arithmetic averaging of discrete realizations of K in time. When considering a region of inhomogeneous K, spatial arithmetic averaging is justified if the region is a unit in the sense that any water parcel will touch any location on its way in the long run, and thus experience the K inhomogeneity as a K instationarity.

Even if distributions of measured K often look similar to a lognormal distribution (and even if there might be temptation to take advantage of the lognormal assumption), the best estimate for the expectation value of a data ensemble of uncertain distribution is the arithmetic average of samples [Davis, 1996; Parkhurst, 1998], even if the uncertainty about the kind of distribution is small. And even if there'd be absolute certainty about the kind of distribution all samples origine from, the advantage of a sophisticated distribution-specific expectation estimation procedure only shows up for small sample sizes. Using a sophisticated method and being slightly erroneous about the distribution will cause greater damage than using the robust arithmetic average.

If required, bias from irregular spatial distribution of samples may be treated by area weighted averaging.

The mentioned spatial averaging relies on representative K values at each position, while measured microstructure profiles are snapshots of a highly fluctuating turbulent dissipation rate ϵ in time and depth. Assuming a depth range that may be regarded as occupied by a depth-homogeneous internal wavefield - as constant N^2 in the focus depth of 150m to 500m indicates (figure 2.6) -, assuming that the entire mixing in that depth range is caused by internal wave shear - as it appears to be in Guinea Dome Region -, and further assuming that vertical migration/fluctuation of the internal wave shear zones is happening faster than the overall intensity of the internal wave field changes:

There should exist an intermediate timescale between the fluctuation timescale of turbulent dissipation spots and the internal wave field intensity timescale, with the integral mixing effect in every depth bin equal and constant on that medium timescale. Thus the ensemble mean $\bar{\epsilon}$ may be estimated by the time mean $\langle\epsilon\rangle_t$ or the depth mean $\langle\epsilon\rangle_d$, and the depth mean may be regarded as representative for the time mean at any depth bin. That medium timescale should be about the period of the slowest fluctuating internal waves, with inertial period of $O(1\,d)$.

When averaging ϵ over the depth range of several vertical wavelengths during a 1-hour-occupation of a station, that kind of average $\langle\epsilon\rangle_{t,d}$ should also give a fair estimate of $\langle\epsilon\rangle_d$, $\langle\epsilon\rangle_t$ and $\bar{\epsilon}$. That is why $\langle\epsilon\rangle_{t,d}$ from averaging all profiles of a station over the depth range 150m to 500m serves to estimate a representative $\bar{\epsilon}$, valid for medium timescale and any depth of the depth range used. N^2 being constant in the depth range and the Osborn parametrization

$$K = \Gamma \cdot \frac{\langle\epsilon\rangle}{\langle N^2\rangle} \tag{4.4}$$

assumed valid [Osborn, 1980], the above arguments apply for $\bar{K}$ as well. As the Osborn parametrization is intended to estimate the integral diapycnal mixing effect on dissipative scales from averaged input parameters ϵ and N^2 - though the kind of averaging not clearly specified -, $\bar{K}$ should even include the effects of ϵ to N^2 correlations on shorter timescales, if existent.

Summarizing, $\bar{K}$ derived from $\langle\epsilon\rangle_{t,d}$ and $\langle N^2\rangle_{t,d}$ will be regarded as describing the integral mixing effect of internal wave shear for medium timescale of $O(1\,d)$ at a specific position for the used depth range - always keeping the assumptions in mind -; and these $\bar{K}$ may serve to estimate a regional representative $\bar{K}$ from arithmetic averaging of spatially distributed stations.

4.4 Results

4.4.1 Microstructure K estimates

Station-depth averages of diapycnal diffusion, $\langle K\rangle_{t,d}$, have been calculated from microstructure profiles at 34 stations from two cruises in November 2008 and December 2009 (figure 4.17). Given the irregular spatial sampling, a regional representative integral $\langle K\rangle$ has been estimated by area weighted averaging - a Gaussian objective mapping scheme with 0.3 degrees influence radius and 0.6 degrees cutoff radius - as $\langle K\rangle = (1.1 \cdot 10^{-5} \pm 0.4 \cdot 10^{-5})\ \frac{m^2}{s}$. There is a strong seasonal bias in that estimate of $\langle K\rangle$, though. The uncertainty of $\Delta\ \langle K\rangle = 0.4 \cdot 10^{-5}\ \frac{m^2}{s}$ is given as 95% confidence limit and was estimated from bootstrapping [Efron, 1987], with single sample errors included. The predominant contribution to $\Delta\ \langle K\rangle$ is the part contributed by sampling uncertainty that is estimated by the bootstrap resampling method.

Another integral $\langle K\rangle$ value, estimated from the GUTRE large scale tracer release experiment for just the same time, region and depth range, is $\langle K\rangle = 1.1 \cdot 10^{-5}\ \frac{m^2}{s}$ [Banyte, 2011] with uncertainty not finally determined yet.

In order to get an estimate what typical vertical profiles of dissipation rate ϵ and diapycnal diffusion K may look like (figures 4.18 and 4.19), microstructure profiles

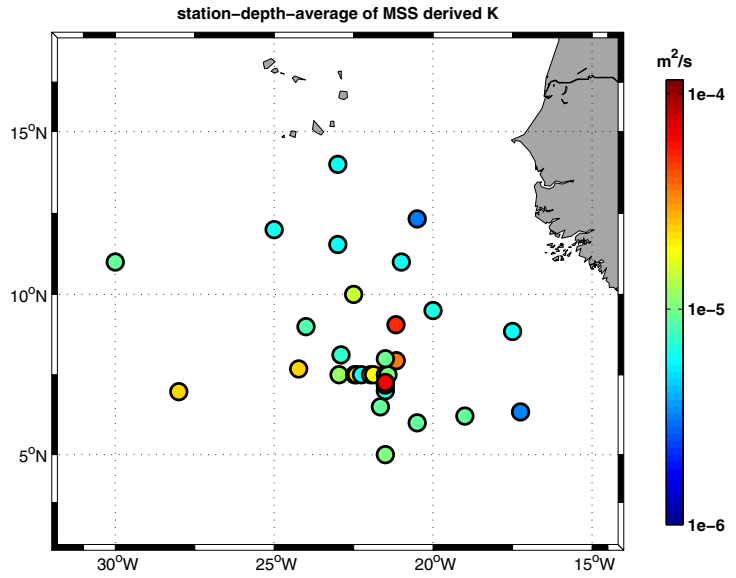

Fig. 4.17: Station-depth-averages $\langle K \rangle_{t,d}$ from microstructure derived $\langle \epsilon \rangle_{t,d}$. Area weighted average $\langle K \rangle = 1.1 \cdot 10^{-5} \pm 0.4 \cdot 10^{-5} \frac{m^2}{s}$ at depth range 150m to 500m

have been averaged in density intervals over the entire region, the density intervals then converted to intervals of scaled depth according to the average density profile (see chapter 2 figure 2.6). Depth bins are 20 m in scaled depth range below 100m, and 8 m in the sharp thermocline. For each bin and station, estimation of ϵ was done after noise substitution according to subsection 3.2.3. ϵ and K estimates in the sharp thermocline may be overestimated due to strong stratification there (cf. section 3.3).

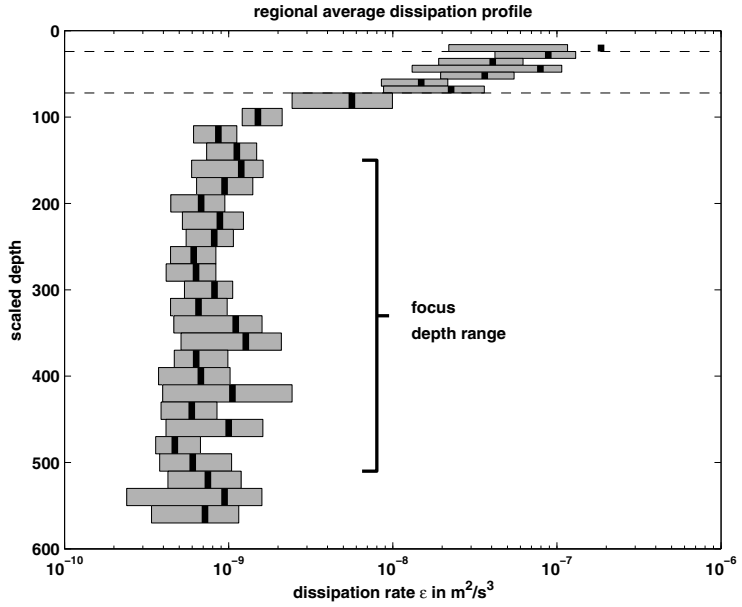

Fig. 4.18: Depthbin-wise area weighted average profile of dissipation rate in Guinea Dome Region. Scaled depth according to mean density profile as of figure 2.6. 95% confidence limits from depthbin-wise bootstrapping, single sample errors accounted for, then averaged area-weighted.

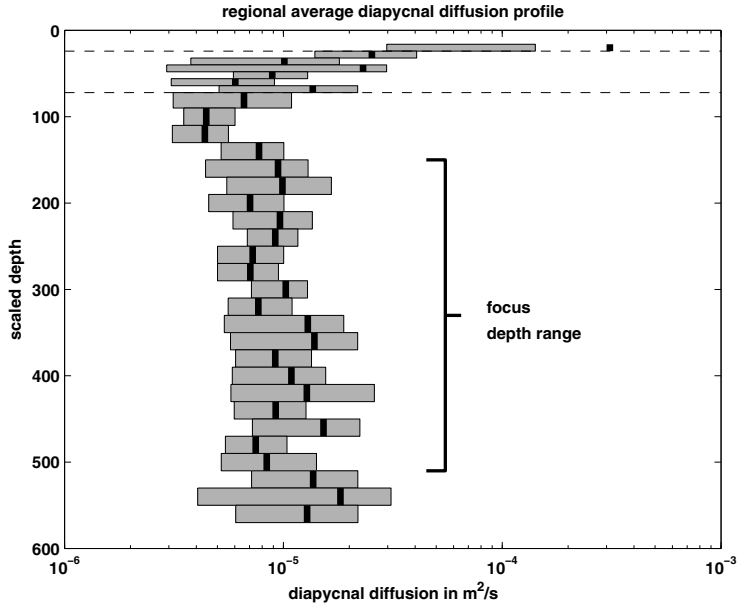

Fig. 4.19: Depthbin-wise area weighted average profile of diapycnal diffusion in Guinea Dome Region. Scaled depth according to mean density profile as of figure 2.6. 95% confidence limits from depthbin-wise bootstrapping, single sample errors accounted for, then averaged area-weighted. For comparison: area weighted average $\langle K \rangle = 1.0 \cdot 10^{-5} \pm 0.5 \cdot 10^{-5} \, \frac{m^2}{s}$ at depth range 150m to 500m

4.4.2 Relation of finescale shear and microscale shear

Station-depth averages of microstructure dissipation rates, to be used as representatives of microscale shear variance or $\bar{\epsilon}$, have been obtained and serve as calibration base for vmADCP derived finescale shear variance. The latter is obtained from vertical shear spectra as a depth average value already by method, so that time-averaging of shear spectral levels Φ_S for the duration of one shipstation, $\langle \Phi_S \rangle_t$, delivers corresponding ADCP finescale shear variance just for the same time and depth range as the microstructure calibration data. These $\langle \Phi_S \rangle_t$ may analogously be regarded as representative for the medium timescale of $O(1\,d)$ and any depth bin (cf. section 4.3). Calibration by MSS can necessarily only be done at times when the ship is not (or hardly) moving. So the fact that vmADCP derived Φ_S does not systematically differ with ship speed (subsection 4.2.6 and figure 4.11) is of vital importance for this here attempt to parametrize $\bar{\epsilon}$ for the entire vmADCP datasets.

Two main physical influences are identified that act on the internal wave field's probability to produce turbulence: the internal wave shear spectral level Φ_S as a measure of finescale shear energy provided, and the wave crest slope $tan\,\alpha$ as a measure of the waves' liability to get steepened, become instable and break. For the purpose of parametrization $\bar{\epsilon} = f_{param}\,(\Psi_1, \Psi_2)$, we use influence factors Ψ_1 and Ψ_2 that are proportional to Φ_S and $tan\,\alpha$:

$$\Psi_1 = N^2 \cdot G \propto \Phi_S \tag{4.5}$$

with $G = \Phi_S / \Phi_{S,GM}$. Relation 4.5 is based on the scaling of Φ_S with N^2 in the limit of large vertical wavenumbers (equation A.13) and on the characterization of internal wave fields with energy above E_{GM} by $E = G \cdot E_{GM}$.

$$\Psi_2 = \frac{f}{N} \propto tan\,\alpha \tag{4.6}$$

is derived in appendix A (equation A.23). The adequacy of both parameters to really describe the physical influences as intended, depends slightly on the validity of the GM internal wave model. Φ_S is measured spectrally in a limited vertical wavenumber band and requires the assumed flatness of spectral shape in order to be a valid estimator for the entire amount of finescale shear energy in the internal wave field. The proportionality $tan\,\alpha \propto f/N$ directly depends on the GM model inherent distribution of wave energy on space- and timescales. Nonetheless we suppress the temptation of including a third parameter that could describe deviations from the GM internal wave field, because a) in the open ocean the GM model seems to be a good approximation of the internal wave energy distribution after its early iterative adaption to open ocean internal wave measurements in the 1970s, and b) parameters that could be chosen are extraordinarily tedious to measure precisely compared to f, N and G; thus there is concern of practically introducing more noise

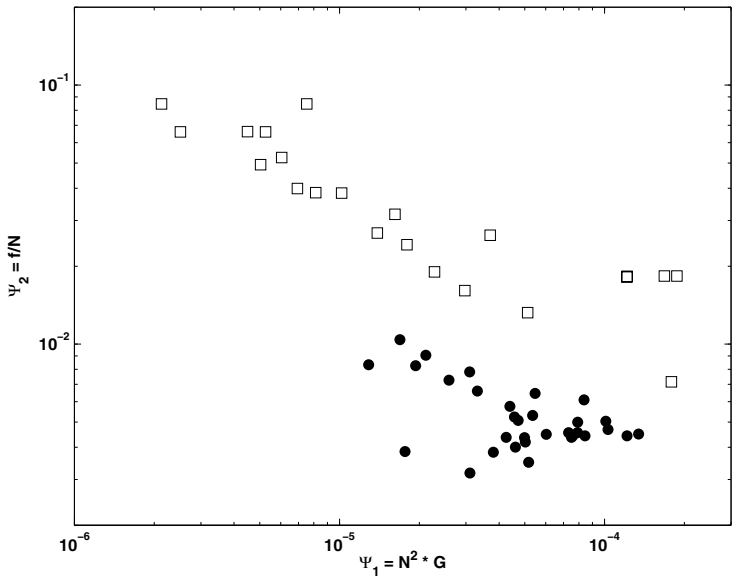

Fig. 4.20: Occupied parameter space (Ψ_1 , Ψ_2) of available data: measurements reported by [Polzin et al., 1995] (squares) and our measurements (dots).

to the parametrization than taking benefit from such an additional parameter. E.g. average frequency content $\langle\omega\rangle / f$ or shear-strain-ratio R_ω as have been used by [Polzin et al., 1995] need longterm stations for their determination and are known for their high uncertainty.

So keeping to relatively simple input parameters (f from navigation, N from occasional CTD casts, Φ_S or G from underway ADCP) intends a broad practical utility of the parametrization that is seeked here.

f and N are badly conditioned for our data that have exclusively been measured in Guinea Dome Region. Range of f is a factor of 3, range of N^2 is a factor of 2 only. This puts high risk to a parametrization to be only valid inside the narrow parameter limits and deviate intolerably from just outside the limits. In order to render more physical meaning and reliability to the functional relation we seek, we enhance the parameter space coverage by including data reported by [Polzin et al., 1995] (figure 4.20). These were obtained - dissipation rates as well as finescale shear for depths down to 3000m - with the Woods Hole HRP profiler [Schmitt et al., 1988] from 73 profiles during three large experiments in the Eastern North Pacific and the Western and Eastern North Atlantic.

For parametrization we use the simple approach of separable variables

$$\bar{\epsilon}_{param} = c_0 \cdot \Psi_1^{c_1} \cdot \Psi_2^{c_2}, \tag{4.7}$$

but do optimum parameter search in log-space

$$log\,\bar{\epsilon}_{param} = c_0 + c_1 \cdot log\,\Psi_1 + c_2 \cdot log\,\Psi_2. \tag{4.8}$$

There are two main remarks for the optimum search here: i) we are not using linear regression but the criterion that residuals $log\,\bar{\epsilon}_{measured} - log\,\bar{\epsilon}_{param}$ not be correlated to $log\,\bar{\epsilon}_{param}$. Using linear regression would assume error-free input parameters and all scattering just caused by $\bar{\epsilon}_{measured}$, which is clearly not the case. Particularly G from underway ADCP is laden with an error of similar magnitude as $\bar{\epsilon}_{measured}$. Under these circumstances linear regression delivers slopes too low. ii) the optimum parametrization should not only meet the criterion that the points ($log\,\bar{\epsilon}_{measured}$, $log\,\bar{\epsilon}_{param}$) lie on a straight line of slope 1, but so should its "inversions". That is, the optimum parametrization should also show a straight line of slope 1 when points ($log\,\bar{\epsilon}_{measured}/\Psi_i^{c_i}$, $log\,\bar{\epsilon}_{param}/\Psi_i^{c_i}$) are plotted. In our case e.g. (c_0, c_1, c_2) should be the optimum coefficient choice for $\bar{\epsilon}_{measured}/\Psi_1^{c_1} = [c_0\,\Psi_2^{c_2}]^1$ as well. This seems a natural consequence of a good parametrization fit for points ($\bar{\epsilon}_{measured}$, $\bar{\epsilon}_{param}$), but is not. Badly conditioned parameters, say very narrow in bandwidth compared to other parameters, may be equipped with a suboptimal exponent choice, but be camouflaged by the wide range parameters' fitting quality in the main parametrization. Inversions reveal both bad conditioning and bad exponent choice.

For the unified dataset,

$$\bar{\epsilon}_{param} = \frac{3}{19} \cdot \Psi_1^{1.5}\,\Psi_2^{0.8} \tag{4.9}$$

meets the optimum criteria, that means

$$\bar{\epsilon}_{param} = \frac{3}{19} \cdot f^{0.8}\,N^{2.2}\,G^{1.5} \tag{4.10}$$

with parameters translated (figure 4.21). 95% confidence limits for exponents from bootstrapping are coincidentally 0.22 for all three. Equation 4.10 is also the optimum choice when doing optimum search on three parameters (f, N, G) as

$$log\,\bar{\epsilon} = d_0 + d_1 \cdot log\,f + d_2 \cdot log\,N + d_3 \cdot log\,G. \tag{4.11}$$

Figure 4.22, showing the inversions of equation 4.10, illustrates the bad conditioning of the GDR dataset in f and N on the one hand and of the [Polzin et al., 1995] dataset in f on the other hand. The unified dataset does much better as already indicated by the better coverage of parameter space (figure 4.20), although f is still the weakest parameter. Concluding f from $\bar{\epsilon}_{measured}$, N and G by reversed parametrization would certainly give bad results - strange idea that it might be anyway.

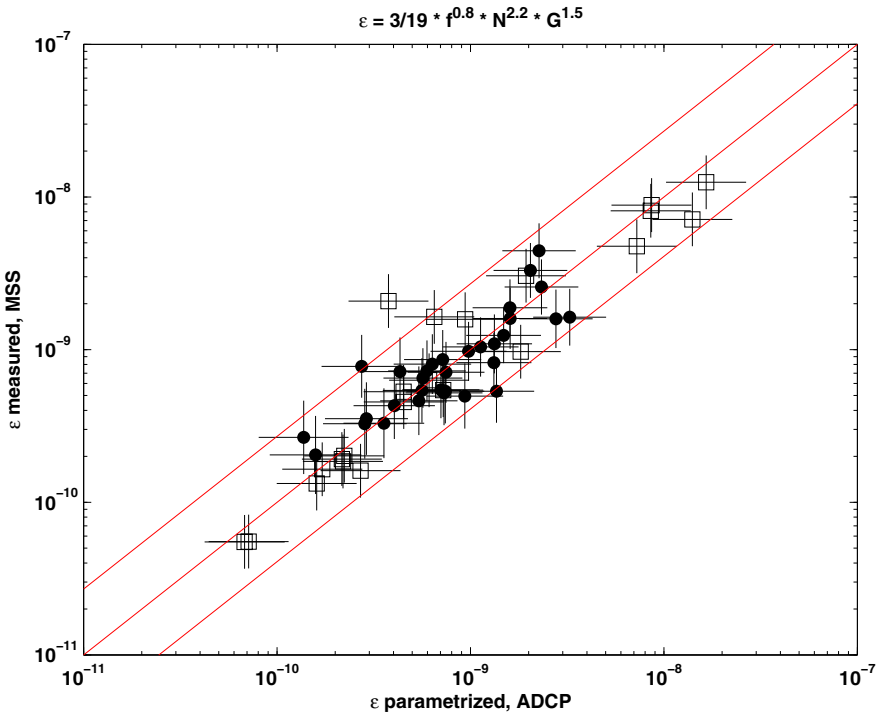

Fig. 4.21: Optimum parametrizational fit for the unified dataset of data reported by [Polzin et al., 1995] (squares) and data from GDR (dots). Individual error bars are 95% level. 95% confidence limits of the fit ara a factor of 2.7 (red lines).

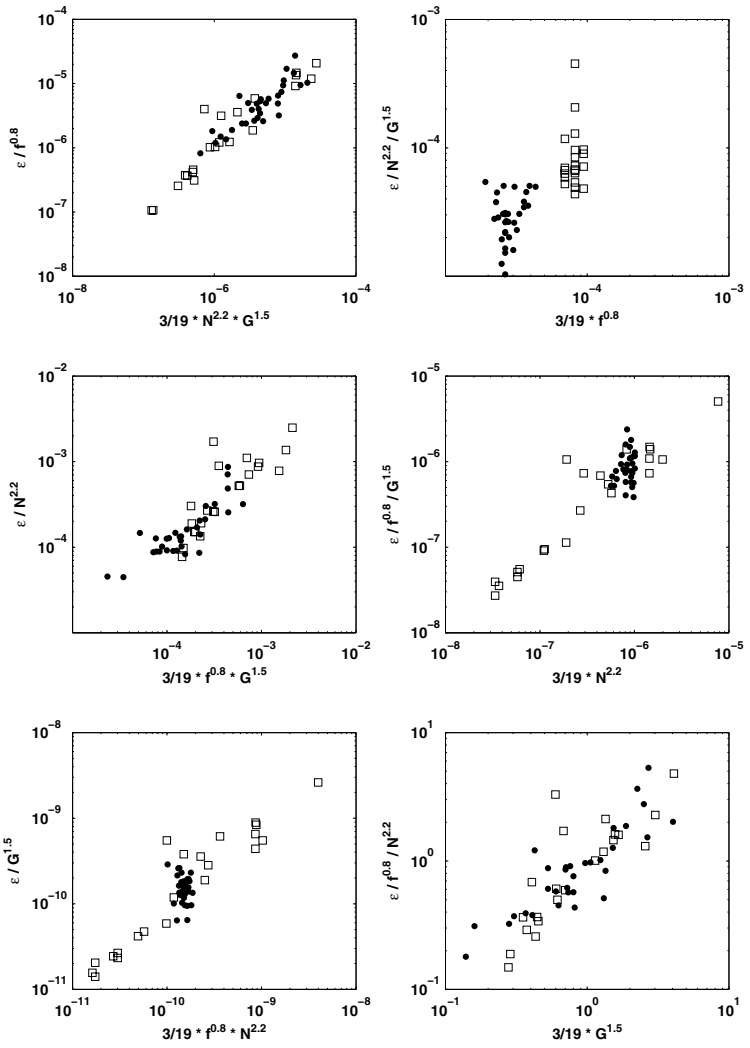

Fig. 4.22: "Inversions" of the optimum parametrizational fit of figure 4.21. Data reported by [Polzin et al., 1995] (squares) and data from GDR (dots).

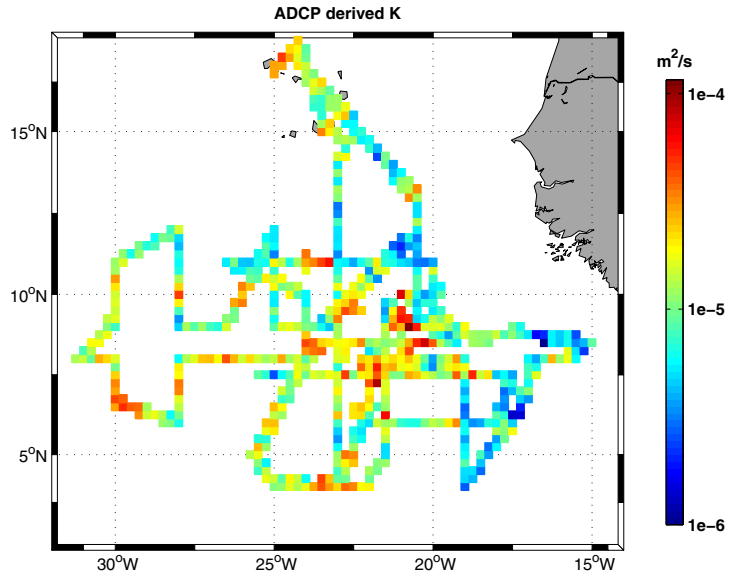

Fig. 4.23: Diapycnal diffusivity $\bar{K}$ values derived from ADCP estimated shear levels. Merged data from two cruises. Area weighted average $\langle K \rangle = (1.2 \cdot 10^{-5} \pm 0.2 \cdot 10^{-5}) \frac{m^2}{s}$

4.4.3 Spatial distribution of ADCP derived diapycnal diffusion

By aid of the parametrization (4.10) and the Osborn parametrization (3.6), underway-ADCP-based $\bar{K}$ is estimated, and condensed by averaging on $1/4° \times 1/4°$ boxes (figure 4.23). This dataset of $\bar{K}$ may be regarded as an ADCP based extension of the MSS station $\bar{K}$ values of subsection 4.4.1, so it is expected to improve the regional $\langle K \rangle$ estimate and reduce the associated bootstrap-based error estimate:

$$\langle K \rangle = \left(1.2 \cdot 10^{-5} \pm 0.2 \cdot 10^{-5}\right) \frac{m^2}{s} \tag{4.12}$$

after area weighted averaging with the same Gaussian objective mapping scheme as used in subsection 4.4.1 with 0.3 degrees influence radius and 0.6 degrees cutoff radius.

This $\bar{K}$ dataset is just a snapshot patchwork of two cruises, but useful besides its ameliorating the integral $\bar{K}$ estimate for Guinea Dome Region. Two prominent features do emerge from figure 4.23: On medium scales $O(10\,km)$ to $O(100\,km)$ coherent $\bar{K}$ structures exist of many hours duration and up to 100 km. On the larger scale $O(300\,km)$ regions of scattered but systematically higher and lower $\bar{K}$ exist that form patterns suggesting some relation to bottom topography; like the seamountain range at $10°\,N$ to $6°\,N$ and $24°\,W$ to $20°\,W$ or the abyssal plains North and East of it (cf. figure 2.1 or 4.26).

First look into the nature of the medium scale coherent structures in $\bar{K}$, that is, look at patches of elevated $\bar{K}$ and what may be learned about them from vmADCP data. From visual inspection of velocity and shear data (not shown) it becomes clear that these are coherent shear structures indeed, presumably internal waves all of them. Two illustrating examples are given: figure 4.16 of a wave train of 6 hours duration and at least 50 km extent, and figure 4.25 of a distinct wave group that will be described in more detail in a moment.

For a selection of patches of elevated $\bar{K}$ (figure 4.24), a table of parameters deducible from vmADCP measurements is given (table 4.1). In general the acoustic data from vmADCP are not sufficient to completely unravel the observed internal waves' characteristics. Dominant vertical wavenumbers in the used wavenumber band 128 m to 38 m, and shear spectral level Φ_S - or its relative counterpart G - may be obtained from the across-ship velocity component when the ship is moving. At stations, the two velocity components available can often give additional information on vertical orientation of group velocity from rotary spectra [Gonella, 1972; Leaman and Sanford, 1975], as well as on a possible horizontal directional preference of wave propagation. But with few exceptions station occupation on research cruises will be too short to allow wave frequencies to be estimated in a satisfactory manner. Thus estimates of further internal wave parameters such as horizontal wavenumber or magnitudes of phase and group velocity are usually impossible.

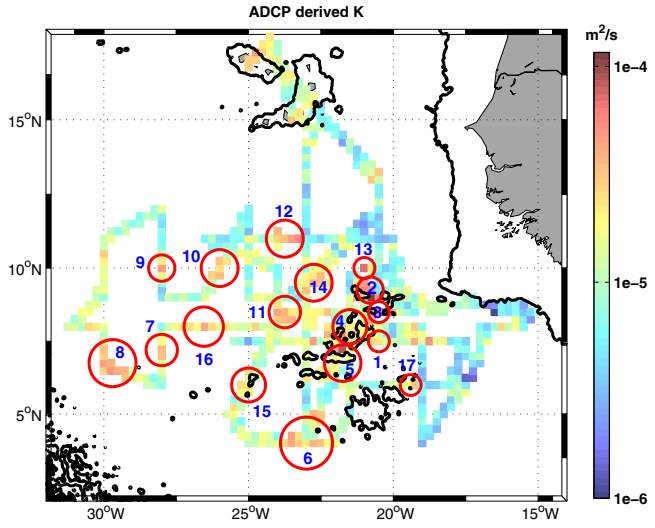

Fig. 4.24: Selection of patches of elevated $\bar{K}$ for further analysis. Numbers correspond to table 4.1. Bold black contours are 3000 m isobath.

feature	**topography**	**G**	c_{gr} **dir.**	$\frac{G_{zonal}}{G_{merid.}}$	**char.** λ_v	ω	λ_h
1	Y	2.5	up	2	80 m		
2	Y	7	down	1			
3	Y	9	down	1			
4	Y	6	down	1	100 m		
5	Y	11	down	1	100 m		
6	N	6	down	0.2	55 m	30 f	900m
7	N	10.5	up	1	100 m		
8	N	7	down	1			
9	N	5	down	1			
10	N	3	down	1	90 m		
11	(Y)	4	equal	3	100 m		
12	N	3	down	2			
13	(Y)	8	down	1			
14	N	5	down	1			
15	Y	5	down	1	100 m		
16	N	3.5	equal	0.4			
17	Y	4	up	2	70 m		

Table 4.1: Some deducible characteristics of selected patches of elevated $\bar{K}$. Topography influence rated based on topography parameter To. Characteristic vertical wavelength λ_v, G_{zonal}, $G_{meridional}$, G from vertical shear spectra, direction of group velocity from rotary shear spectra. The wave group feature 6 was recorded at a 4 hour station thus allowing an estimate of frequency and horizontal wavelength λ_h.

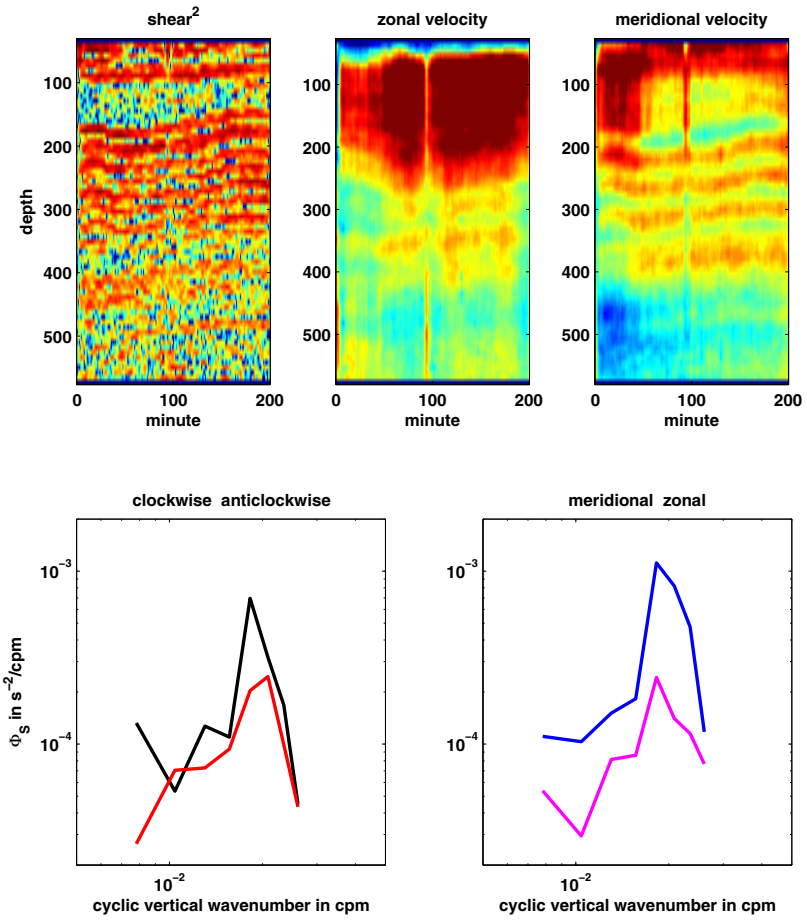

Fig. 4.25: Example of a 6 hour period, meridionally propagating wave group with group velocity down (feature 6 in table 4.1). Clockwise spectrum black, counterclockwise spectrum red. Meridional component spectrum blue, Zonal component spectrum magenta.

One of the few exceptions is a strong internal wave group met on cruise M80/2 at a 4 hour station at $4° N$ $23° W$ (figure 4.25) whose origin will be discussed in section 4.5. Station occupation at that position was long enough to estimate the half period to be 2.5 to 3 hours which is equivalent to a frequency of roughly 30 times the local Coriolis parameter f. There's a strong directional preference towards meridional propagation that can also be deduced from the vertical shear spectra of the velocity components at the dominant vertical wavenumber of about 50 m. At that wavenumber clockwise rotation of velocity components dominates, corresponding to a downward group velocity. The vertical group velocity component of about 2 mm/s means that the wave group may have left the mixed layer depth about one day before. Finally the velocity components show a zone of strong shear of about $2 \cdot 10^{-2}\, s^{-1}$ between a NNW current at 40 m and presumably further up, and an Eastward jetlike current from about 60 m down to 200 m.

Common to all of the tabulated high $\bar{K}$ patches is coherence of internal wave shear patterns on medium scales of $O(10\,km)$ to $O(100\,km)$. There are waves of upward energy transport indicating generation by tidal interaction with bottom topography. There seem to be many near inertial waves of downward energy transport indicating wind generation. And there is at least one clear example of a strong internal wave group not complying to these two type characteristics (feature 6, figure 4.25). The vmADCP-method-inherent incompleteness of data unfortunately forbids further quantitative analysis of regional internal wave processes and their contribution to turbulent mixing.

To go on in a more heuristic manner, focus on the larger scale regional patterns of order $O(300\,km)$ in $\bar{K}$ and their anticipated potential determination by topographic influence. This regional scale approach might even be the more appropriate one to detect topographic influence in particular, because the expected internal tide wave groups that are produced at the bottom and propagate upwards are characterized by remote sources, directional anisotropy and temporal and spatial incoherence (on larger scales than the medium scales considered before) [Ray, 2001]. Horizontal distances between the location of generation and the location where actual internal tidal wave groups are detected in the main thermocline may be of order $O(100\,km)$. So averaging should comply greater distances than that.

Before partitioning Guinea Dome Region into smaller regions, get a quantitative measure for the potential of bottom topography to mediate the generation of internal tides. We follow [Jayne and StLaurent, 2001] who multiply a characteristic horizontal wavenumber of bottom elevation, k, to the variance of bottom elevation, h^2, to get a bottom roughness parameter. This seems plausible as areas with highly variable elevations at small distances, meaning high $k \cdot h^2$, should display a wide range of bottom slopes that renders tidal interaction with the bottom at critical angles more probable. $k \cdot h^2$ is calculated from the global bathymetry compilation ETOPO1 in 1 nm resolution [Amante and Eakins, 2009], doing running boxcars of $64 \times 64\,nm$ to allow relation of internal waves to their possible $O(100\,km)$ remote topographic sources. Led by prejudice, influence of bottom topography should also increase with decreasing water depth. Thus a heuristically obtained combination of bottom roughness $k \cdot h^2$ and depth D is chosen, baptized dimensionless topography parameter To, that best fits internal wave shear spectral level $\Phi_S \propto N^2\,G$ at the longterm microstructure stations (figure 4.26). To is scaled in order to occupy a convenient range of low numbers:

$$To = \sqrt[4]{\frac{k \cdot h^2}{D^{1.5}} \cdot 2 \cdot 10^7\, m^{0.5}}. \tag{4.13}$$

with the rather uncommon coefficient dimension 'meters square root' in order to secure dimensional match. The functional relation and the regional variation of To is highly dependent on the ETOPO1 bathymetry.

Figure 4.27 overlays records of internal wave shear activity for both cruises with

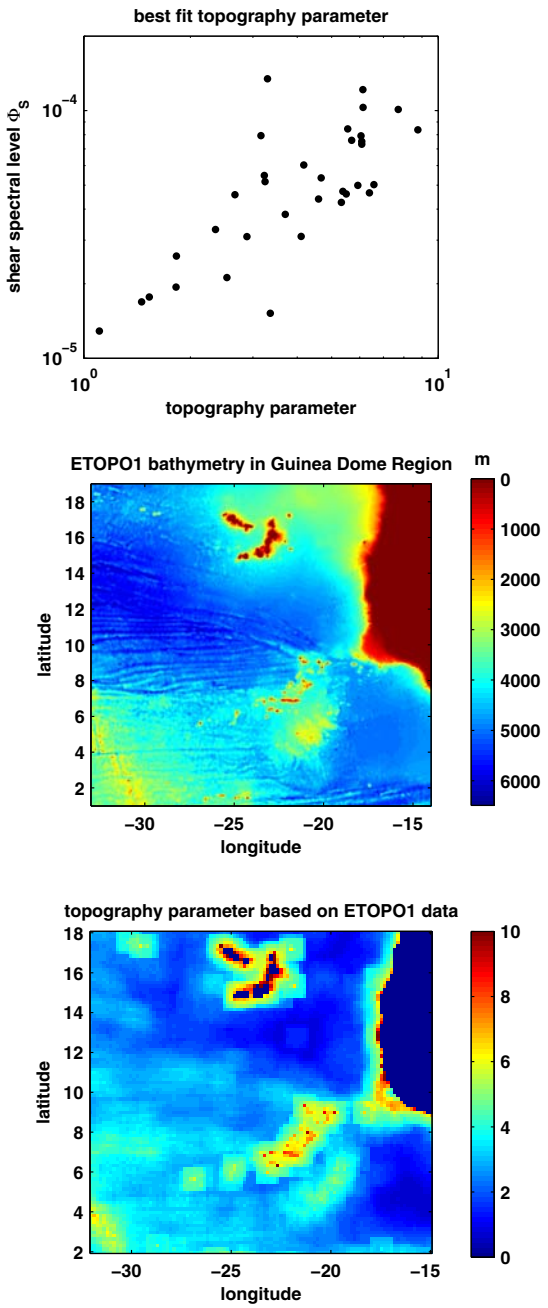

Fig. 4.26: Visualizing dimensionless topography parameter To (equation 4.13). Upper panel: correlation to shear spectral level at MSS stations. Middle: ETOPO1 bathymetry for comparison. Lower panel: To map.

corresponding topography parameter To. While elevated To over seamountains - mainly at the central seamountain range - do correspond in many cases to internal wave shear peaks, and low To of abyssal plains do in most cases correspond to low internal wave shear, there seems to be no relation at the Cape Verdian rise and the Guinean continental slope. Moreover, there are many internal wave shear peaks without corresponding topography indication to be found mainly West of the central seamountain range. The overall predictive power of To is low, the humble explained variance $r^2 = 20\%$ mostly merited to seamountains and abyssal plains. Thus direct quantitative employment of To to categorize regions by topography is abandoned; but the different characterizations of topography types that have emerged from the synopsis of To and internal wave shear will be used: a) abyssal plains characterized by low $To \leq 3$ and low shear, b) seamountain influence characterized by high To and frequent episodes of high shear, c) continental slopes and rises characterized by low shear in spite of a promising To and d) the inhomogeneous and hard-to-define Western region characterized by frequent episodes of high shear in spite of not particularly elevated To.

These four topographic half-empirically defined phenotypes lead to a partitioning of Guinea Dome Region according to figure 4.28. The partitions' average diapycnal diffusivities are $\langle K \rangle_{A_1} = 1.1 \cdot 10^{-5} \frac{m^2}{s}$ and $\langle K \rangle_{A_2} = 0.8 \cdot 10^{-5} \frac{m^2}{s}$ for the Northern and Eastern abyssal plain, respectively, and a uniform $\langle K \rangle_B = \langle K \rangle_C = \langle K \rangle_D = 1.5 \cdot 10^{-5} \frac{m^2}{s}$ for the other three formations.

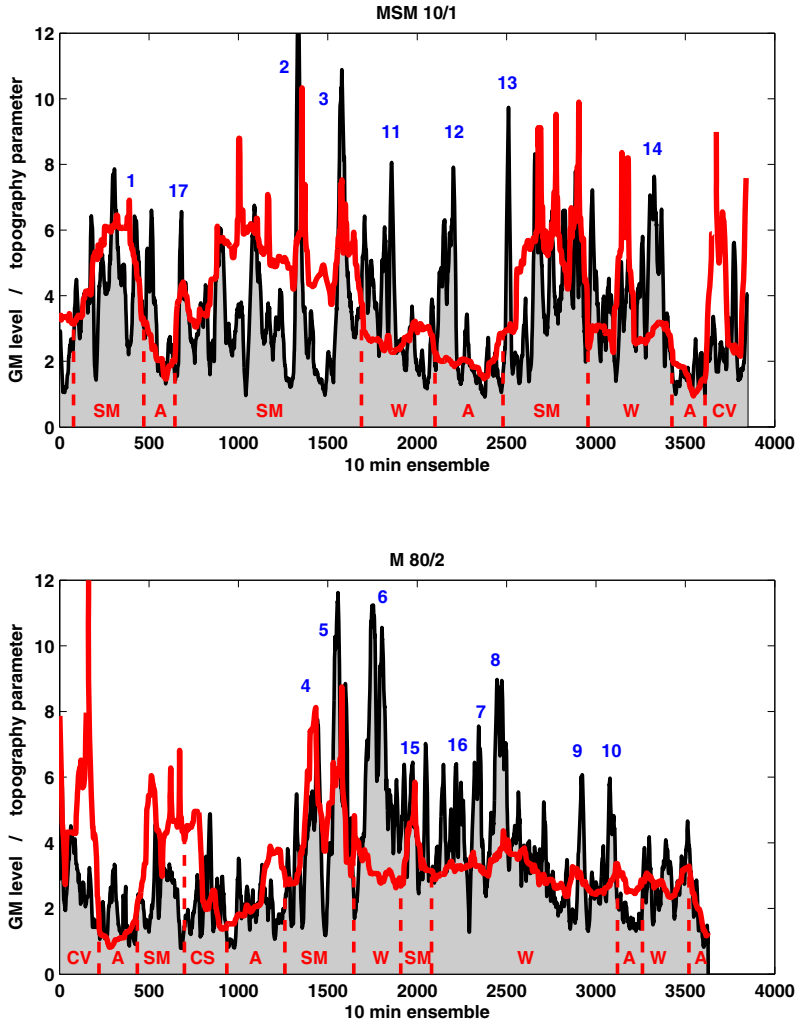

Fig. 4.27: Measured relative shear spectral levels G (black lines) and corresponding topography parameter To (red lines) for both cruises. Visually rated bathymetry features marked as seamountain (SM), abyssal plain (A), Cape Verdian rise (CV), continental slope of Guinea (CS) and region West of seamountain range (W). Blue numbers correspond to numbers of elevated $\bar{K}$ patches of table 4.1 and figure 4.24.

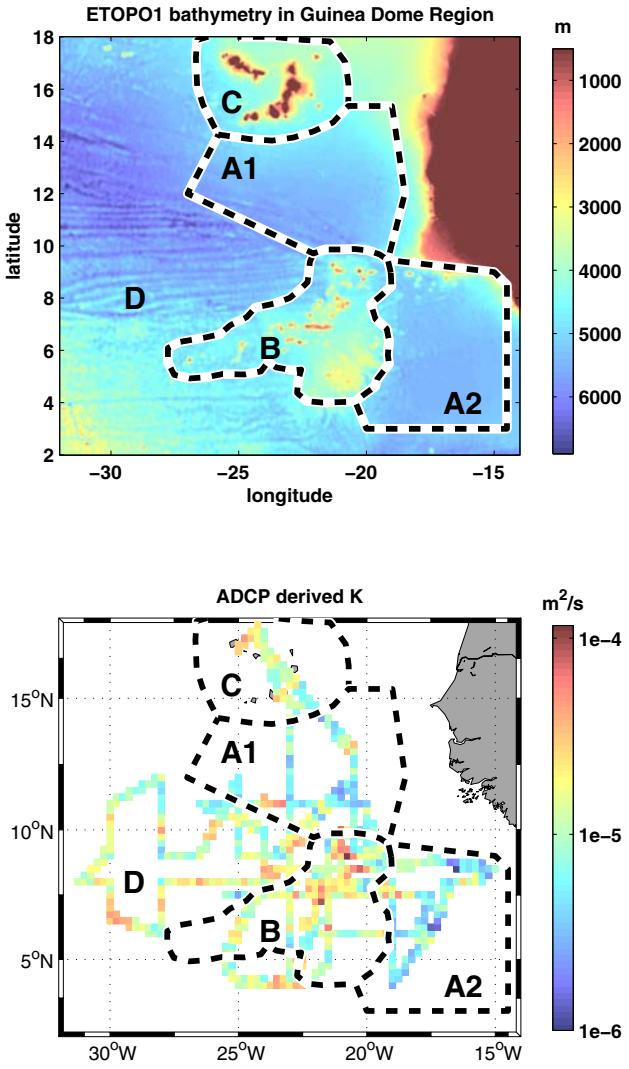

Fig. 4.28: Partition of Guinea Dome Region (plus Cape Verdian archipelago) based on common common characteristics. A_1, A_2 abyssal plains, B seamountain range, C Cape Verdian surroundings, D Western region neither fitting A nor B.

4.5 Discussion

Observation of shear structures and quantifying shear variance from underway ADCP

Most acoustic data used here is from high precision broadband (BB) mode of vessel mounted Ocean Surveyor ADCP. Calculated shear spectral levels Φ_S as a measure of shear variance are consistent with expectations: in that there is no visible systematic difference in Φ_S whether the ship is moving or not (figure 4.11), in that the recorded Φ_S occasionally occupy background internal wave level $\Phi_S = \Phi_{S,GM}$ or $G = 1$ as the minimum value, and in that filtered and corrected velocities display roughly flat vertical shear spectra in the wavenumber band $(128\,m)^{-1}$ to $(38\,m)^{-1}$ for internal wave energy levels of 1 to 10 times the Garrett-Munk (GM) value (figure 4.12). The simplest explanation for these properties is credibility within error limits and practical utility of the processing method laid down in section 4.2.

A veritable limitation might be cases of stronger shear than 10 times GM ($G = 10$), as the used wavenumber band would not allow differentiating spectra of higher energy, given the canonical shear spectrum is true (compare figure 4.4 in subsection 4.2.1). Events $G > 10$ have been sometimes recorded though in the run of the two cruises, and there is no reason to suspect $G > 10$ to play a major role here (compare subsection 4.2.6): Neither do we know of common occurrence of $G > 10$ in the open ocean main thermocline, nor is there a discrepancy in our estimated $\langle K \rangle$ from shear data to expected values, which could have suggested our ignorance of rare giant mixing events.

We have few processed data from the long range, less precise narrowband (NB) mode of the Ocean Surveyor vmADCP, but there is no indication that processing would not lead to satisfactory results; neither from expected error margins, nor from deduced spectra and shear spectral densities (figure 4.13). For a final evaluation of shear data quality from NB mode, more exhaustive datasets have to be checked. The NB mode question is an important one, as most German collected Ocean Surveyor data of the last decade are NB mode.

In the typical research cruise frame, accurately processed vessel mounted ADCP measurements do prove useful in not costing extra ship-time, be it underway or during station's work. When underway, useable data is confined to the across-ship velocity component and mainly energy/shear spectral level of shear structures may be deduced. Visual inspection of velocity and shear sections may give hints on structures' horizontal scales. At station, both velocity components are useable, thus allowing slightly more precise shear level estimates, and often getting information on group velocity direction and horizontal directionality of particular wave groups. Sometimes information on frequency may be obtained. In order to calibrate ADCP finescale shear to microstructure shear and dissipation, occasional station work is eesential. Major limitations of the vmADCP method are the ADCP performance

limits in the range/resolution trade-off (that at the moment confine estimates of shear to the upper 500m), and the method-inherent confinement to only that part of diapycnal mixing to be estimated that is caused by vertical shear instability/internal wave breaking.

Microstructure shear measurements

Dissipation ϵ and diapycnal diffusivity K profiles (figures 4.18 and 4.19), deduced from microstructure shear and averaged over Guinea Dome Region, are assumed to represent qualitatively correct the profile shape on medium timescale of $O(1\,d)$ at any station. They are more or less constant from 150m to 500m, our focus depth; the scatter being ascribed to the rather low number of 34 stations taking part in the average. This constancy on medium timescale is plausible for any station, as stratifcation being about constant in that depth range for any station is found, as should be expected from a constant vertical diffusion coefficient. Further there is no indication of vertical inhomogeneity in the internal wave field for this depth range, so that intermittent short smallscale mixing events resulting from internal wave shear should in the longer run regularly fill the whole depth range and equal out.

There may be a slight, while insignificant, tendency of ϵ to decrease and K to increase with depth. Such tendencies correspond to typical findings at other open ocean places [Gregg and Sanford, 1988; Ferrari and Polzin, 2005]. A kind of bottleneck in K seems to exist at the lower end of the sharpest thermocline, and keeping in mind the possible overestimation of K in strong stratification of up to a factor of 3 (section 3.3), that bottleneck might in reality continue through the sharpest thermocline until just below the mixed layer.

The Guinea Dome region average $\langle K \rangle = 1.1 \cdot 10^{-5} \frac{m^2}{s}$ after area weighting is intended to approximately represent the regional integral $\langle K \rangle$ for the main thermocline. This value is supported by estimates of the regional integral $\langle K \rangle$ from the large scale tracer experiment GUTRE. That coincidence may be seen as a confirmation of prior assumptions: that microstructure measurement procedures implemented do work satisfactory, that microscale turbulent shear is the predominant cause of mixing in the GDR main thermocline, and that the available set of spatially scattered stations is sufficient to estimate a regional $\langle K \rangle$ here. Nonetheless a seasonal bias is present as both cruises happened to be in early boreal winter.

Parametrization of dissipation rate

The current state-of-the-art finescale shear to microscale shear parametrization - in "its latest incarnation" as [Kunze et al., 2006] put it - in its core goes back to a fit to early ray tracing simulations [Henyey et al., 1986] and was stepwise adapted to results of several field campaigns [Polzin et al., 1995; Gregg et al., 2003]. It is

a function of four parameters: the Coriolis parameter f, the buoyancy frequency N, the relative shear spectral level scaled to the Garrett-Munk model value $G = E/E_{GM}$, and the shear-to-strain ration R_ω as a measure of frequency content or deviation from GM well-behaviour. The functional form is equivalent to

$$\epsilon = 6.73 \cdot 10^{-10} \frac{m^2}{s^3} \cdot \frac{N^2}{N_0^2} G^2 \frac{R_\omega + 1}{R_\omega \sqrt{R_\omega - 1}} \frac{\sqrt{2}}{\frac{4}{3}} \frac{f \, arcosh \frac{N}{f}}{f_{30^\circ} \, arcosh \frac{N_0}{f_{30^\circ}}} \tag{4.14}$$

with $N_0 = 5.24 \cdot 10^{-3} \frac{rad}{s}$ and f_{30° the coriolis parameter at 30° latitude. Or, with use of the Osborn parametrization (3.6),

$$K = \frac{1}{14} m^2 \cdot G^2 \frac{R_\omega + 1}{R_\omega \sqrt{R_\omega - 1}} f \, arcosh \frac{N}{f} \tag{4.15}$$

with m^2 square meters, not vertical wavenumber squared. This formulation differs from our choice of parametrization, most prominently in the G dependence (see subsection 4.4.2):

$$\epsilon = \frac{3}{19} m^2 \cdot \Psi_1^{1.5} \, \Psi_2^{0.8} = \frac{3}{19} m^2 \cdot f^{0.8} \, N^{2.2} \, G^{1.5}. \tag{4.16}$$

Equation 4.16 originates from a fit of a unified dataset (diverse field campaign data from midlatitudes published by [Polzin et al., 1995] plus our field data from Guinea Dome Region, figure 4.29) to two influence parameters. This choice of only two influence parameters is based on physical reasoning, Ψ_1 being proportional to shear spectral level as a measure of shear energy present, and Ψ_2 being proportional to internal waves' crest slope as a measure of vulnerability to breaking. And it is guided by apparent unnecessary inclusion of a third parameter accounting for the internal wave field's deviation from the GM model, as far as the unified dataset can tell (figures 4.21 and 4.22). The only obvious outlier is a value from close to the flank of a seamountain - $F\,3$ in [Polzin et al., 1995]'s nomenclature. But such a setting should play no part in our attempts to infer main thermocline ϵ.

Introducing an additional parameter for GM deviation, as R_ω for example, would also mean the need to get good estimates of wave frequencies or vertical strain rates. Such require rather longtime stations and are known for high scatter. Thus - not excluding the possibility that R_ω could lead to a somewhat better fit - for practical reasons we stick to the more simple parametrization (4.16) that just requires underway ADCP data plus an information on stratification from occasional CTD stations. The satisfactory fit to measurements under our simple two-parameter-approach - that to some extent relies on the GM model and omits inclusion of a GM deviation parameter - also confirms the impression that in open ocean settings GM is a quite appropriate internal wave model.

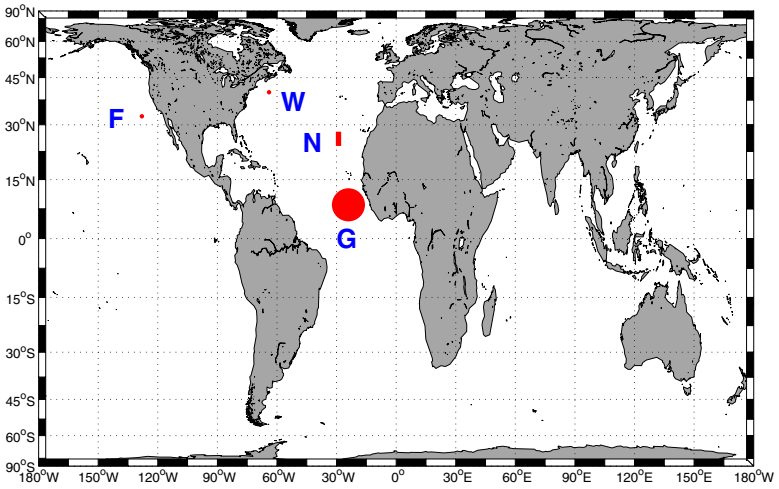

Fig. 4.29: Regions that contribute to the unified dataset of combined finescale shear and microstructure measurements. G: Guinea Dome Region of Nov. 2008 and Dec. 2009. [Polzin et al., 1995]'s reported data: F: Fieberling Guyot seamount of Mar. 1991; W: Gulf Stream warm core ring of Mar./APr. 1990; N: NATRE open ocean site of Apr. 1992.

Notwithstanding the notion that inclusion of a GM deviation parameter should be physically reasonable when leaving the open ocean environment, there is some indication that [Polzin et al., 1995]'s inclusion of R_ω might be an overfit (see figure 4.30). Their collected dataset shows correlation between $G = E/E_{GM}$ and the GM deviation cluster $(R_\omega + 1)/R_\omega/\sqrt{R_\omega - 1}$, so that a whole family of equally fine parametrizational fits can be sustained, each with a different exponent in G.

The chosen parametrization (4.16) can be declared valid in the narrow sense only for the particular locations, times and settings the data were obtained (figure 4.29). But the apparent ease with which data from a span of latitudes, stratifications and diverse oceanic settings can be unified without contradiction, could support the more optimistic statement that equation (4.16) be a good estimate for: open ocean regions at latitudes of 5° to 40°, the internal wave field not stronger than 10 times the GM model value, and a wide range of stratification $N^2 = 1 \cdot 10^{-6}$ *to* $1 \cdot 10^{-4}\ \frac{rad^2}{s^2}$ that may be expected beneath the mixed layer and the sharpest thermocline.

As more data coverage in parameter space (Ψ_1, Ψ_2) and oceanic settings lacks, further extrapolations most certainly will fail; obvious cases being the equatorial regime with $f = 0$ and the one strongly topographically influenced value $F\,3$ from [Polzin et al., 1995]'s reported data.

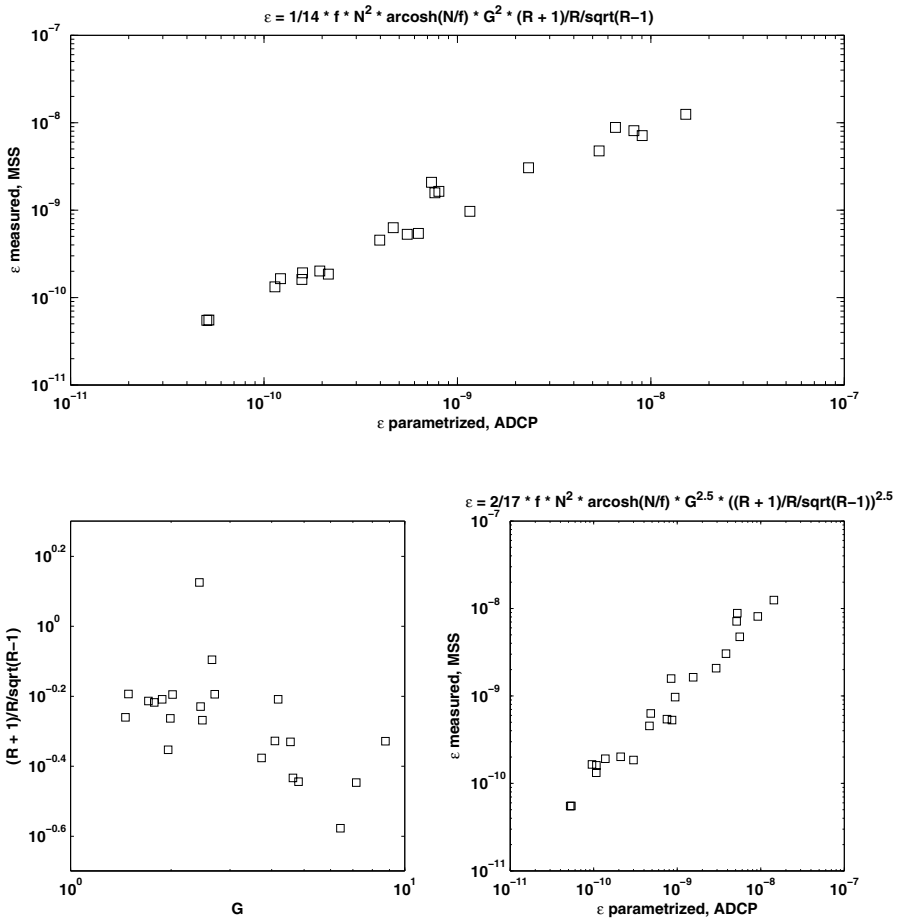

Fig. 4.30: Ambiguity of state-of-the-art ϵ-parametrization, based on [Polzin et al., 1995] reported data. Upper panel: Fit to Henyey-Polzin-Gregg parametrization as of equation 4.14. Lower left: correlation of shear spectral level and shear-to-strain-ratio-containing term. Lower right: alternative optimum parametrizational fit for different exponent choice.

ADCP based estimate of regional K field

One important aim of doing vmADCP based K estimates was to expand the available database for the estimate of a regional representative integral diapycnal diffusion coefficient. Accounting for the decorrelation time of roughly 3 hours (subsection 4.2.6), the two cruises have delivered about 400 independent local $\bar{K}$ estimates, in contrast to 34 microstructure station based $\bar{K}$ values. The ADCP based 'continuous' $\bar{K}$ values (figure 4.23) allow additional deductions: i) an estimate of typical horizontal scales of shear structures (30 km to 100 km very common), ii) an indication that representative regional sampling is possible within a reasonable amount of stations (ADCP based integral $\langle K \rangle$ = MSS based integral $\langle K \rangle$ within 10%), iii) without a priori knowledge, such regional sampling should imply short stations at many locations rather than few longtime occupations (spatial inhomogeneities of high endurance or even permanence seem to exist, cf. subsection 4.4.3), iv) though the regional average $\bar{K}$ is dominated by large single K values, the role of very rare very strong shear events that we might have missed seems to be negligible, at least in the GUTRE timeframe of 2 years (ADCP based integral $\langle K \rangle$ = GUTRE tracer based integral $\langle K \rangle$ within 10%).

Due to the better area coverage compared to microstructure measurements, the vmADCP based regional average $\langle K \rangle$ is deemed the best estimate to be reported as integral $\langle K \rangle$ of Guinea Dome Region in the main thermocline:

$$\langle K \rangle_{GDR} = \left(1.2 \cdot 10^{-5} \pm 0.2 \cdot 10^{-5}\right) \frac{m^2}{s} \tag{4.17}$$

with 95% confidence limit based on method-inherent error and bootstrap resampling.

Influences on regional K distribution

In trying to find causes for the regional segmentation in $\langle K \rangle$ (subsection 4.4.3) we unexpressedly assumed wind not to exhibit such longterm ($O(1\,month)$) regional patterns in its potential to create near-inertial waves, that the $\bar{K}$ patterns and their common features could be explained. This assumption is firsthand plausible for a tradewind region, but also gets supported by a study of [Alford, 2001] for the years 1996 to 1999 and from a more focused own check for Guinea Dome Region via NCEP wind reanalysis data [Kalnay et al., 1996] for the cruise months November 2008 and December 2009.

Generation locations of near-inertial internal waves inferred from an NCEP forced slab ocean model for early winter of the 'typical year 1997' [Alford, 2001] show up as patches of increased energy flux into the mixed layer (figure 4.31). Energy flux at 2° to $15^\circ\,N$ and 35° to $15^\circ\,W$ appears homogeneous and overall minor compared to midlatitudes; both these characteristics resting unchanged during all seasons.

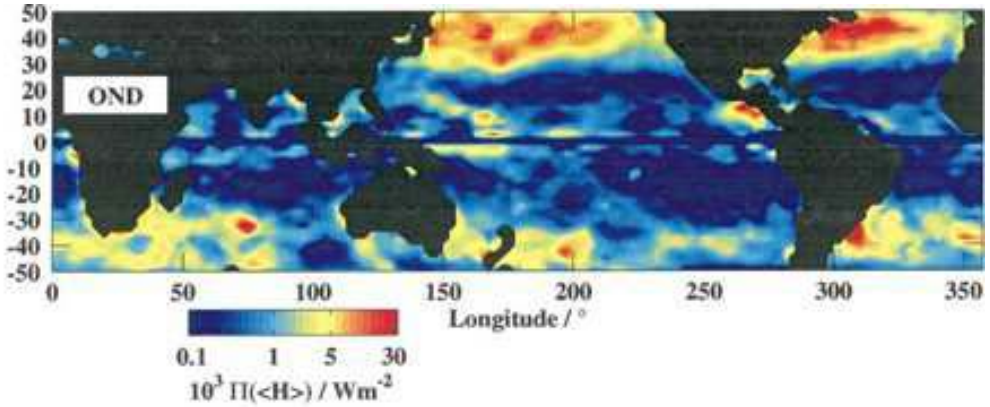

Fig. 4.31: Near-inertial energy flux into the ocean mixed layer, based on NCEP winds and a slab ocean model, as reported by [Alford, 2001] for the fourth quartal of 'typical year 1997'. Guinea Dome Region supply with near-inertial internal waves is rather low and homogeneous.

Following [Alford, 2001] in his rating that the 'inertial component of the wind field' should exhibit similar patterns to the inertial energy flux patterns of his model, we calculate the difference of clockwise and counterclockwise near-inertial NCEP wind energy and overlay it to according $\bar{K}$ fields for the two cruises in November 2008 and December 2009 (figure 4.32). The emanating picture is at best inconclusive, but rather denying a correlation between the regional wind pattern and patterns of elevated $\bar{K}$. In November 2008 essentially all cruise saw a weak positive inertial wind energy surplus, regions of low and elevated $\bar{K}$ alike. In December 2009 all four possible combinations of elevated/low wind inertial energy surplus and elevated/low $\bar{K}$ do occur at roughly equal area coverage, thus suggesting independence of the two parameters. However for both months a maximum in the overall modest inertial wind energy coincides with the location of the seamountain range. That leaves some ambiguity but cannot overrule the general impression of uncorrelatedness and lack of explanation for the rather abrupt changes in $\bar{K}$ pattern with abyssal plain limits (cf. figure 4.28).

On the other hand regional patterns in $\bar{K}$ match basic topographic features, particularly distinct at the triad abyssal plain A_1 - seamountain range B - abyssal plain A_2 (figure 4.28). When comparing regional averages of measured $\bar{K}$ to expected values for GM background internal wave fields at that same latitude (table 4.2), [Gregg et al., 2003]'s given parametrization equivalent to (4.15) fits the two abyssal plain regions and the Cape Verdian area. Meanwhile the seamount region B and the topographically rather poorly constrained Western region D show twice the 'Gregg'-K-value; but a somewhat elevated internal wave activity, expressed as relative shear spectral level G, would be sufficient for a fit. Thus the simplest explanation for the 30% elevated $\langle K \rangle$ in Guinea Dome Region, as compared to expectation and to the well behaved abyssal plains, is the effect of topographically enhanced internal wave activity. This is very plausible for the seamountain range with occasional upwards propagating wave groups, but less clear for the Western region. Concerning the possible vertical range that internal tides can perceptably affect, there is no common

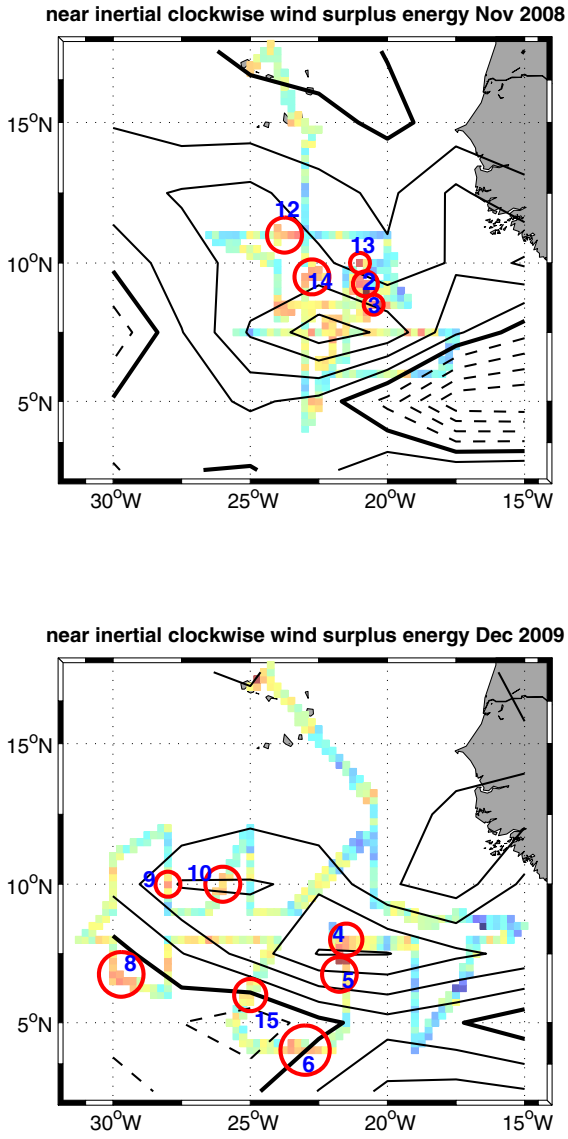

Fig. 4.32: Near-inertial clockwise wind energy surplus as an indicator of near-inertial energy flux into the ocean for both cruises. Contour lines in arbitrary units: bold line = zero; solid lines = positive; dashed lines = negative. For comparison, vmADCP based $\bar{K}$ estimates are given and patches of coherent elevated $\bar{K}$ marked (enumeration according to table 4.1).

partition		latitude	$N^2 \,/\, 10^{-5}$	$K \,/\, 10^{-5}$	$K_{Gregg} \,/\, 10^{-5}$
A_1	Abyssal plain North	12°	1	1.1	1.2
A_2	Abyssal plain East	7°	1.8	0.8	0.8
B	Seamountain range	7°	1.5	1.5	0.8
C	Cape Verdian archipel	16°	1.5	1.5	1.5
D	Western region	8°	1.2	1.5	0.8
	Total	9°	1.5	1.2	0.9

Table 4.2: Comparison of regional $\bar{K}$ averages estimated from ADCP to expected $\bar{K}$ from [Gregg et al., 2003]'s state-of-the-art parametrization when assuming GM background state of internal wave field. Partitions according to figure 4.28.

opinion [Wunsch and Ferrari, 2004], but [Kunze et al., 2006]'s measurements along diverse basin wide sections, their figures 5 to 11, support the idea that internal tide energy might reach the upper ocean, even from topographic features 4000m deep.

There may be a third player in the internal wave concerto besides near-inertial waves and internal tides. The wave packet we observed at $4° N$ $23° W$ (number 6 in table 4.1) possibly is a wind driven, but shear induced wave as described by [Townsend, 1968; Stevens and Imberger, 1994]. The frequency is clearly far from near-inertial, group velocity downward, and the wave group seems too undispersed to be a reflected internal tide harmonic. Further regarding that the mixed layer moves more or less meridionally across the upper shear zone of a zonal jet (figure 4.25), could explain the shedding of mainly meridionally propagating waves. The detection of this one wave packet was luck due to a 4 hour ship station at that spot. But there is indication that such phenomena might occur more frequently in that region. Without possibility to actually check for the presence of this kind of wave, of 11 historical sections $4° N$ to $14° N$ on $23° W$, 10 show one or two of these strong-shear-above-zonal-jets constellations, often about 1 degree in latitudinal extent.

In the light of our results suggesting that background GM internal wave shear levels are mainly to be expected above abyssal plains, while other topographic features can display higher G values in the main thermocline - a view that is supported by the exhaustive compiled dataset of [Kunze et al., 2006] - what may be expected for the fraction of "well behaved" area on global scales? Focusing on the belt $15° S$ to $15° N$, hardly half of the ocean bottom is abyssal plain (figure 4.33, abyssal plains characterized in our crude sense by topographic parameter $To \leq 3$, a threshold that can be justified from figure 4.27).

Thus adaptation of parametrizational estimates of $\bar{K}$ for the global ocean, from assuming that the internal wave field exhibits GM background level everywhere in the upper ocean, and without further observational backing, might be misleading. For testing the response of a Global Circulation Model, [Jochum, 2009] gives a suggestive exemplary global K map at 200 m level (figure 4.34) without claiming perfectness. Recognizing the reported distinct sensitivity of Global Circulation Models to dis-

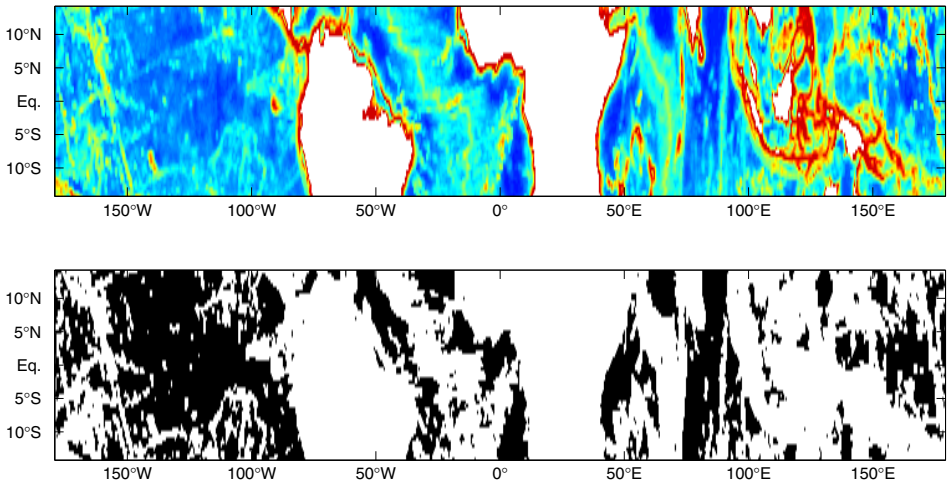

Fig. 4.33: Topography parameter To for global $15° S$ to $15° N$ belt (upper panel) and estimated abyssal plain location from $To \leq 3$ (black patches on lower panel). Abyssal plain area thus defined is 45% of total ocean area (continental slopes excluded) in belt.

tribution patterns of topography mediated mixing [Simmons et al., 2004; Jayne, 2009], and anticipating similar sensitivity to mixing patterns in other ocean layers, incorporating detailed K information for model constraint seems helpful. Depending on how much detail will be needed in the end to get stable plausible results, and depending on how fast K observations proceed, the anticipated patchiness in global K distribution could mean there is still some way ahead.

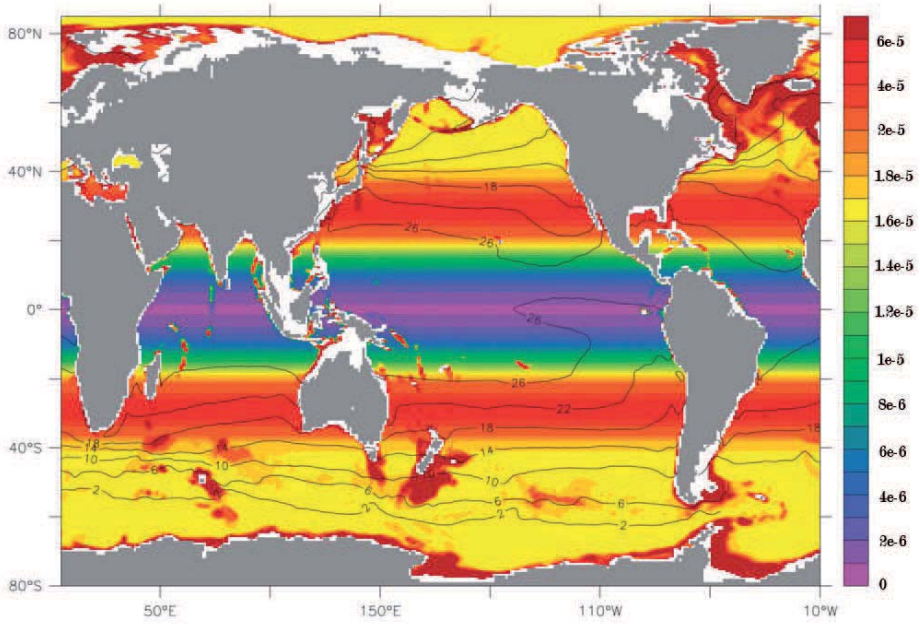

Fig. 4.34: K on its way to become spatial: a global K field in 200 m depth, used by [Jochum, 2009] for sensitivity studies of a Global Circulation Model to spatial K variation.

5 Diapycnal fluxes of oxygen and nitrous oxide

5.1 General and special remarks when inferring diapycnal fluxes

Immediate fluxes that result from diffusion or turbulent diffusion acting on a concentration gradient can be expressed as

$$\Phi_c = -\rho\, K\, \nabla c \tag{5.1}$$

with c concentration in mol/kg, K diffusion coefficient in m^2/s, ρ density of water in kg/m^3 and Φ_c the resulting downgradient flux of substance in $mol/m^2/s$. Here we are interested in diapycnal fluxes, so K is diapycnal diffusion and the gradient is taken as vertical for convenience and without perceptible loss of precision. Although for discussing concepts we will stay in depth space, for calculating fluxes it is convenient to swap to density space, in order to get rid of concentration profile deformations caused by the ubiquitous internal waves. So

$$\Phi_c = -\rho\, K\, \frac{\partial c}{\partial z} = -\rho\, K\, \frac{\partial c}{\partial \sigma}\, \frac{d\sigma}{dz} = \rho\, K\, \frac{\partial c}{\partial \sigma}\, N^2\, \frac{\rho}{g} \tag{5.2}$$

according to the common expression for buoyancy frequency N, and with σ potential density minus $1000\, kg/m^3$ and g gravitation. Introduction of the Osborn parametrization for K (equation 3.6) with dissipation ratio $\Gamma = 0.2$ leads to

$$\Phi_c = 0.2\, \frac{\rho^2}{g}\, \epsilon\, \frac{\partial c}{\partial \sigma} \tag{5.3}$$

with dissipation rate ϵ that can for example be delivered by microstructure measurements or parametrization of finescale shear observations by ADCP as in our case.

The Osborn parametrization delivers effective K on scales not smaller than say $O(10\, m)$, as ϵ and N^2 must be values representative for such scales in order to allow

the balancing of turbulent kinetic energy that this parametrization relies on, one reason being the assumed steady state [Osborn, 1980]. That implies that mixing effects resulting from ϵ and N^2 fluctuating on smaller scales are nonetheless included in the resulting effective K. So for the following reasoning it is sufficient to regard $O(10\,m)$ as the depth scale for K.

K acting on $\frac{\partial c}{\partial z}$ can only change the concentration gradient markedly on timescales T as of

$$\frac{L^2}{T} \sim 2\,K \tag{5.4}$$

(a Gaussian diffusion model assumed) with L depth scale. So distinct changes of concentration gradient on the depth scale of 10m would be expected for

$$T \sim \frac{50\,m^2}{K}. \tag{5.5}$$

For the depth range of 150m to 500m in Guinea Dome Region, patches of $K = 10^{-4}\,\frac{m^2}{s}$ with thickness 10m are already remarkable (K as large as $10^{-3}\,\frac{m^2}{s}$ never longlived enough to last much more than an hour). The resulting timescale of $O(100\,h)$ that would be needed by a stationary patch of $K = 10^{-4}\,\frac{m^2}{s}$ to markedly modify the concentration gradient, is just about the longest time that the slowest possible internal wave in GDR needs to perform one cycle - that is, that wave's shear zones will traverse one vertical wavelength (typically of order 100m for near inertial waves here) in $O(100\,h)$. So the time that patches of K may be regarded as stationary is expectedly always shorter than the time needed to deform the concentration profile, in GDR at that depth range. Thus concentration profiles may be regarded as stationary in comparison to K on timescales of $O(1\,d)$ (that we have K estimates for, see section 4.3), and via the argument for K, also inferred diapycnal fluxes from equation 5.1 are expected to include effects from smaller mixing scales.

This longish scaling argument does not rule out the possibility of lateral intrusions of small vertical scale that would not change the mean concentration gradient but add/substract concentration via diapycnal diffusion at the intrusions' limits. But on the depth scale of $O(10\,m)$ these diapycnal processes can be regarded as subscale, and the resulting change in concentration for that water parcel is regarded as caused by lateral eddy diffusion here. For the aimed calculations of OMZ oxygen and nitrous oxide fluxes, it may even be considered rather helpful that flux calculations from equations 5.1 or 5.3, with K and concentration gradients defined on scales $O(10\,m)$ do exclude such subscale nuisance.

For much longer timescales than $O(1\,d)$ and/or spatial scales larger than the coherent patch scale of $O(10\,km)$ to $O(100\,km)$ (subsection 4.4.3), there is no obvious reason why K and concentration gradient should be independent. Instead it is well

imaginable that stronger mixing could coincide with weaker gradients and vice versa, resulting in a negative correlation. Introducing the nomenclature of an overbar denoting medium timescale averaging on $O(1\,d)$ and angled brackets denoting regional spatial averaging, the regional average diapycnal flux will be

$$\Phi_c \propto \left\langle \overline{K} \cdot \overline{\left(\frac{\partial c}{\partial z}\right)} \right\rangle = \left\langle \overline{K} \right\rangle \cdot \left\langle \overline{\left(\frac{\partial c}{\partial z}\right)} \right\rangle + \left\langle \left(\overline{K} - \left\langle \overline{K} \right\rangle\right) \cdot \left(\overline{\left(\frac{\partial c}{\partial z}\right)} - \left\langle \overline{\left(\frac{\partial c}{\partial z}\right)} \right\rangle \right) \right\rangle \tag{5.6}$$

or

$$\Phi_c \propto \left\langle \overline{\epsilon} \cdot \overline{\left(\frac{\partial c}{\partial \sigma}\right)} \right\rangle = \left\langle \overline{\epsilon} \right\rangle \cdot \left\langle \overline{\left(\frac{\partial c}{\partial \sigma}\right)} \right\rangle + \left\langle \left(\overline{\epsilon} - \left\langle \overline{\epsilon} \right\rangle\right) \cdot \left(\overline{\left(\frac{\partial c}{\partial \sigma}\right)} - \left\langle \overline{\left(\frac{\partial c}{\partial \sigma}\right)} \right\rangle \right) \right\rangle . \tag{5.7}$$

The first terms on the right hand sides represent the flux contributions to be calculated from regional average profiles, while the second terms represent the flux contributions caused by the profiles' correlation. Our data in oxygen and K are numerous and equally distributed enough in GDR, so the importance of the correlation term can be estimated after calculating mean flux, mean K and mean gradient.

5.2 Diapycnal oxygen flux from above into the OMZ

There is a remarkable similarity in the characteristic shape of oxygen profiles in GDR, a typical member shown in figure 5.1. We only have a regional set of $\bar{K}$ for the depth range above the oxygen minimum core, in depth approximately coinciding with the domain of South Atlantic Central Water SACW, so flux estimates must be confined to here. The profile may be read as revealing the oxygen supply via incoming currents or eddies, distinct in 100m to 300m. The small-scale undulations is probably indicating lateral exchange with patches of lower and/or higher oxygen concentration. Above, there is for most of GDR a shallow oxygen minimum. That means there is no oxygen flux from the surface through to the main oxygen minimum, only oxygen from SACW is reaching the upper half of the OMZ.

In the vicinity of the oxygen minimum core the profile looks rather parabolic. Whatever the reason, it means that diapycnal flux divergence in these depths should be rather constant, as K is about constant here (cf. figure 4.19). Meanwhile the total diapycnal oxygen influx across an arbitrarily chosen upper OMZ limit depends heavily on the actual limit position. Thus it seems reasonable to define the upper limit of the OMZ to be just below the upper limit of the near parabolic shape and to calculate diapycnal influx there - but to rely on deduced average diapycnal flux divergence

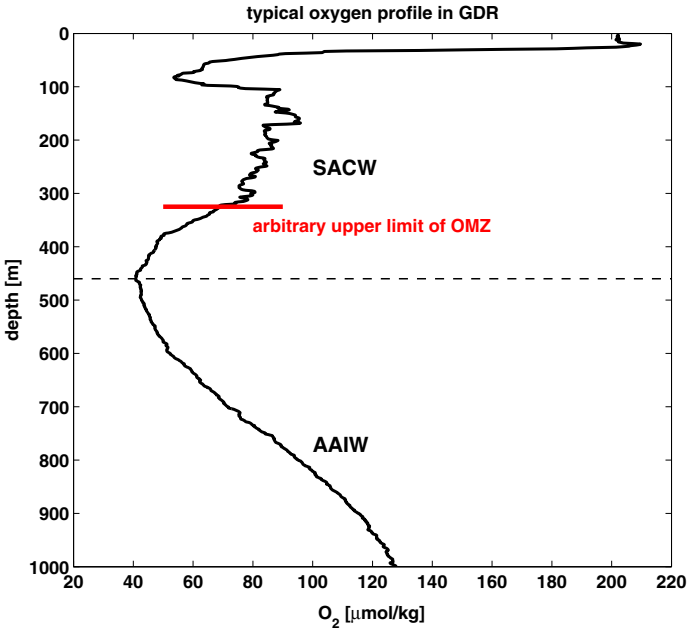

Fig. 5.1: Characteristic oxygen profile in Guinea Dome Region. The oxygen minimum core divides South Atlantic Central Water SACW and Antarctic Intermediate Water AAIW. The upper limit where diapycnal oxygen influx is to be calculated is defined as the upper limit of the near-parabolic profile shape.

$$\overline{\nabla \Phi_{O_2}} = \frac{\Phi_{O_2}}{depth_{core} - depth_{limit}} \tag{5.8}$$

in order to represent the contribution of diapycnal oxygen flux to OMZ total oxygen supply.

Figure 5.2 assembles maps of ϵ, $\frac{\partial c}{\partial \sigma}$ and inferred diapycnal oxygen downflux into the upper half of the OMZ. The mean flux after area weighted averaging is $\Phi_{O_2} = -6.2 \cdot 10^{-3} \pm 0.7 \cdot 10^{-3} \frac{\mu mol}{m^2\, s}$ corresponding to a mean flux divergence of $\nabla \Phi_{O_2} = -1.7 \pm 0.2 \frac{mmol}{m^3\, a}$. Uncertainties are 95% confidence limits calculated via bootstrapping.

Compared to the total oxygen consumption in the OMZ of estimated 5 to 6 $\frac{mmol}{m^3\, a}$ [Karstensen et al., 2008] or 2 to 3 $\frac{mmol}{m^3\, a}$ [Brandt et al., 2010], this would mean a 25% to more than 50% contribution to the necessary oxygen resupply of the upper half of the OMZ. For the lower half of the OMZ there is just scarce observed mixing data, but if K is taken to be the same here as above plus some double diffusive mixing added as expected (chapter 2), diapycnal oxygen flux from below could be of same order as the diapycnal oxygen flux from above.

The spatial distributions of figure 5.2 suggest that oxygen flux variability is mainly caused by mixing variability, but the higher oxygen gradients accumulated in the West of GDR support the notion of easterly jets bringing the oxygen into the region.

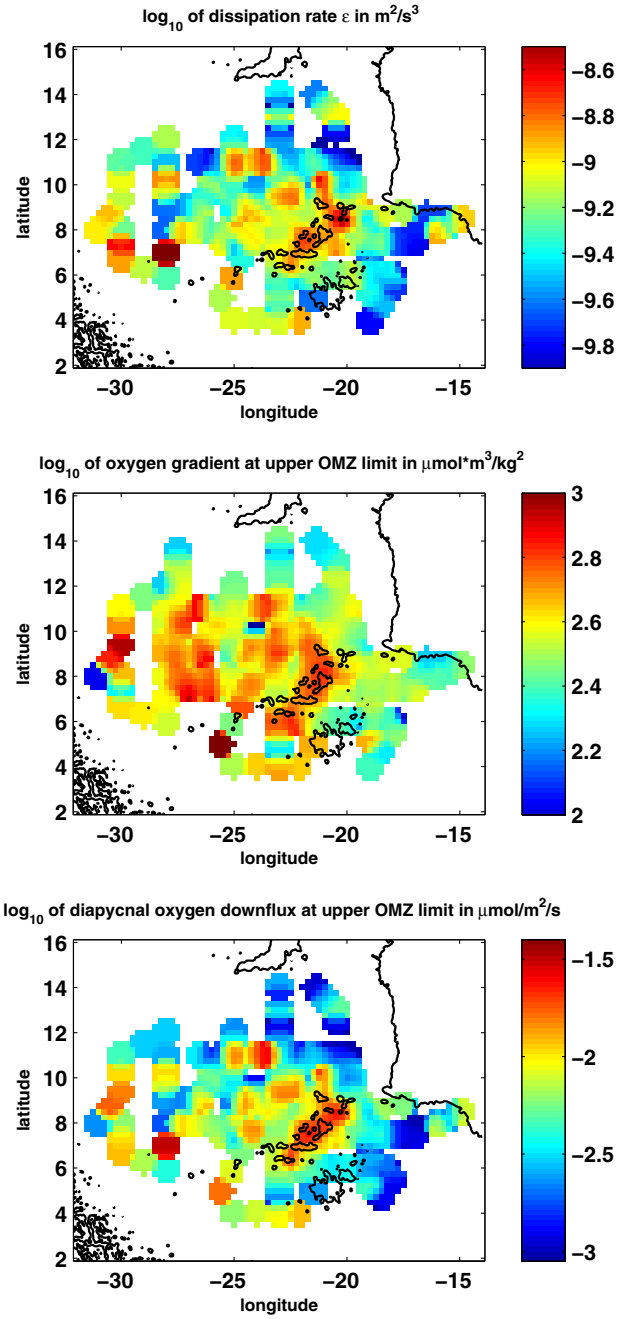

Fig. 5.2: Spatial distribution of dissipation ϵ, oxygen gradient at upper OMZ limit and inferred local oxygen influx into the upper half of the OMZ. Black lines are the 3000m isobath. Resulting regional average oxygen influx is $\Phi_{O_2} = -6.2 \cdot 10^{-3} \pm 0.7 \cdot 10^{-3} \frac{\mu mol}{m^2\, s}$.

Finally, comparing the regional average flux

$$\Phi_{O_2} = 0.2\,\frac{\rho^2}{g}\left\langle \bar{\epsilon}\cdot\overline{\left(\frac{\partial c}{\partial \sigma}\right)}\right\rangle \tag{5.9}$$

to the flux resulting from an average dissipation value $\langle\bar{\epsilon}\rangle$ and an average gradient $\left\langle\overline{\left(\frac{\partial c}{\partial \sigma}\right)}\right\rangle$ (which would result in $\Phi_{O_2} = -6.0{\cdot}10^{-3} \pm 0.7{\cdot}10^{-3}\,\frac{\mu mol}{m^2\,s}$) reveals that mixing intensity and oxygen gradients at upper OMZ limit seem to be independent in GDR. So calculating regional fluxes from regional average mixing and concentration profiles might be an option, given that ϵ and gradient averages do represent the region well. For sparse datasets, such flux estimate might even be superior (again given that ϵ and gradient averages do represent the region well), as there is some probability that the small sample of local fluxes might exhibit spurious correlation.

5.3 Diapycnal nitrous oxide flux from the OMZ

The ocean is a natural source to the atmosphere of nitrous oxide (N_2O), which is a potent greenhouse gas that is also depleting ozone [IPCC, 2007]. It is produced by nitrifying and denitrifying microbes as a by-product or intermediate product, respectively [Walter et al., 2006]. Relatively high concentrations in the Tropical Northeastern Atlantic have been found before [Wallace and Bange, 2004], with maxima in the OMZ core. During cruises MSM10/1 and M80/2 13 profiles of simultaneous N_2O and microstructure profiles have been sampled.

The characteristic N_2O profile shape is inversely related to oxygen, one example displayed here (figure 5.3). Whether there is a causality behind this relation is rather unclear. [Frame and Casciotti, 2010] report little influence of oxygen concentration on N_2O production by a cultured nitrifier at realistic oceanic cell concentrations. It is well possible that it GDR oxygen consumption and N_2O production just go antiparallel in time while watermasses slowly ventilate the OMZ.

Having observed the antiparallel relation of N_2O and oxygen, it seems reasonable to calculate N_2O-outflux leaving the OMZ and flux divergence in complete analogy to oxygen (section 5.2): determine N_2O-gradient in density space at upper limit of the OMZ (as fixed from oxygen profile for its better resolution), calculate diapycnal flux there by using measured dissipation rate ϵ and equation 5.3 (figure 5.4), then calculate flux divergence for the upper half of the OMZ. Area weighted averages then become $\Phi_{N_2O} = 1.0 \cdot 10^{-3} \pm 0.4 \cdot 10^{-3}\,\frac{nmol}{m^2\,s}$ and $\nabla\Phi_{N_2O} = 250 \pm 100\,\frac{nmol}{m^3\,a}$, their values a factor of about 6000 smaller than related oxygen flux and flux divergence. Estimating Φ_{N_2O} from regional average profiles of ϵ and N_2O concentration yields $\Phi_{N_2O} = 0.9 \cdot 10^{-3} \pm 0.4 \cdot 10^{-3}\,\frac{nmol}{m^2\,s}$, again close to the regional average flux, despite the small number of samples.

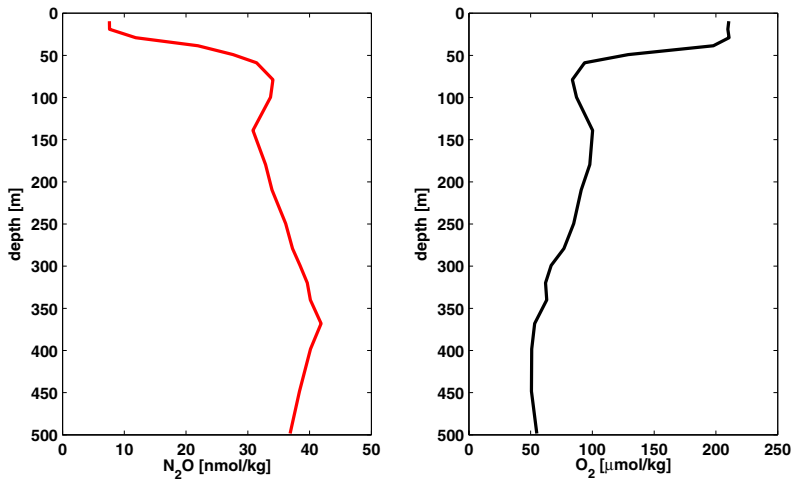

Fig. 5.3: Example profiles of nitrous oxide and oxygen at $12° N$ and $25° W$ in December 2009

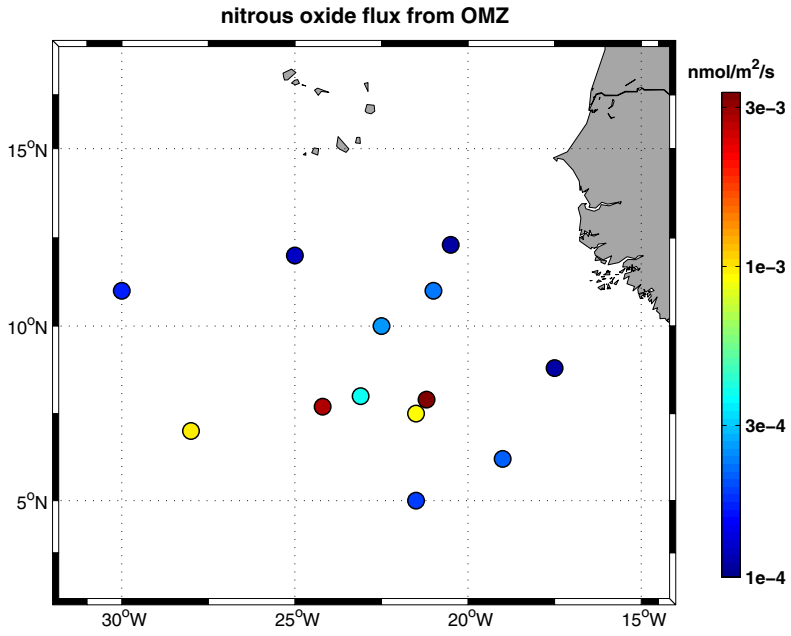

Fig. 5.4: Upward diapycnal flux of N_2O from the upper half of the OMZ for stations of simultaneous microstructure and N_2O measurements during cruises MSM10/1 and M80/2. The inferred regional average flux is $\Phi_{N_2O} = 1.0 \cdot 10^{-3} \pm 0.4 \cdot 10^{-3} \frac{nmol}{m^2\, s}$.

[Freing et al., 2009] report N_2O production rates from Atlantic ocean midlatitudes and find values of $\dot{q} = 500 \pm 300 \frac{nmol}{m^3 a}$ for the depth range 100m to 500m (taken from their figure 7). If such values should be accurate for GDR, too, this would indicate an important contribution of diapycnal diffusion to total N_2O outflux from the upper half of the OMZ, and confirm the results found for oxygen.

Note that calculated upward diapycnal outflux of N_2O from the upper half of the OMZ is only to South Atlantic Central Water. The further fate of this N_2O is unclear. Further production of N_2O in the upper layers is probable as nitrification seems possible anywhere in the water column [Yool et al., 2007].

6 Summary

An indirect acoustic method to infer upper ocean finescale shear variance from a moving vessel by Acoustic Doppler Current Profiler (vmADCP) is developed and implemented. It is shown that estimating dissipation rate ϵ and diapycnal exchange coefficient/diapycnal diffusion K from finescale shear is possible. From own microstructure calibration measurements, backed by the outcome of a simultaneous tracer release experiment, and by including measurements reported by Polzin et al. [1995] enhancing the dataset's range in latitude and stratification, a parametrization for ϵ as function of Coriolis parameter, buoyancy frequency and finescale shear variance is developed. If aware that only the part of diapycnal mixing due to finescale shear/breaking internal waves may be deduced this way, vmADCP usage is featuring enhanced area coverage for diapycnal mixing data at low operational costs, and with no extra shiptime needed.

Guinea Dome Region in the depth range below the sharp thermocline and above the oxygen minimum core (150 to 400 m roughly) seems to be diapycnally mixed by shear instability/breaking internal waves alone. The regional integral $K = 1.2 \cdot 10^{-5} \pm 0.2 \cdot 10^{-5} \frac{m^2}{s}$ is slightly above the expected value for background internal wave activity in these latitudes. This is most possibly caused by local topographically enhanced internal waves. Below the oxygen minimum core from 400 m downward, double diffusion is expected to enhance diapycnal mixing.

A competitive number of oxygen profiles from two cruises in conjunction with the inferred K field from vmADCP allows to estimate the diapycnal influx of oxygen from above into the upper half of the oxygen minimum zone (OMZ) off West Africa as $\Phi_{O_2} = -6.2 \cdot 10^{-3} \pm 0.7 \cdot 10^{-3} \frac{\mu mol}{m^2\, s}$. Expressed as a constant flux divergence inside the OMZ it is $\nabla\Phi_{O_2} = -1.7 \pm 0.2 \frac{mmol}{m^3\, a}$, forming a substantial contribution to resupplying oxygen loss: a quarter to one half, depending on estimates of total consumption. The spatial distribution of oxygen gradient and oxygen flux in Guinea Dome Region is in concordance with the notion that oxygen is brought to the OMZ by zonal jets and eddies from the West. The greenhouse gas nitrous oxide takes the reverse diapycnal pathway out of the OMZ into the water above at a flux estimated to $\Phi_{N_2O} = 1.0 \cdot 10^{-3} \pm 0.4 \cdot 10^{-3} \frac{nmol}{m^2\, s}$; with a flux divergence of $\nabla\Phi_{N_2O} = 250 \pm 100 \frac{nmol}{m^3\, a}$ in the upper half of the OMZ.

7 Acknowledgments

This is the place to give thanks to several people

Prof. Dr. Peter Brandt for his exemplifying scientific quality and his laugh in the aisle

Dr. Marcus Dengler who is equipped with enormous background knowledge and piles of papers, for many fruitful discussions out in the smoker's exile

Prof. Dr. Martin Visbeck, Mr GUTRE, without whom I presumably would not have found interest in this ocean spot

Dr. Johannes Karstensen for the monthly expert opinion

the secretaries' fire brigade, Sigrun Komander-Hoepner and Nadira Mahmud

the double diffusive people, Dr. Heiner Dietze for bringing St.Laurent & Schmitt to my attention, and Dr. Mirjam Gleßmer who recently diffused to Norway, and once enthusiastically brought that field to my horizon

the many colleagues and present and have been fellow students for their warm words

the Marine Chemist's Realm vis-à-vis, Dr. Hermann Bange and the host of grad students, particularly Annette Kock in her tireless commitment to measure laughing gas

the enduring and friendly crews of Merian and Meteor, and the very abled Fahrtleiters

A. Huber for his trying to teach us his unreachable clearness of thought

Special thanks to the unique Manuel Brito, the Cape Verdian members of INDP and the crew of RV Islandia. Another seasickness is possible.

And not least I am grateful for funding by BMBF-SOPRAN.

and to some valuable public data sources

NCEP Reanalysis data provided by the NOAA/OAR/ESRL PSD, Boulder, Colorado, USA, from their Web site at http://www.esrl.noaa.gov/psd/

ETOPO1 Global bathymetry data provided by NOAA National Geophysical Data Center, from their Web site at http://www.noaa.gov/mgg/

Bibliography

Alford, M. H. (2001). Internal swell generation: The spatial distribution of energy flux from the wind to mixed layer near-inertial motions. *J. Phys. Oceanogr. 31*, 2359–2368.

Alford, M. H. (2008). Observations of parametric subharmonic instability of the diurnal internal tide in the South China Sea. *Geophys. Res. Lett. 35*, L 15602, doi:10.1029/2008GL034720.

Amante, C. and B. W. Eakins (2009). Etopo1 1 arc-minute global relief model: Procedures, data sources and analysis. *NOAA Technical Memorandum NESDIS NGDC-24*.

Banyte, D. (2011). pers. comm.; grad student with Prof. M. Visbeck, IFM-GEOMAR.

Brandt, P., V. Hormann, A. Koertzinger, M. Visbeck, G. Krahmann, L. Stramma, R. Lumpkin, and C. Schmid (2010). Changes in the ventilation of the oxygen minimum zone of the tropical north Atlantic. *J. Phys. Oceanogr. 40*, 1784–1801.

Cairns, J. and G. Williams (1976). Internal wave observations from a midwater float, 2. *J. Geophys. Res. 81(12)*, 1943–1950.

D'Asaro, E. A. (1984). Wind forced internal waves in the north Pacific and Sargasso Sea. *J. Phys. Oceanogr. 14*, 781–794.

Davis, R. (1996). Sampling turbulent dissipation. *J. Phys. Oceanogr. 26*, 341–358.

Dengler, M. and D. Quadfasel (2002). Equatorial deep jets and abyssal mixing in the Indian Ocean. *J. Phys. Oceanogr. 32*, 1165–1180.

Doi, T., T. Tozuka, and T. Yamagata (2010). The atlantic meridional mode and its coupled variability with the Guinea Dome. *J. Climate 23*, 455–475.

Duda, T. F. and C. S. Cox (1989). Vertical wave number spectra of velocity and shear at small internal wave scales. *J. Geophys. Res. 94(C1)*, 939–950.

Efron, B. (1987). Better bootstrap confidence intervals. *J. Amer. Stat. Assoc. 82(397)*, 171–185.

Ferrari, R. and K. Polzin (2005). Finescale structure of the T-S relation in the eastern north Atlantic. *J. Phys. Oceanogr. 35*, 1437–1454.

Fischer, J., P. Brandt, M. Dengler, M. Müller, and D. Symonds (2003). Surveying the upper ocean with the ocean surveyor: A new phased array doppler current profiler. *J. Atmos. Oceanic Technol. 20*, 742–751.

Frame, C. H. and K. L. Casciotti (2010). Biogeochemical controls and isotopic signatures of nitrous oxide production by a marine ammonia-oxidizing bacterium. *Biogeosciences 7*, 2695–2709.

Freing, A., D. W. R. Wallace, T. Tanhua, S. Walter, and H. W. Bange (2009). North atlantic production of nitrous oxide in the context of changing atmospheric levels. *Global Biogeochem. Cycles 23*, GB4015 doi:10.1029/2009GB003472.

Garabato, A. C. N., K. L. Polzin, B. A. King, K. J. Heywood, and M. Visbeck (2004). Widespread intense turbulent mixing in the Southern Ocean. *Science 303*, 210–213.

Gargett, A. (1976). An investigation of the occurrence of oceanic turbulence with respect to finestructure. *J. Phys. Oceanogr. 6*, 139–156.

Gargett, A. (1990). Do we really know how to scale the turbulent kinetic energy dissipation rate ϵ due to breaking of oceanic internal waves? *J. Geophys. Res. 95(C9)*, 15971–15974.

Gargett, A. (1994). Observing turbulence with a modified ADCP. *J. Atmos. Oceanic Technol. 11*, 1592–1610.

Gargett, A., P. Hendricks, T. Sanford, T. Osborn, and A. WilliamsIII (1981). A composite spectrum of vertical shear in the upper ocean. *J. Phys. Oceanogr. 11*, 1258–1271.

Gargett, A., T. Osborn, and P. W. Nasmyth (1984). Local isotropy and the decay of turbulence in a stratified fluid. *J. Fluid Mech. 144*, 231–280.

Garrett, C. and W. Munk (1972). Space-time scales of internal waves. *Geophys. Fluid Dyn. 2*, 225–264.

Garrett, C. and W. Munk (1975). Space-time scales of internal waves: A progress report. *J. Geophys. Res. 80(3)*, 291–297.

Gonella, J. (1972). A rotary-component method for analysing meteorological and oceanographic vector time series. *Deep Sea Res. 19*, 833–846.

Gregg, M. (1989). Scaling turbulent dissipation in the thermocline. *J. Geophys. Res. 94(C7)*, 9686–9698.

Gregg, M. and E. Kunze (1991). Shear and strain in Santa Monica Basin. *J. Geophys. Res. 96(C9)*, 16709–16719.

Gregg, M. and T. B. Sanford (1988). The dependence of turbulent dissipation on stratification in a diffusively stable thermocline. *J. Geophys. Res. 93(C10)*, 12381–12392.

Gregg, M., T. B. Sanford, and D. P. Winkel (2003). Reduced mixing from the breaking of internal waves in equatorial waters. *Nature 422*, 513–515.

Gregg, M., D. P. Winkel, and T. B. Sanford (1993). Varieties of fully resolved spectra of vertical shear. *J. Phys. Oceanogr. 23*, 124–141.

Hayes, S. P., H. Milburn, and E. Ford (1984). TOPS: A free-fall velocity and CTD profiler. *J. Atmos. Oceanic Technol. 1*, 220–236.

Henyey, F. S., J. Wright, and S. Flatte (1986). Energy and action flow through the internal wave field: an eikonal approach. *J. Geophys. Res. 91(C7)*, 8487–8495.

IPCC (2007). *Climate Change 2007: Synthesis report. Contribution of Working Groups I, II and III to the fourth Assessment report of the Intergovernmental Panel on Climate Change, 104 pp.* IPCC.

ISW Wassermesstechnik Dr. Hartmut Prandke (2009). *PNS03/06 shear probes for microstructure measurements. Product information.* ISW Wassermesstechnik Dr. Hartmut Prandke.

Itsweire, E. C., T. Osborn, and T. Stanton (1989). Horizontal distribution and characteristics of shear layers in the seasonal thermocline. *J. Phys. Oceanogr. 19*, 301–320.

Jayne, S. R. (2009). The impact of abyssal mixing parameterizations in an ocean general circulation model. *J. Phys. Oceanogr. 39*, 1756–1775.

Jayne, S. R. and L. C. StLaurent (2001). Parameterizing tidal dissipation over rough topography. *Geophys. Res. Lett. 28(5)*, 811–814.

Jochum, M. (2009). Impact of latitudinal variations in vertical diffusivity on climate simulations. *J. Geophys. Res. 114*, C 01010 doi:10.1029/2008JC005030.

Kalnay, E., M. Kanamits, R. Kistler, W. Collins, D. Deaven, L. Gandin, M. Iredell, S. Saha, G. White, J. Woollen, Y. Zhu, A. Leetmaa, R. Reynolds, M. Chelliah, W. Ebisuzaki, W. Higgins, J. Janowiak, K. C. Mo, C. Ropelewsk, J. Wang, R. Jenne, and D. Joseph (1996). The NCEP/NCAR 40-year reanalysis project. *Bull. Amer. Meteor. Soc. 77*, 437–470.

Karstensen, J., L. Stramma, and M. Visbeck (2008). Oxygen minimum zones in the eastern tropical Atlantic and Pacific Oceans. *Prog. Oceanogr. 77*, 331–350.

Klocker, A. and T. J. McDougall (2010). Influence of the nonlinear equation of state on global estimates of dianeutral advection and diffusion. *J. Phys. Oceanogr. 40*, 1690–1709.

Kunze, E., E. Firing, J. M. Hummon, T. K. Chereskin, and A. M. Thurnherr (2006). Global abyssal mixing inferred from lowered ADCP shear and CTD strain profiles. *J. Phys. Oceanogr. 36*, 1553–1576.

Kunze, E., E. Firing, J. M. Hummon, T. K. Chereskin, and A. M. Thurnherr (2006b). Corrigendum: Global abyssal mixing inferred from lowered ADCP shear and CTD strain profiles. *J. Phys. Oceanogr. 36*, 2350–2352.

Kunze, E. and T. Sanford (1996). Abyssal mixing: Where it is not. *J. Phys. Oceanogr. 26*, 2286–2296.

Leaman, K. D. (1976). Observations on the vertical polarization and energy flux of near-inertial waves. *J. Phys. Oceanogr. 6*, 894–908.

Leaman, K. D. and T. B. Sanford (1975). Vertical energy propagation of inertial waves: A vector spectral analysis of velocity profiles. *J. Geophys. Res. 80(15)*, 1975–1978.

Ledwell, J. R., E. T. Montgomery, K. L. Polzin, L. C. StLaurent, R. W. Schmitt, and J. M. Toole (2000). Evidence for enhanced mixing over rough topography in the abyssal ocean. *Nature 403*, 179–182.

Ledwell, J. R., A. J. Watson, and C. S. Law (1998). Mixing of a tracer in the pycnocline. *J. Geophys. Res. 103(C10)*, 21499–21529.

Lueck, R. G., F. Wolk, and H. Yamazaki (2002). Oceanic velocity microstructure measurements in the 20th century. *J. Oceanogr. 58*, 153–174.

Macoun, P. and R. Lueck (2004). Modeling the spatial response of the airfoil shear probe using different sized probes. *J. Atmos. Oceanic Technol. 21*, 284–297.

Maria S. Merian (2008). *MSM10/1 short cruise report, http://www.ifm.zmaw.de/de/leitstelle/reisen-des-fs-maria-s-merian/ last check: 23.3.2011.* Maria S. Merian.

Meteor (2009). *M80/2 short cruise report, http://www.ifm.zmaw.de/de/leitstelle/reisen-des-fs-meteor/ last check: 23.3.2011.* Meteor.

Moum, J. N. and T. P. Rippeth (2009). Do observations adequately resolve the natural variability of oceanic turbulence? *J. Mar. Sys. 77*, 409–417.

Munk, W. H. (1966). Abyssal recipes. *Deep Sea Res. 13*, 707–730.

Munk, W. H. (1981). Internal waves and small-scale processes. In B. Warren and C. Wunsch (Eds.), *Evolution of Physical Oceanography; Scientific Surveys in Honor of Henry Stommel*, pp. 264–291. MIT press.

Nagasawa, M., T. Hibiya, Y. Niwa, M. Watanabe, Y. Isoda, S. Takagi, and Y. Kamei (2002). Distribution of fine-scale shear in the deep waters of the north Pacific obtained using expendable current profilers. *J. Geophys. Res. 107(C12)*, doi: 10.1029/2002JC001376.

Nasmyth, P. W. (1973). Turbulence and microstructure in the upper ocean. In J. Nihoul (Ed.), *Fourth Liege Colloquium on Ocean Hydrodynamics, Mem. Soc. Roy. Sci. Liege, series 6, vol. 4*, pp. 47–56.

Nikurashin, M. and S. Legg (2011). A mechanism for local dissipation of internal tides generated at rough topography. *J. Phys. Oceanogr. 41*, 378–395.

Oakey, N. S. (1982). Determination of the rate of dissipation of turbulent energy from simultaneous temperature and velocity shear microstructure measurements. *J. Phys. Oceanogr. 12*, 256–271.

Osborn, T. R. (1980). Estimate of the local rate of vertical diffusion from dissipation measurements. *J. Phys. Oceanogr. 10*, 83–89.

Parkhurst, D. F. (1998). Arithmetic versus geometric means for environmental concentration data. *Environ. Sci. Technol./News 32(3)*, 92A–98A.

Polzin, K., E. Kunze, J. Hummon, and E. Firing (2002). The finescale response of lowered ADCP velocity profiles. *J. Atmos. Oceanic Technol. 19*, 205–224.

Polzin, K., J. Toole, and R. Schmitt (1995). Finescale parameterizations of turbulent dissipation. *J. Phys. Oceanogr. 25*, 306–328.

Pope, S. B. (2000). *Turbulent Flows*. Cambridge University Press.

Press, W. H., S. A. Teukolsky, W. T. Vetterling, and B. P. Flannery (1992). *Numerical Recipes in FORTRAN* (2 ed.). Cambridge University Press.

Rainville, L. and R. Pinkel (2004). Observations of energetic high-wavenumber internal waves in the Kuroshio. *J. Phys. Oceanogr. 34*, 1495–1505.

Ray, R. D. (2001). Internal tides. In J. H. Steele, S. A. Thorpe, and K. K. Turekian (Eds.), *Encyclopedia of Ocean Science*, pp. 1327–1335.

RDI-Teledyne (2008). *Ocean Surveyor Vessel-Mount ADCP, Product information: http://www.rdinstruments.com/observer.aspx last check: 23.3.2011.* RDI-Teledyne.

Saenko, O. A. and W. J. Merryfield (2005). On the effect of topographically enhanced mixing on the global ocean circulation. *J. Phys. Oceanogr. 35*, 826–833.

Schmitt, R. W., J. R. Ledwell, E. T. Montgomery, K. L. Polzin, and J. M. Toole (2005). Enhanced diapycnal mixing by salt fingers in the thermocline of the tropical Atlantic. *Science 308*, 685–688.

Schmitt, R. W., J. M. Toole, R. L. Koehler, E. C. Mellinger, and K. W. Doherty (1988). The development of a fine- and microstructure profiler. *J. Atmos. Oceanic Technol. 5*, 484–500.

Schott, F., J. P. McCrearyJr., and G. C. Johnson (2004). Shallow overturning circulations of the tropical-subtropical oceans. In C. Wang, J. Carton, and S. P. Xie (Eds.), *Earths Climate: The Ocean Atmosphere Interaction*, pp. 261–304.

SeaSunTechnology (2011). *MSS 90 datasheet, http://www.sea-sun-tech.com/fileadmin/pdf-sea/sst_mss90-2.pdf last check: 23.3.2011.* SeaSunTechnology.

Siedler, G., N. Zangenberg, and R. Onken (1992). Seasonal changes in the tropical atlantic circulation: Observation and simulation of the Guinea Dome. *J. Geophys. Res. 97(C1)*, 703–715.

Simmons, H. L., S. R. Jayne, L. C. StLaurent, and A. J. Weaver (2004). Tidally driven mixing in a numerical model of the ocean general circulation. *Ocean Modelling 6*, 245–263.

Smyth, W. D., J. Moum, and D. Caldwell (2001). The efficiency of mixing in turbulent patches: Inferences from direct simulations and microstructure observations. *J. Phys. Oceanogr. 31*, 1969–1992.

Stacey, M. T. (2003). Estimation of diffusive transport of turbulent kinetic energy from acoustic doppler current profiler data. *J. Atmos. Oceanic Technol. 20*, 927–935.

Stevens, C. and J. Imberger (1994). Downward propagating internal waves generated at the base of the surface layer of a stratified fluid. *Geophys. Res. Lett. 21(5)*, 361–364.

StLaurent, L. and R. Schmitt (1999). The contribution of salt fingers to vertical mixing in the North Atlantic Tracer Release Experiment. *J. Phys. Oceanogr. 29*, 1404–1424.

StLaurent, L. C., H. L. Simmons, and S. R. Jayne (2002). Estimating tidally driven mixing in the deep ocean. *Geophys. Res. Lett. 29(23)*, 2106, doi:10.1029/2002GL015633.

Stramma, L., S. Huettl, and J. Schafstall (2005). Water masses and currents in the upper tropical northeast Atlantic off northwest Africa. *J. Geophys. Res. 110*, C12006, doi:10.1029/2005JC002939.

Stramma, L., G. C. Johnson, J. Sprintall, and V. Mohrholz (2008). Expanding oxygen-minimum zones in the tropical oceans. *Science 320*, 655–658.

Thorpe, S. A. (2005). *The Turbulent Ocean.* Cambridge University Press.

Townsend, A. A. (1968). Excitation of internal waves in a stably-stratified atmosphere with considerable wind-shear. *J. Fluid Mech. 32*, 145–171.

UH (2010). *University of Hawaii Current Group, http://currents.soest.hawaii.edu/docs/adcp_doc/_images/scattering_layer.png last check: 23.3.2011.* UH.

VanHaren, H. (2009). Using high sampling-rate ADCP for observing vigorous processes above sloping [deep] ocean bottoms. *J. Mar. Systems 77*, 418–427.

Wallace, D. W. R. and H. W. Bange (2004). Introduction to special section: Results of the Meteor 55: Tropical SOLAS expedition. *Geophys. Res. Lett. 31*, L 23S01, 1–4.

Walter, M., C. Mertens, and M. Rhein (2005). Mixing estimates from a large-scale hydrographic survey in the north Atlantic. *Geophys. Res. Lett. 32*, L 13605, doi:10.1029/2005GL022471.

Walter, S., H. W. Bange, U. Breitenbach, and D. W. R. Wallace (2006). Nitrous oxide in the north Atlantic Ocean. *Biogeosciences 3*, 607–619.

Watson, A. J., M.-J. Messias, E. Fogelqvist, K. A. VanScoy, T. Johannessen, K. I. C. Oliver, D. P. Stevens, F. Rey, T. Tanhua, K. A. Olsson, F. Carse, K. Simonsen, J. R. Ledwell, E. Jansen, D. J. Cooper, J. A. Kroepke, and E. Guilyardi (1999). Mixing and convection in the Greenland Sea from a tracer-release experiment. *Nature 401*, 902–904.

Webb, D. J. and N. Suginohara (2001). Vertical mixing in the ocean. *Nature 409*, 37.

Winkel, D. P., M. Gregg, and T. Sanford (2002). Patterns of shear and turbulence across the Florida Current. *J. Phys. Oceanogr. 32*, 3269–3285.

Wolk, F., H. Yamazaki, L. Seuront, and R. G. Lueck (2002). A new free-fall profiler for measuring biophysical microstructure. *J. Atmos. Oceanic Technol. 19*, 780–793.

Wunsch, C. and R. Ferrari (2004). Vertical mixing, energy, and the general circulation of the oceans. *Annu. Rev. Fluid Mech. 36*, 281–314.

Yool, A., A. P. Martin, C. Fernandez, and D. R. Clark (2007). The significance of nitrification for oceanic new production. *Nature 447*, 999–1002.

A Used expressions from GM76 internal wave model

When in need of estimates of the ocean internal wave field's energy content or its shear variance, a spectral model comes in handy that relates energy to wavenumber and frequency and is in addition more or less proven by observations. Here we reproduce and deduce spectral densities and other relations of the Garrett-Munk internal wave model in its 1976 flavour (GM76), which is frequently used and which we also rely on. All units are radian. References [Garrett and Munk, 1972, 1975; Cairns and Williams, 1976; Munk, 1981; Gregg and Kunze, 1991] lay the historical record and may serve as a collection of concepts and expressions.

Munk's 1981 model version (GM81) does not imply additional observations compared to GM76, but a slightly different functional expression for vertical wavenumber influence, and produces different expressions for spectral densities [Gregg and Kunze, 1991]. GM76 fits better to our data in that observed low 'background' internal wave states match GM76 shear spectral level, while GM81 shear spectral level is a factor of $2/\pi$ lower.

GM76 spectral densities

A good starting point is the GM76 expression for kinetic energy spectral density in two dimensions (frequency ω and vertical mode number j):

$$F_u(\omega, j) = \frac{2}{\pi} E_{GM} b^2 N_0 N \cdot \left[\frac{f}{\omega^3} \frac{\omega^2 + f^2}{\sqrt{\omega^2 - f^2}} \right] \cdot \frac{1}{j^* \left(1 + \frac{j}{j^*}\right)^2} \tag{A.1}$$

with E_{GM} the dimensionless spectral energy level (Garrett and Munk's value $E_{GM} = 6.3 \cdot 10^{-5}$), b the stratification scale depth when modelling the stratification as exponential, N_0 a characteristic buoyancy frequency, j^* a characteristic ('peak') mode number, N the local buoyancy frequency and f the local Coriolis parameter. F_u is defined for positive axes j and ω (ω bounded by $f \leq \omega \leq N$). The assumption of exponential stratification is $N = N_0 \cdot \exp(z/b)$ with z-axis pointing upward. The classic parameter choice is $N_0 = 5.24 \cdot 10^{-3}\, rad/s$, $b = 1300\, m$ and $j^* = 3$.

To derive kinetic energy spectral density as a function of $\omega > 0$ and vertical

wavenumber $m > 0$, use constancy of marginal kinetic energy when substituting parameters, $F_u(\omega, m)\, dm = F_u(\omega, j)\, dj$, and

$$m = \frac{\pi}{b}\frac{N}{N_0} j \tag{A.2}$$

which to a good approximaton results from matching a wave of vertical modenumber j to an ocean with exponential stratification, average buoyancy frequency N, and depth more than 3 times b. Equation A.2 also defines m^* from j^*.

Applied to equation A.1,

$$F_u(\omega, m) = \frac{2}{\pi^2} E_{GM} b^3 N_0^2 \cdot \frac{1}{j^*} \cdot \left[\frac{f}{\omega^3}\frac{\omega^2 + f^2}{\sqrt{\omega^2 - f^2}}\right] \cdot \frac{1}{\left(1 + \frac{m}{m^*}\right)^2} \tag{A.3}$$

or

$$F_u(\omega, m) = \frac{2}{\pi} E_{GM} b^2 N_0 N \cdot \left[\frac{f}{\omega^3}\frac{\omega^2 + f^2}{\sqrt{\omega^2 - f^2}}\right] \cdot \frac{1}{m^* \left(1 + \frac{m}{m^*}\right)^2}. \tag{A.4}$$

In an analogous way with $F_u(k, m)\, dk = F_u(\omega, m)\, d\omega$ and using the internal wave dispersion relation

$$k^2 = m^2 \cdot \frac{\omega^2 - f^2}{N^2 - \omega^2} \tag{A.5}$$

or

$$\omega^2 = \frac{k^2 N^2 + m^2 f^2}{k^2 + m^2} \tag{A.6}$$

to get $d\omega/dk$, derive kinetic energy spectral density as a function of vertical wavenumber $m > 0$ and horizontal wavenumber $k > 0$ ($k^2 = k_1^2 + k_2^2$):

$$F_u(k, m) = \frac{2}{\pi} E_{GM} b^2 N_0 N \left[\frac{f\sqrt{N^2 - f^2}\,(k^2 N^2 + 2m^2 f^2 + k^2 f^2)}{\sqrt{k^2 + m^2}\,(k^2 N^2 + m^2 f^2)^2}\right] \frac{m^* m^2}{(m^* + m)^2}. \tag{A.7}$$

When interested in kinetic energy spectral density in one dimension for parameters ω or m, integrate (A.4) by using

$$\int_0^\infty \frac{1}{\left(1+\frac{m}{m^*}\right)^2} dm = m^* \tag{A.8}$$

or

$$\int_f^N \left[\frac{f}{\omega^3}\frac{\omega^2+f^2}{\sqrt{\omega^2-f^2}}\right] d\omega = \frac{3}{2} arctan\frac{\sqrt{N^2-f^2}}{f} + \frac{1}{2}\cdot\left[\frac{\frac{\sqrt{N^2-f^2}}{f}}{1+\frac{N^2-f^2}{f^2}}\right] \approx \frac{3\pi}{4}, \tag{A.9}$$

and get

$$\Phi_u(\omega) = \int_0^\infty F_u(\omega, m)\, dm = \frac{2}{\pi} E_{GM} b^2 N_0 N \cdot \left[\frac{f}{\omega^3}\frac{\omega^2+f^2}{\sqrt{\omega^2-f^2}}\right] \tag{A.10}$$

and

$$\Phi_u(m) = \int_f^N F_u(\omega, m)\, d\omega = \frac{3}{2\pi} E_{GM} b^3 N_0^2 \frac{1}{j^*}\cdot\frac{1}{\left(1+\frac{m}{m^*}\right)^2}. \tag{A.11}$$

For vertical shear spectral density, multiply $\Phi_u(m)$ by m^2 (which in power spectrum corresponds to vertical first differencing of velocity):

$$\Phi_S(m) = \int_f^N F_u(\omega, m)\, d\omega = \frac{3}{2\pi} E_{GM} b^3 N_0^2 \frac{1}{j^*}\cdot\frac{m^2}{\left(1+\frac{m}{m^*}\right)^2}. \tag{A.12}$$

In the limit of large m, $\Phi_S(m)$ becomes constant in m and scales as $b\cdot j^*\cdot N^2$, for (A.12) is equivalent to

$$\Phi_S(m) = \frac{3\pi}{2} E_{GM} b N^2 j^* \cdot \frac{m^2}{(m^*+m)^2}. \tag{A.13}$$

Froude spectra $\Phi_{S/N}(m) = \Phi_S(m)/N^2$ may be calculated alternatively to shear spectra, with the advantage of spectral level being independent of N^2.

Total kinetic energy of the internal wave field finally becomes

$$\left\langle u^2 \right\rangle = \int_f^N \Phi_u(\omega)\, d\omega = \int_0^\infty \Phi_u(m)\, dm = \frac{3}{2} E_{GM} b^2 N_0 N. \tag{A.14}$$

Total shear variance would become infinite, but GM76 ignores the fact later discovered by [Gargett et al., 1981] that for m greater than a critical wavenumber $m_c \approx 0.6 rad/m$, the shear spectrum is no longer approximately white but rolls off as m^{-1}. To kinetic energy spectra this roll-off is of no practical importance.

Doppler shifting

When going on a ship moving relative to the water, one observes the Doppler-shifted internal wave field. The corresponding Doppler-shifted spectra Garrett and Munk term 'towed spectra'. When underway at a speed much faster than 0.22 m/s, the observed Doppler shifted 'frequency-of-encounter spectrum' may be approximated by the frozen-field hypothesis of a steady internal wave field [Garrett and Munk, 1972]. That means that the horizontal wavenumber k in $F_u(k,m)$ of equation A.7 may be substituted by $k = \omega_t / v_0$, with ship speed v_0, observed frequency ω_t and vertical wavenumber m. Thus kinetic energy spectral density observed from a moving platform $F_{u,v_0}(\omega_t, m)$ emanates after applying $F_{u,v_0}(\omega_t, m)\, d\omega_t = F_u(k,m)\, dk$:

$$F_{u,v_0}(\omega_t, m) = v_0^2 \cdot \frac{2}{\pi} E_{GM} b^2 N_0 N \left[\frac{f\sqrt{N^2 - f^2}\,(\omega_t^2 N^2 + 2m^2 f^2 v_0^2 + \omega_t^2 f^2)}{\sqrt{\omega_t^2 + v_0^2 m^2}\,(\omega_t^2 N^2 + m^2 f^2 v_0^2)^2} \right] \frac{m^* m^2}{(m^* + m)^2}. \tag{A.15}$$

The frozen-field approximation proves to be good for ship speed $v_0 \geq 2m/s$.

Principally, it is possible to derive $F_{u,v_0}(\omega_t, m)$ from $F_u(\omega, k_1, k_2)$ (which is from $F_u(k,m)$ of equation A.7 considering rotational symmetry and constancy of total kinetic energy), then Galileo-transform $F_u(\omega, k_1, k_2)$ by $\omega = \omega_t + k_1 \cdot v_0$ and finally do line-integrals along $m = const.$ on planes of $\omega_t = const.$ But this is an analytical no-thru-road, and a numerical hassle because of the singularity at $\omega = f$.

Loss of observed variance when underway

The former remarks apply to a perfect observer from a moving ship. Our interest nonetheless lies in the consequences of real observing systems like an ADCP going on moving platforms. There is always an unavoidable amount of signal averaging in time by the observing system, that leads to a loss in observed variance of the wave field (adding up to other averaging effects of the ADCP, that are commented on in subsection 4.2.2). What percentage of kinetic energy or shear variance of the internal wave field is escaping observation just because of moving at speed v_0 and averaging signals for a time t_{ave}?

Let a ship move steadily on water of mean velocity zero, and observe a pure internal wave of wavenumber $k = (k_1, k_2, m)$ and frequency ω below it, no matter what wave

property is observed. Say, it is possible to follow the depth of a wave crest. The ship course determines the x-axis and thus the direction of wavenumber component k_1. The wave's horizontal wavenumber $k = (k_1, k_2)$ be then inclined to the ship course by angle φ, thus determining

$$k_1(m, \omega, \varphi, f, N) = \|k\| \cdot cos\varphi = m \cdot \sqrt{\frac{\omega^2 - f^2}{N^2 - \omega^2}} \cdot cos\varphi \tag{A.16}$$

by aid of the internal wave dispersion relation. Parameters are defined on $m \in R^+$, $\varphi \in [0, 2\pi[$, $\omega \in R^+$ with $f \leq \omega \leq N$. When f and N chosen, m, ω and φ span a 3-dimensional parameter space.

The ship at location x_0 observes a wave crest at z_0 and follows it to $x_1 = x_0 + \Delta x = x_0 + v_0 \cdot t_{ave}$ to find it again at $z_1 = z_0 + \Delta z$. Δz is the sum of a Δz_{t_0} caused by the wave's inclination α to the horizontal, $\Delta z_{t_0} = tan\alpha \cdot \Delta x = -\frac{k_1}{m} \cdot v_0 \cdot t_{ave}$, plus a $\Delta z_{t_0 \to t_{ave}}$ caused by the vertical phase velocity, $\Delta z_{t_0 \to t_{ave}} = \frac{\omega}{m} \cdot t_{ave}$. Thus

$$\Delta z = \frac{t_{ave}}{m} \cdot (\omega - k_1 v_0), \tag{A.17}$$

which may also be interpreted as the vertical crest displacement after t_{ave}, considering the Doppler-shifted observed wave frequency $\omega_t = \omega - k_1 v_0$.

When averaging a harmonic wave horizontally for a time t_{ave}, the observed variance in relation to the original variance (or remaining power fraction) p_r of the averaged wave is

$$p_r(t_{ave}, T_{obs}) = \frac{sin^2\left(\pi \cdot \frac{t_{ave}}{T_{obs}}\right)}{\left(\pi \cdot \frac{t_{ave}}{T_{obs}}\right)^2} \tag{A.18}$$

with observed period $T_{obs} = 2\pi / (\omega - k_1 v_0)$. This effect of averaging in time is equivalent to vertical averaging, considering equation A.17. The remaining power fraction after averaging of a single wave then becomes

$$p_r(m, \omega, \varphi, v_0, t_{ave}, f, N) = \frac{sin^2\left(\frac{\omega - k_1(m,\omega,\varphi,f,N) \cdot v_0}{2} \cdot t_{tave}\right)}{\left(\frac{\omega - k_1(m,\omega,\varphi,f,N) \cdot v_0}{2} \cdot t_{tave}\right)^2}. \tag{A.19}$$

When interested in the remaining fraction of total kinetic energy or of total shear variance of the full continuous internal wave field, consider GM76 spectral energy density as of equation A.4. Assuming horizontal isotropy, $F_u(m, \omega, \varphi) = F_u(m, \omega) / (2\pi)$ for kinetic energy spectral density. $F_S(m, \omega, \varphi) = F_u(m, \omega, \varphi) \cdot m^2$ for shear variance spectral density. For a single wave, the remaining kinetic energy

spectral level is $F_u(m,\omega,\varphi)\cdot p_r(m,\omega,\varphi,v_0,t_{ave},f,N)$. So it is possible to deduce $P_{r,u}$, the 'remaining observed kinetic energy percentage after underway averaging of the internal wave field according to GM76 after choosing f, N, and v_0' as a two-dimensional field in m and t_{ave} as

$$P_{r,u}(m,t_{ave}) = \frac{\int_0^{2\pi}\int_f^N F_u(m,\omega,\varphi)\cdot p_r(m,\omega,\varphi,v_0,t_{ave},f,N)\,d\omega d\varphi}{\int_0^{2\pi}\int_f^N F_u(m,\omega,\varphi)\,d\omega d\varphi}, \tag{A.20}$$

equations A.19 and A.16 to be considered and A.20 to be numerically integrated. The remaining shear variance percentage is $P_{r,S}(m,t_{ave}) = P_{r,u}(m,t_{ave})$, as m is kept as a parameter and not subject to integration.

Latitudinal influence on internal wave field

The overall effect of a decreasing Coriolis parameter with decreasing latitude towards the equator is a flattening of internal wave crest slopes. This causality emerges when taking a closer look at near inertial waves that contain the major part of shear variance or shear energy.

The fraction of shear energy contained in waves with frequencies $f \le \omega \le c\cdot f$, $c>1$ is found considering GM76 shear spectral density $F_u(k,m)\cdot m^2$ with $F_u(k,m)$ as of equation A.7,

$$P(c,f) = \frac{\int_0^{m_c}\int_0^{m\cdot tan\alpha} F_u(k,m)\ m^2\,dk\,dm}{\int_0^{m_c}\int_0^{\infty} F_u(k,m)\ m^2\,dk\,dm}. \tag{A.21}$$

m_c denotes the critical vertical wavenumber of Gargett's canonical shear spectrum [Gargett et al., 1981]. $m\cdot tan\alpha$ is the upper limit for horizontal wavenumber when considering the frequency range upper limit $c\cdot f$; $tan\alpha$ won from the dispersion relation as

$$tan\alpha = \sqrt{\frac{(c\cdot f)^2 - f^2}{N^2 - (c\cdot f)^2}}. \tag{A.22}$$

Fig. A.1 is a graphical representation of equation A.21 and reveals a nearly constant amount of shear energy contained in internal waves of frequency below $\omega = c\cdot f$ independent of latitude, for a chosen small c.

This also means that nearly constant amounts of shear energy will be found with internal waves of crest slopes $tan\,\alpha \le tan\,\alpha_{limit} = \frac{f}{N}\sqrt{c^2-1}$, which follows from equation A.22 if c is small and $f^2 \ll N^2$. So independent of what c exactly is chosen

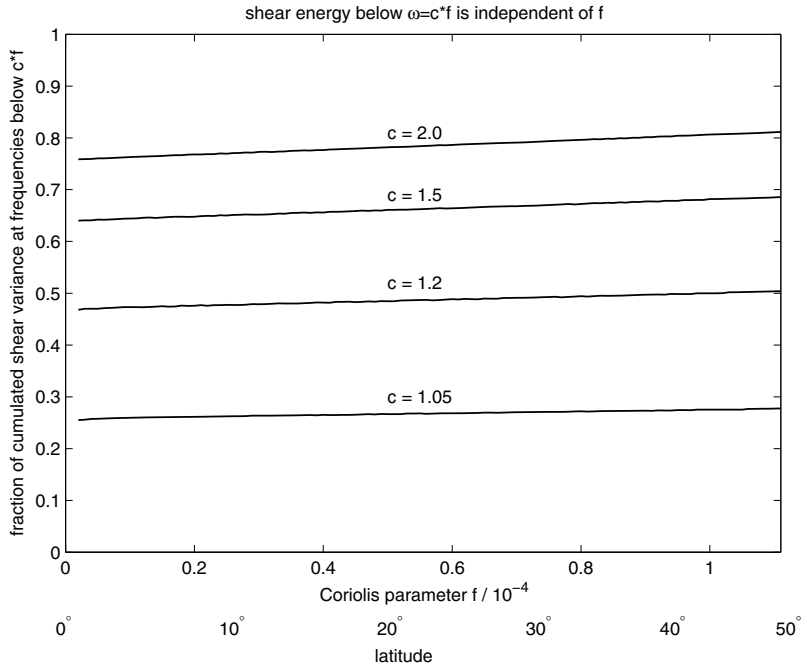

Fig. A.1: Fraction of cumulated shear variance in internal wave field in frequency range $f \leq \omega \leq c \cdot f$; as a function of Coriolis parameter f. For example $\omega \leq c \cdot f$ for $c \approx 2$ encloses a major and nearly constant amount of shear energy, independent of latitude.

to represent an upper limit for near inertial waves containing the major part of shear energy,

$$tan\,\alpha_{limit} \propto \frac{f}{N} \tag{A.23}$$

is valid to a good approximation.

Erklärung

Hiermit erkläre ich, dass ich die vorliegende Arbeit - abgesehen von der Beratung durch meinen Betreuer - unter Einhaltung der Regeln guter wissenschaftlicher Praxis der DFG selbständig erarbeitet und verfasst habe. Diese Arbeit hat weder ganz, noch zum Teil, einer anderen Stelle im Rahmen eines Prüfungsverfahrens vorgelegen, ist nicht veröffentlicht und auch nicht zur Veröffentlichung eingereicht.

Kiel, 23.3.2011